Multiple and Extended References in Fourier Transform Holography

vorgelegt von
Diplom-Physiker
René Könnecke
Dessau

von der Fakultät II - Mathematik und Naturwissenschaften
der Technischen Universität Berlin
zur Erlangung des akademischen Grades
Doktor der Naturwissenschaften
Dr.rer.nat.

genehmigte Dissertation

Tag der wissenschaftlichen Aussprache: 11. Februar 2010

Promotionsausschuss:

Vorsitzender:	Prof. Dr. Mario Dähne
Gutachter:	Prof. Dr. Jürgen Eichler
Gutachter:	Prof. Dr. Stefan Eisebitt

Berlin 2010
D 83

Contents

Abbreviations

CCD	Charge-Coupled Device
FEL	Free Electron Laser
FIB	Focused Ion Beam
FFT	Fast Fourier Transform
FTH	Fourier Transform Holography
FWHM	Full Width Half Maximum
HERALDO	Holography with Extended Reference by Autocorrelation Linear Differential Operation
MTF	Modulation Transfer Function
RSH	Ratio of spacing to hole diameter
SEM	Scanning Electron Microscope
URA	Uniformly Redundant Array

Chapter 1

Introduction

Imaging is one of the oldest techniques of humankind. The first paintings of items in burrows, seen in the visible light, have changed over thousands of years to technical imaging of objects in a huge range of electromagnetic radiation, extending the range of visible light to larger and to shorter wavelengths. Imaging with soft X-rays is one example for a shift towards shorter wavelengths.
In recent years in the range of soft X-rays a new method of imaging is established, the Fourier Transform Holography (FTH) [26]. The FTH is a promising imaging method, since it lacks of optical lenses and is, therefore, free of aberrations. FTH with soft X-rays is typically carried out via an opaque mask, which contains a small aperture producing the reference beam. The reference aperture is located next to the object in this mask. So far, the achieved resolution in soft X-ray FTH in transmission mode is 50 nm [26].

In the range of soft X-rays the research field is growing fast, especially through the new development of Free Electron Lasers (FEL). The characteristic of the FEL-beam of having a high brilliance is a particular benefit for FTH as an imaging method in FEL-experiments. The high transverse coherence length enables experiments with a larger lateral dimension. Additionally, the femtosecond pulsed nature of the FEL-beam enables femtosecond time-resolved imaging, using a single FEL-pulse for the measurement.

Although "conventional" FTH with one pinhole as reference can resolve objects with a high resolution, the photon flux through the single reference aperture can limit the signal to noise ratio in a short exposure. Multiple reference patterns

can retain the high resolution of conventional FTH, but additionally increase the signal intensity. Extended reference patterns, on the other hand, are an alternative approach to increase the signal to noise ratio. As a specific multiple reference pattern the Uniformly Redundant Array (URA) is investigated in this thesis, whereas the Extended Reference by Autocorrelation Linear Differential Operation (HERALDO) is introduced as one example for an extended reference.

Experiments in the soft X-ray spectral range are carried out for both types of reference structures in this thesis.
In the URA-experiments we succeeded to characterize the transmission of the structure "at wavelength" enabling us to include this information in the image reconstruction procedure. For HERALDO, this is the first report of the application of this concept for wavelengths shorter than visible light. Apart from the "standard" imaging properties, the potential for tomography with HERALDO is explored.
In both cases, images are obtained without the need for iterative phase retrieval algorithm.

Chapter 2

Fourier Transform Holography (FTH)

Fourier Transform Holography (FTH) is a technique well-known for several decades. The first experimental realization has been carried out with visible light by G.W. Stroke [74] in 1965. Meanwhile, FTH has been transferred into the range of soft X-rays [24, 26, 39, 62, 64, 72, 73].

2.1 Principle of Fourier Transform Holography

FTH is a lensless imaging method encoding an object in a hologram. In FTH the object and the reference are placed together in one plane as a sample and are illuminated at the same time in transmission geometry by a beam orthogonal to the sample. The scattered light from the object and the scattered light from the reference interfere with each other and form a hologram in the far field. The hologram is detected as the spatial variation of intensities by a suitable pixelated detector such as a CCD-camera. The phase difference between the scattered photons is encoded in the hologram in form of fringes.

In the following a perfectly coherent illumination of the sample with a plane wave is assumed. The wavefield hitting the detector can be described mathematically as the Fourier transform of the wavefield $f(x, y)$ at the exit surface of the sample with x and y as coordinates in real space. The wavefield $f(x, y)$ can be written as:

$$f(x, y) = o(x, y) + r(x, y) \quad , \tag{2.1}$$

where $o(x, y)$ is the object modulation and $r(x, y)$ is the reference modulation. The wavefield $F(q_x, q_y)$ at the detector can thus be described as:

$$F(q_x, q_y) = \mathscr{F}\{f(x, y)\} = \iint_{-\infty}^{\infty} f(x, y) e^{-i2\pi(q_x x + q_y y)} dx dy \quad . \tag{2.2}$$

Here, (q_x,q_y) are the transverse coordinates in Fourier space and $\mathscr{F}\{X\}$ denotes the Fourier transform of the quantity X. The detector records the intensity $|F(q_x, q_y)|^2$, which constitutes a hologram with q_x=0 and q_y=0 in the center of it. The inverse Fourier transform $\mathscr{F}^{-1}\{|F(q_x, q_y)|^2\}$ yields:

$$\mathscr{F}^{-1}\{|F(q_x, q_y)|^2\} = f \otimes f^* = o \otimes o^* + r \otimes r^* + o \otimes r^* + r \otimes o^* \tag{2.3}$$

with $\otimes$ denoting a convolution and f^* indicating the complex conjugate of f. The terms themselves have special meanings which are:

- $f \otimes f^*$: autocorrelation of the entire sample consisting of the object and the reference
- $o \otimes o^*$: autocorrelation of the object
- $r \otimes r^*$: autocorrelation of the reference
- $r \otimes o^*$: cross-correlation of the reference and the complex conjugate object
- $o \otimes r^*$: cross-correlation of the object and the complex conjugate reference.

The operations "convolution" and "correlation" are defined as:

$$f(x) \otimes g(x) \equiv \int_{-\infty}^{\infty} f(\rho) g(x - \rho) d\rho \qquad \text{(convolution)} \tag{2.4}$$

$$f(x) \otimes g^*(x) \equiv \int_{-\infty}^{\infty} f(\rho) g^*(x + \rho) d\rho \qquad \text{(correlation)} \quad . \tag{2.5}$$

After the Fourier transform of the hologram the resulting real space picture contains the autocorrelation of the object and the autocorrelation of the reference, which are centered at the origin. The two cross-correlations between object and reference are placed radially opposite to the origin to each other, as seen in figure 2.1.

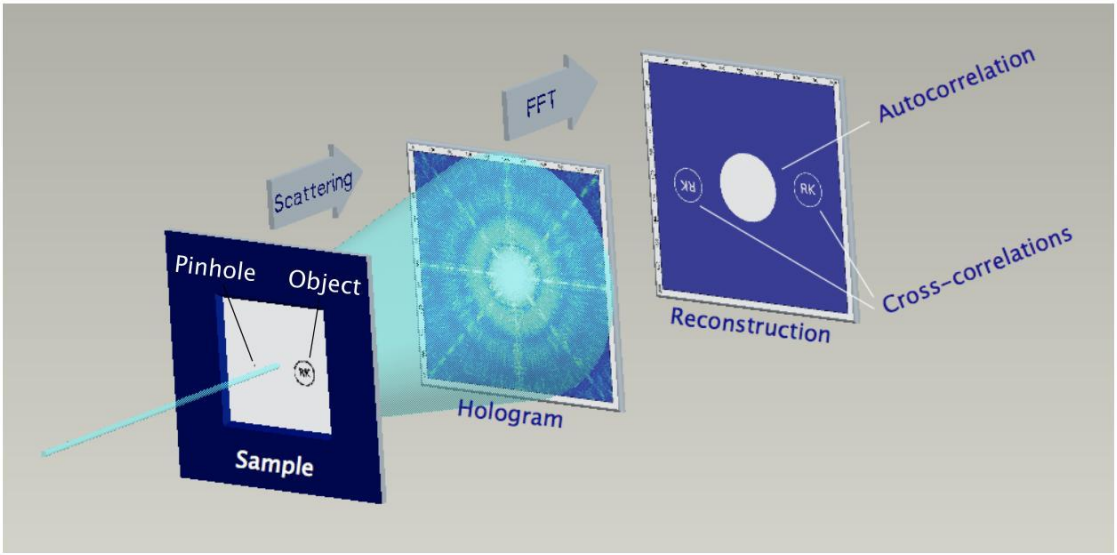

Figure 2.1: Setup for Fourier Transform Holography; The beam illuminates the entire sample. The scattered light from the exit surface of the sample forms a hologram in the far field. The Fourier transform of the hologram produces the autocorrelation of the entire sample.

In conventional FTH the reference is one single pinhole. After the Fourier transform of the hologram the cross-correlation contains the convolution of the pinhole and the object, thus depicting the object itself. The resolution of the reconstructed object depends on the diameter of the pinhole in addition to the resolvable contrast and to the maximum momentum transfer recorded in the hologram. The smaller the diameter of the reference pinhole the higher is the resolution. Ideally, the reference should be a δ-function with respect to the transmitted radiation intensity. In reality a better resolution due to a smaller pinhole implies a lack of signal intensity. The smaller the pinhole the fewer photons reach the detector.
In the dissertation of W.F. Schlotter [71] this dilemma is shown very illustratively, seen in figure 2.2. The first object "Ampelmännchen" in figure 2.2a is the original. The objects next to the original show reconstructions produced with different pinhole sizes. The first "Ampelmännchen" right to the original is convolved with a pinhole resulting in a contrast of 14% compared to the original. The objects in 2.2c and 2.2d reconstructed with pinholes having a diameter twice and three times as large as the pinhole used in 2.2b, show contrasts of 40% and 98%, respectively. The associated loss in resolution is clearly visible.

Figure 2.2: Dilemma between resolution and signal intensity [71]

In theory, when noise is excluded, the signal intensity can be increased by a simple multiplication, since the background is zero. In a real measurement the noise cannot be neglected. Any multiplication after the hologram is detected will increase the noise level as well. Obviously, one way to increase the signal to noise ratio is to increase the signal intensity. Whereas the increase of the exposure time might be possible for many experiments, experiments investigating the dynamics of objects require short exposure times. In order to decrease the noise level relatively to the signal intensity also for this kind of experiments a way is found to maintain the same exposure time and the same resolution, but to increase the signal intensity. This way is the "enlargement" of the reference structure. In this thesis two groups for enlarged reference structures are introduced:

- the multiple reference pattern
- the extended reference pattern.

An illustration of enlarging the reference pattern in a "multiple reference" style is seen in figure 2.3. Two ways of enlargements are shown. The first way, shown in figure 2.3a, is to increase the number of pinholes under the consideration that each reconstructed object is not disturbed by any other cross-correlation. The second way is to put all pinholes close together in a compact form as shown in figure 2.3b. Both reference structures increase the signal intensity and, therefore, increase the signal to noise ratio. While in situation (a) the spatial resolution is connected to the size of each pinhole, in (b) an additional factor is how well the overlapping images can be disentangled. Another difference is that the reference structure in figure 2.3a requires a wide coherent illumination, while the second reference structure, seen in figure 2.3b, can operate with a beam, which is focused

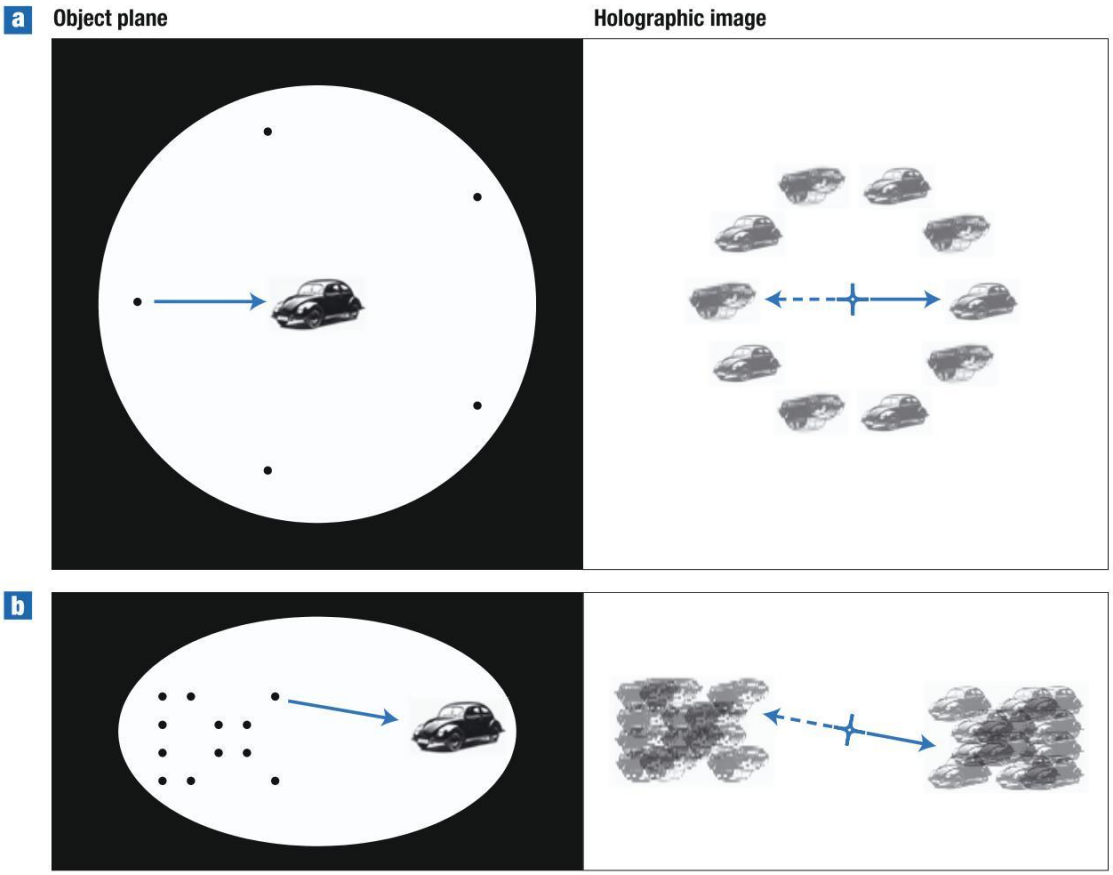

Figure 2.3: Two examples for enlarging a reference structure [22]

on a smaller area leading to a higher usable photon flux density on the sample. Each pinhole reconstructs an object after the hologram is Fourier transformed. In the first reference structure the object is directly reconstructed (multiple times) since the separation conditions, which will be elaborated below, are fulfilled. The contrary is the case in the second reference structure, in which the pinholes lie so close together that the reconstructed objects overlap each other. In chapter 3 two reconstruction methods will be shown how to disentangle the object image from the overlap, when the arrangement of the pinholes follows the structure of an Uniformly Redundant Array (URA).

Enlarging a reference structure can also be done in form of an "extended reference" pattern. In contrast to the multiple reference pattern, the extended reference pattern is based on extended continuous references with corners or kinks like lines, rectangles or other shapes. The extended reference pattern increases the signal

intensity as well. The HERALDO-Pattern belongs to this category. The term HERALDO stands for Holography with Extended Reference by Autocorrelation Linear Differential Operation. The reconstruction method for the HERALDO-Pattern is different to the multiple reference pattern, since the reference points are mathematically "generated" at the corners or kinks of the reference structure in HERALDO, which will be described in detail in chapter 4.

2.2 Separation conditions

Conventional FTH

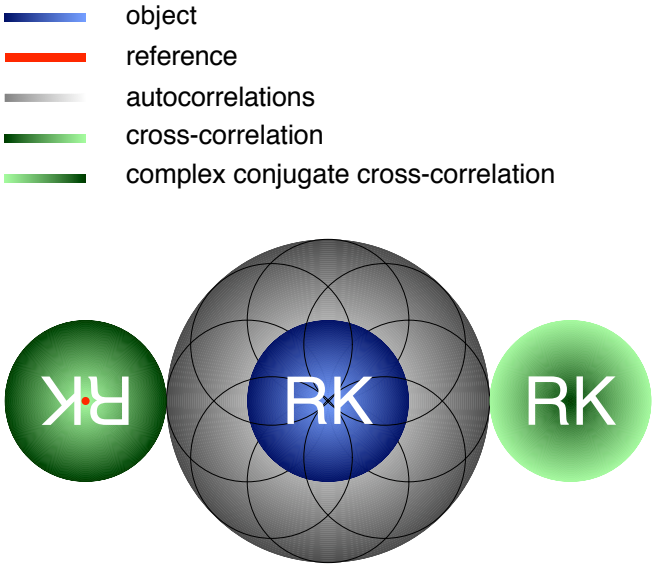

Figure 2.4: Separation condition for conventional FTH; Object (blue) and reference pinhole (red) are illuminated by a coherent beam. Grey and green: position of autocorrelations and cross-correlations to each other after the hologram is Fourier transformed.

In order to gain a usable reconstruction the cross-correlations containing the desired image information should not be overlaid by the autocorrelations. The smallest distance between the autocorrelations and the cross-correlations depends on the center-to-center distance between the original object and the reference plus the

size of the object, neglecting the size of the reference. The separation condition for conventional FTH is illustrated in figure 2.4. The pinhole must be at least three times the radius of the object away from the center of the object in order to avoid overlapping.
The existence of more than one pinhole leads to the separation conditions of many pinholes, which differ from conventional FTH by the additional condition that the pinholes must be separated by a distance of at least equal to the size of the object. In figure 2.3a an example is shown following these conditions.

URA

The URA-Pattern is a compact reference pattern. An example is the pattern in figure 2.3b. The entire reference pattern is larger than the object, leading to a larger autocorrelation of the reference in comparison to the autocorrelation of the object. In order to avoid overlappings between the autocorrelations and the cross-correlations, the following separation condition is added to the separation condition of conventional FTH:

$$a = \frac{3s + r}{2} \quad , \tag{2.6}$$

where a is the distance between the middle of the object and the middle of the reference pattern, s is the size of the reference pattern and r the radius of the object.

HERALDO

The separation condition for a reference point in the HERALDO-Pattern is based on the separation condition for conventional FTH in so far, that both are identical, when the pinhole in conventional FTH is set equal to the corner or kink in the HERALDO-Pattern. In chapter 4 it will be shown that the corner or kink acts as reference point. Since the HERALDO-Pattern has typically more than just one reference point as in the case of conventional FTH, an additional separation condition must be followed. The additional separation condition states that the reference points must be apart from each other by a distance of at least the size of the object.
An example of a HERALDO-Pattern is shown in figure 2.5. In this figure the

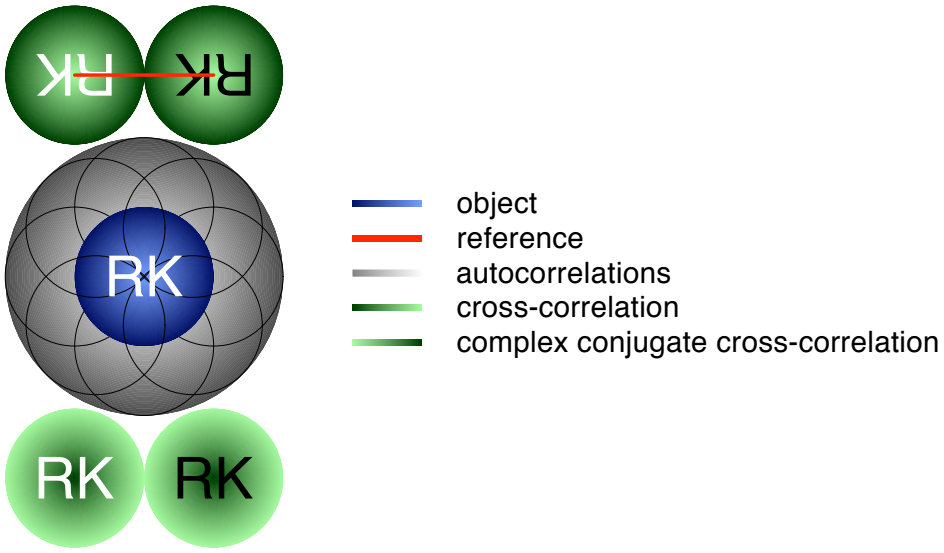

Figure 2.5: Separation condition for a HERALDO-Pattern; Object (blue) and reference line (red) are illuminated by a coherent beam. Grey and green: position of autocorrelations and cross-correlations to each other after the hologram is Fourier transformed and differentiated along the length of the line.

reference is the horizontal line between the upper two "RK"s. The endpoints of this line act as reference points. In order to follow the additional separation condition, the line has to have the length equal or larger than the diameter of the object.

2.3 Resolution

An imaging system attempts to capture the spatial structure of the object. In soft X-ray FTH in transmission mode the spatial structure is the projection of the absorption or of the phase shift along the optical axis. In this thesis only the absorption is considered.
In practice the spatial resolution depends mainly on three parameters:

1. Diffraction limited resolution

2. Reference points

3. Modulation Transfer Function.

2.3.1 Diffraction limited resolution

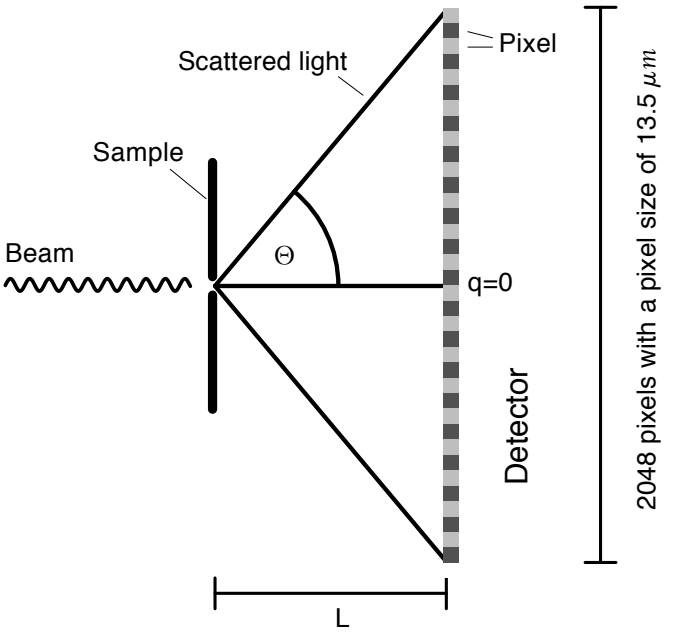

Figure 2.6: Geometry of the experimental setup

The choice of the field of view determines the maximum and minimum resolvable length in dependence of other experimental conditions, like the wavelength of illumination, the distance between sample and detector, the total size of the detector and the pixel size of the detector.

The geometry of the experimental setup is illustrated in figure 2.6. The sample is coherently illuminated by synchrotron radiation in transmission mode. At a distance L the hologram is detected by a CCD-camera.
The distance L between the sample and the detector has to be chosen on the size of the CCD-camera and the size of the pixels. While a short distance will decrease the detection of long lengths in the sample, a large distance will reduce the acceptance angle Θ and thus limit the detection of scattered light associated with short lengths in the sample, as seen in figure 2.7.

A large distance in the sample will be displayed in the hologram as fringes with a high frequency. According to the Nyquist-Shannon sampling theorem, also known

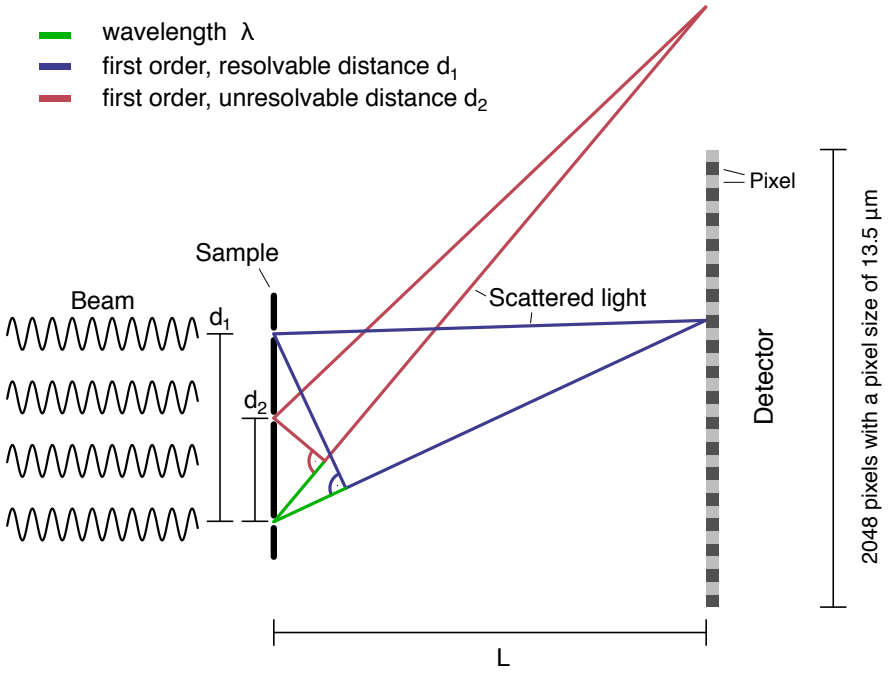

Figure 2.7: First order of constructive interference originated from different distances in the sample plane

as Whittaker-Kotelnikow-Shannon sampling theorem, the sampling of the hologram has to be done with at least twice the maximum frequency displayed in the hologram. That means, in order to resolve the longest distance in the sample, the highest hologram frequency at the location of detection must have a wavelength of two times the pixel size, i.e. $2\,\mathrm{x}\,13.5\,\mu$m for the CCD-detector used for the experiments in this work.

Short distances in the sample are displayed in the hologram as fringes with a low frequency. Fringes can only be resolved by the inverse Fourier transform, when the wavelength of the fringes is shorter than half the size of the detector. This is the case, when the first order of the constructive interference between two points, separated by a distance d, and their zero order lie within half of the detection area in the CCD-camera.

On this basis the shortest detectable distance d_{min} and the longest detectable

distance d_{max} can be calculated with the grating equation:

$$d_{min} = \frac{\lambda}{sin(\Theta_{max})} \qquad tan(\Theta_{max}) = \frac{S_{CCD}}{2L}$$
$$d_{max} = \frac{\lambda}{sin(\Theta_{min})} \qquad tan(\Theta_{min}) = \frac{2S_{pixel}}{L} \quad .$$

Here, λ is the wavelength of the incoming light, Θ_{max} the maximum resolvable angle, Θ_{min} the minimum resolvable angle, L the distance between the sample and the detector, S_{CCD} the size of the detector and S_{pixel} the size of the pixel.
The CCD-camera in the experiments reported here has a pixel size of $S_{pixel} = 13.5\,\mu$m and a chip size of $S_{CCD} = 2048{\cdot}13.5\,\mu\text{m} = 27.648\,\text{mm}$.

In the case of the measurements in chapter 6 the distance $L \gtrapprox 220\,$mm is large compared to S_{CCD} leading to a maximum angle of $\Theta_{max} \lessapprox 7°$. Under the approximation of small angles, which means that $\sin(\arctan(\Theta)) \approx \Theta$, the equations of the shortest and largest resolvable distances go over into:

$$d_{min} \approx \frac{2\lambda\, L}{S_{CCD}} \qquad d_{max} \approx \frac{\lambda\, L}{2S_{pixel}} \quad . \tag{2.7}$$

The determination of the shortest resolvable distance is illustrated in figure 2.7, which shows the first order of the constructive interference for two different distances, d_1 is resolvable, d_2 is not.

2.3.2 Reference point

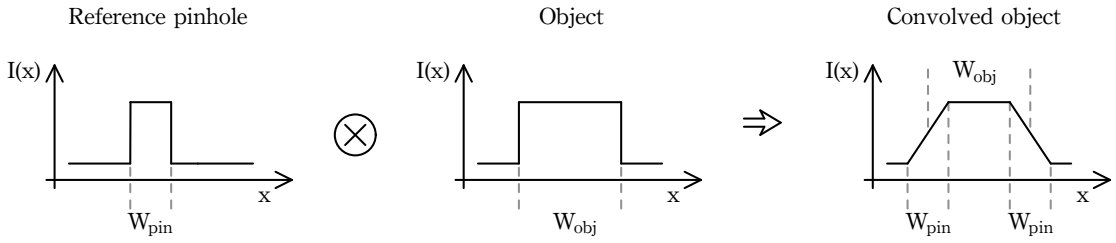

Figure 2.8: Illustration of the relation between diameter of the reference pinhole and the broadening of the convolved object

In addition to the diffraction limited resolution for a given pixelated detector, the reference points limit the resolution as well. In a multiple reference pattern, such as an URA-Pattern, the smaller the diameter of the pinholes the higher is the

resolution. Figure 2.8 shows this connection as 1D illustration. A pinhole with the width W_{pin} is convolved with an object represented as a rectangle with the width W_{obj} under the condition that $W_{pin} \ll W_{obj}$. The convolved object is broadened on both sides compared to the original object by W_{pin}, the diameter of the pinhole. In the HERALDO-Pattern, the shorter the transition between highest transmission and highest absorption at the corners or kinks the higher is the resolution. An illustration for this connection is found in figure 4.4 in section 4.4.
These geometry parameters of the holography mask are typically limited by micro- and nanostructuring abilities. In particular for soft X-rays high aspect ratio structures are required, which are difficult to manufacture. Focused Ion Beam Fabrication results are presented in section 5.4.

2.3.3 Modulation Transfer Function

The Modulation Transfer Function (MTF) is a measurable quantity showing to which extent the contrast of the original object at a specific frequency f is represented in the imaged object, seen in figure 2.9. The contrast transfer can be determined by a periodic line grating consisting of alternating white and black rectangular bars as the original object. By construction, this grating has a contrast of 100% at the grating spatial frequency f. In this case the MTF is also called Contrast Transfer Function. The MTF is defined as:

$$MTF(f) = \frac{M_{image}(f)}{M_{object}(f)} \quad . \tag{2.8}$$

M is the Michelson contrast, also known as modulation, either in the imaged object M_{image} or in the original object M_{object}. The Michelson contrast is defined as:

$$M = \frac{I_{max} - I_{min}}{I_{max} + I_{min}} \quad , \tag{2.9}$$

where I_{max} and I_{min} are defined as the maximum and the minimum value in the original and reconstructed object, respectively. An example of a MTF-diagram is seen in figure 2.10. The higher the spatial frequency the lower is typically the contrast transfer. The frequency at which the Michelson contrast M_{image} reaches the background level is called cutoff frequency. The cutoff frequency defines the upper limit for the obtainable resolution. All higher frequencies in the original object cannot be resolved.

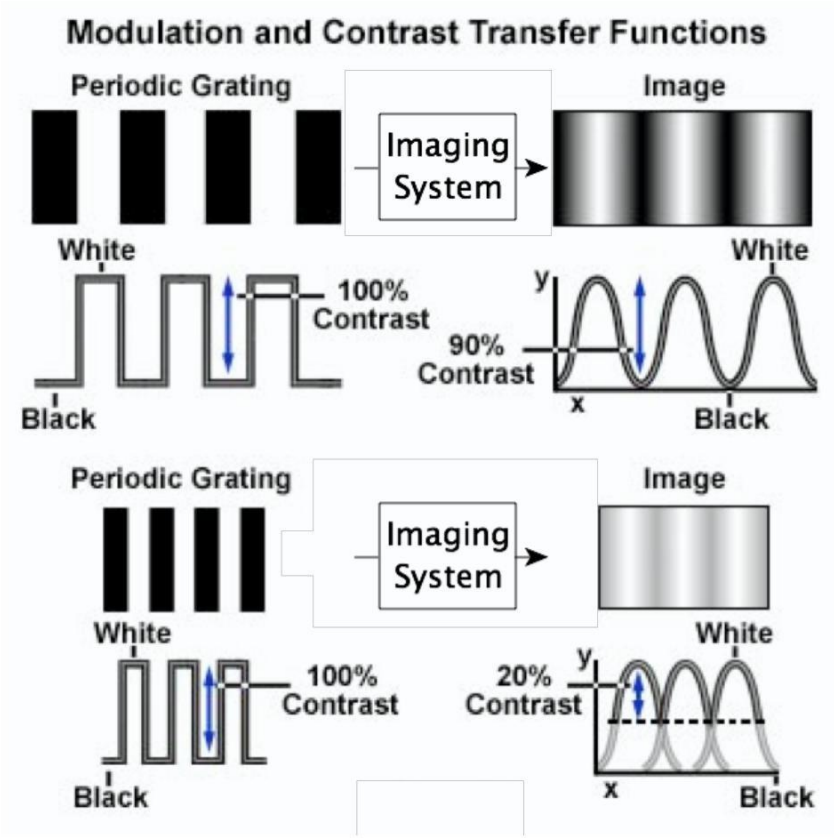

Figure 2.9: Illustration of the Modulation Transfer Function (MTF), which is identical to the Contrast Transfer Function when $M_{object} = 1$, for two different spacial frequencies; The object with a specific spatial frequency f is shown on the left side, whereas the image of the object is shown on the right side. The smaller the spacial frequencies the smaller is typically the contrast transfer. Modified from Reference [86]

For a 1D pixelated detector the Michelson contrast of the hologram fringe intensity is reduced to 90%, when one oscillation period is sampled by 5 pixels and M drops to 75% for sampling with 3 pixels [88].
Depending on the noise level in the experiment an effective smallest pixel size S'_{pixel} can be introduced in equation (2.7). If the noise corresponds to M=75%, $S'_{pixel} = 3 \cdot S_{pixel}$.

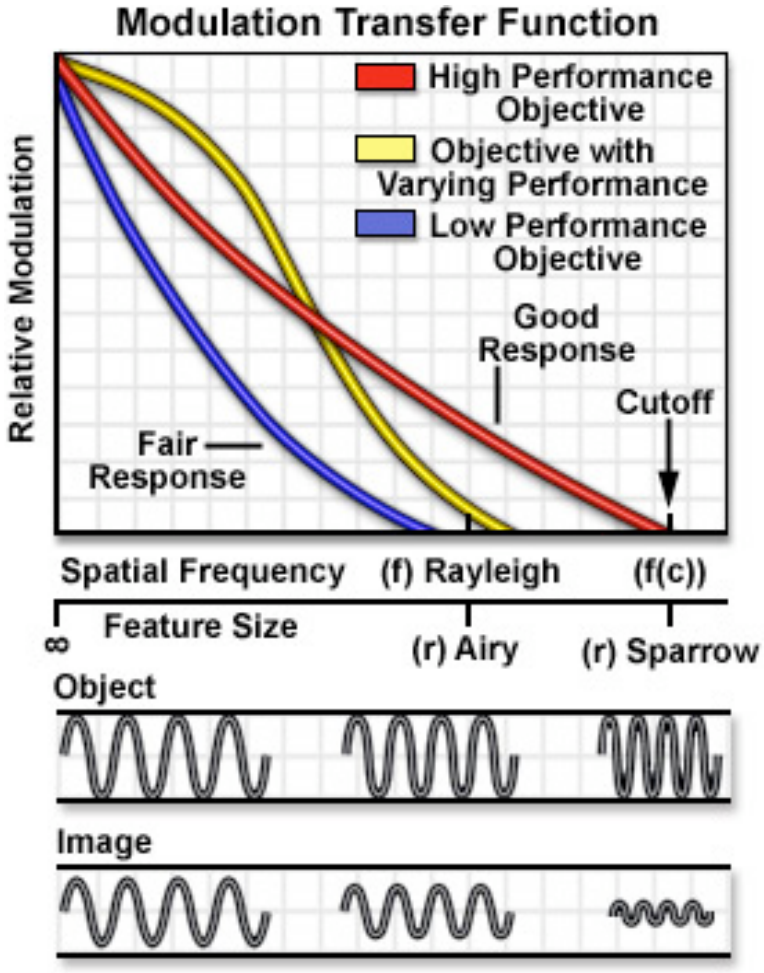

Figure 2.10: Illustration of the Modulation Transfer Function for all spacial frequencies until the cutoff frequency; The upper part shows the performance of three different imaging systems. A perfect imaging system would be a horizontal line without a cutoff frequency. The lower part shows three different frequencies in the object which are transferred by a non-perfect imaging system into frequencies with less contrast [86].

Chapter 3

Fourier Transform Holography with Uniformly Redundant Array (URA)

The URA-Pattern is a compact array of pinholes positioned in a specific arrangement, which has already been used as aperture in tomographic imaging [13], in imaging of Laser Driven Compression [32] and in astronomy for time-resolved and energy-resolved imaging [29].
Although the URA itself is known for a long time, the use as reference pattern in soft X-ray FTH started only recently [62, 22]. So far, the final reconstructions have been done in combination with a phase retrieval algorithm [89]. Here, a new way of reconstruction will be demonstrated without the need to use a phase retrieval algorithm.

3.1 Definition of an URA-Pattern

The URA-Pattern according to E.E. Fenimore and T.M. Cannon has a structure, in which each distance appears exactly as often as any other distances between the holes within this pattern [30]. It is constructed in the following way:

- The URA-Pattern is a matrix A with the dimensions of $r \times s$.
- The values of r and s are prime numbers.

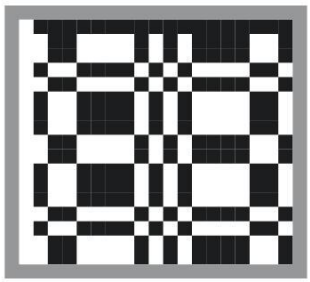

Figure 3.1: 17x19 Basic URA-Pattern from E. Caroli [15]; The black URA-Elements represent transparent areas, whereas the white URA-Elements represent opaque areas. The grey line is a frame to show the exact size of the Basic URA-Pattern. The meaning of the black and the white URA-Elements will be the same for all following figures.

- $r - s = 2$.
- The matrix element $A(i, j) = A(I, J)$, with $I = mod_r i$ and $J = mod_s j$.

The matrix elements are defined by the following list:

- $A(I, J) = 0$, if $I = 0$
- $A(I, J) = 1$, if $J = 0$ and $I \neq 0$
- $A(I, J) = 1$, if $C_r(I) \cdot C_s(J) = 1$
- $A(I, J) = 0$, otherwise.

$C_r(I)$ and $C_s(J)$ are defined by E.E. Fenimore and T.M. Cannon as:

- $C_r(I) = 1$, if $I = mod_r x^2$ where x is an integer and $1 \leq x < r$
- $C_r(I) = -1$, otherwise.

I is associated with r, the larger of the two prime numbers and J is associated with s.
An URA, which is the result of this definition, is called Basic URA-Pattern. An example for a Basic URA-Pattern is shown in figure 3.1. The matrix elements of the Basic URA-Pattern are called URA-Elements, which consist of ones and zeros standing for transparent and opaque areas, respectively.
At first one URA-Element is equal to one pixel. In later sections, one URA-Element will consist of 10 x 10 pixels in order to show effects related to transparent areas, whose shapes are round.

3.2 Reconstruction via deconvolution

Figure 3.2: Test object

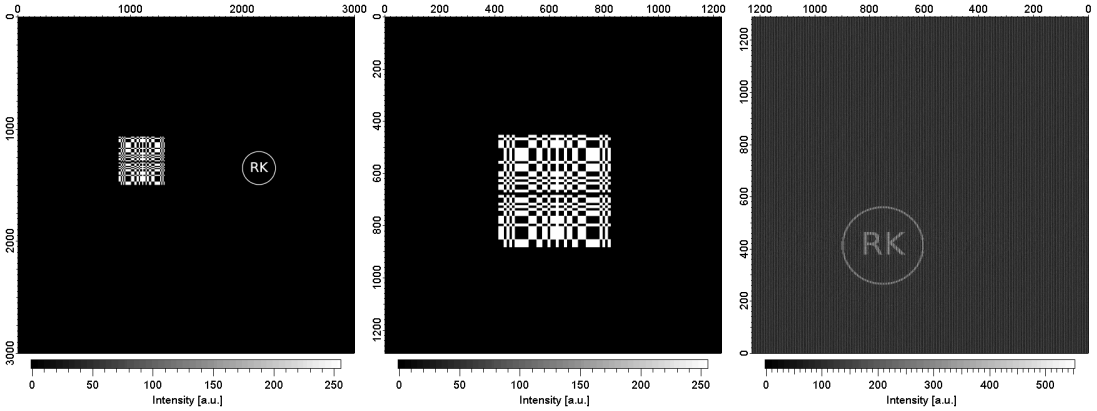

(a) Sample (b) URA-Pattern (c) Final reconstruction

Figure 3.3: Reconstruction via deconvolution; The x and y axes denote pixels of the matrix.

The URA-Pattern was constructed originally by E.E. Fenimore and T.M. Cannon [30] for the use as reference pattern via the reconstruction method described in section 3.3. Nevertheless, a deconvolution method can be used to reconstruct the object as well.

One of the two cross-correlations obtained via FTH is the convolution of the complex conjugate object with the reference pattern. An obvious way to reconstruct the object is to deconvolve this cross-correlation with the reference pattern.

The convolution with cc as the cross-correlation, o as the object, r as the reference and n as a noise term

$$cc = o \otimes r + n \tag{3.1}$$

can be written as a multiplication in Fourier space:

$$\mathscr{F}(cc) = \mathscr{F}(o) \cdot \mathscr{F}(r) + \mathscr{F}(n) \quad . \tag{3.2}$$

Transposing equation (3.2) to o leads to the equation of the deconvolution, which is:

$$o = \mathscr{F}^{-1}\left[\frac{\mathscr{F}(cc) - \mathscr{F}(n)}{\mathscr{F}(r)}\right] \quad , \tag{3.3}$$

with $\mathscr{F}^{-1}$ as the inverse Fourier transform.
The reconstruction via deconvolution is successful as long as the denominator does not have values near zero in its matrix. As soon as low values appear in the denominator, the reconstruction is covered by artifacts.

The URA-Pattern is such a reference pattern with low values. The reconstruction via deconvolution is covered by strong artifacts without a recognizable reconstructed object.
In order to reduce the artifacts in the reconstruction a filter will be used. A well-known filter for reducing these kinds of artifacts is the heuristic "Wiener filter". The heuristic "Wiener filter" is defined as:

$$R_{Wiener} = \frac{1}{\mathscr{F}(r)} \cdot \frac{|\mathscr{F}(r)|^2}{|\mathscr{F}(r)|^2 + K} \quad , \tag{3.4}$$

where K is a constant, which is determined experimentally [87]. As a note, the heuristic "Wiener filter" changes to an inverse filter, when K=0.
The reconstruction via deconvolution with a "Wiener filter" is:

$$o = \mathscr{F}^{-1}\big[R_{Wiener} \cdot \mathscr{F}(cc)\big] \quad . \tag{3.5}$$

For demonstration purpose an object, seen in figure 3.2, is convolved with the URA-Pattern, seen in figure 3.3b, via FTH. Noise is included as a Poisson distribution and the "Wiener filter" approach is used in order to reconstruct the object. For a low K-value of K=1e^{-6} the reconstruction via deconvolution in figure 3.3c could be achieved, which shows the properly reconstructed object without very strong artifacts.

3.3 Reconstruction via convolution

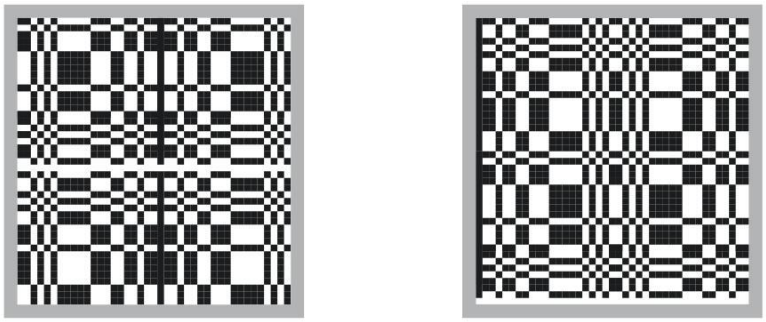

(a) Basic URA-Pattern 1 (b) Basic URA-Pattern 2

Figure 3.4: Different Basic URA-Patterns generated the same way, but translated to each other

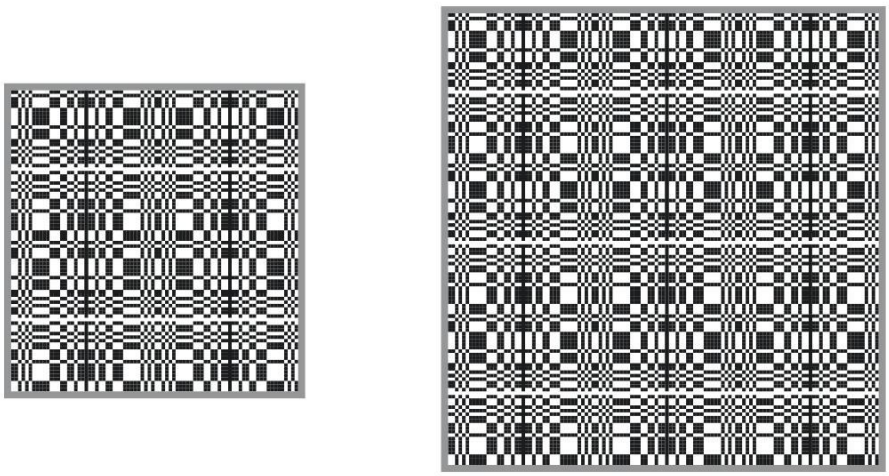

(a) Reference URA-Pattern (b) Reconstruction URA-Pattern

Figure 3.5: The Reference URA-Pattern and the Reconstruction URA-Pattern with the same Basic URA-Pattern used by E.E. Fenimore and T.M. Cannon

The consideration of the specific characteristic of an URA-Pattern, meaning the equal amount of all distances within the URA-Pattern, leads to one single peak at $|q|=0$ and a relatively flat background with an approximately constant value in Fourier space. The variations of the otherwise smooth background are minor,

negligible peaks, which exist due to the finite size of the URA-Elements.

The cross-correlation of the object with the URA-Pattern contains the reconstructed object, if:

1. The URA-Pattern is not surrounded by empty space.

2. The matrix of the URA-Pattern has the same size as the matrix in which the cross-correlation is entirely embedded.

The first point is important since the surrounding empty space creates a strong interference pattern in Fourier space destroying the characteristics of the URA-Pattern. The second point seems to be trivial. However, it should be remembered that the convolution of two extended objects leads to a cross-correlation, which is larger than either one of the two objects and, therefore, denying point one.

E.E. Fenimore and T.M. Cannon [30] found a solution to this dilemma by correlating the cross-correlation with a second URA-Pattern. The second URA-Pattern is based on a Basic URA-Pattern, which is either identical or translated, as seen in figure 3.4, to the Basic URA-Pattern of the first URA-Pattern. It considers both points by putting copies of one Basic URA-Pattern side by side in x and in y direction, called mosaicing. The number of Basic URA-Patterns in the second URA-Pattern depends especially on the size of the first one, since the number of Basic URA-Patterns in the first URA-Pattern can be increased as well. As a result a large second URA-Pattern is created, which has no surrounding empty space and is larger than the cross-correlation.

In the publication of reference [30], E.E. Fenimore and T.M. Cannon demonstrate the concept with a 2x2 mosaiced first URA-Pattern and a 3x3 mosaiced second URA-Pattern, shown in figure 3.5.

In FTH the situation is slightly different to the situation in reference [30]. Taking the complex conjugate cross-correlation, the correlation method of reference [30] goes over into a convolution method:

$$o' = o \otimes r^* \otimes g \quad . \tag{3.6}$$

Here, o is the original object and o' the reconstructed object. The first URA-Pattern r is named as the Reference URA-Pattern, whereas the second URA-Pattern g is named as the Reconstruction URA-Pattern.
The complex conjugate cross-correlation is cut out of the Fourier transformed hologram and convolved with the Reconstruction URA-Pattern. The Reconstruction URA-Pattern can consist of many Basic URA-Patterns, each of them reconstructing the original object. No upper limit exists for the number of Basic URA-Patterns in the Reconstruction URA-Pattern, therefore, no upper limit exists for the number of reconstructed objects as seen in figure 3.6c and figure 3.6e.
For the final reconstruction more conditions, as said above, have to be considered:

1. The object must be smaller than the Basic URA-Pattern, since the reconstructed objects in the final reconstruction have a periodicity equal to the size of the Basic URA-Pattern.

2. A higher number of Basic URA-Patterns in the Reference URA-Pattern increases the contrast.

3. The Basic URA-Patterns in both, the Reference URA-Pattern and the Reconstruction URA-Pattern, might not be identical or translated to each other, when the URA-Elements consist of more than one pixel. The structure within the URA-Elements can differ as will be explained in section 3.3.1. Nevertheless, the arrangement of the URA-Elements within both Basic URA-Patterns as well as the URA-Element sizes are identical.

In figure 3.6 four final reconstructions are presented. The first column shows two final reconstructions, in which the Reconstruction URA-Pattern has no additional empty space. The second column shows two final reconstructions in which the Reconstruction URA-Pattern is enlarged by an empty line and an empty row. Figure 3.6a and figure 3.6b show the appropriate Reconstruction URA-Patterns for the final reconstructions of figure 3.6c and of figure 3.6d, respectively. In figure 3.6b the additional empty space is marked by red lines.
The comparison of figure 3.6c with figure 3.6d shows that the additional space in the Reconstruction URA-Pattern creates a strong overlaying artifact, disturbing the reconstructed objects.
Although increasing the number of Basic URA-Patterns in the Reconstruction URA-Pattern does not change the quality of the final reconstruction, seen in the

comparison of figure 3.6c with figure 3.6e, the ratio between the size of the Reconstruction URA-Pattern versus the added empty space is visible in the artifacts, as seen in the comparison of figure 3.6d with figure 3.6f. The higher the ratio the less pronounced are the artifacts. This concludes, if the additional empty space cannot be avoided, e.g. the matrix has to be even in both dimensions, increasing the number of Basic URA-Patterns will still reveal reconstructed objects without artificial overlap, as seen in figure 3.6f.

In figure 3.7 the entire process from the illumination to the final reconstruction is shown. The beam illuminates the entire sample which is detected in the far field by a CCD-camera. The hologram is Fourier transformed and leads to the conventional reconstruction. The complex conjugate cross-correlation is cut out and convolved with the Reconstruction URA-Pattern leading to the final reconstruction.

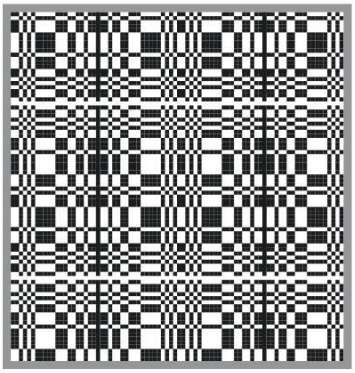

(a) 2x2 Reconstruction URA-Pattern; matrix with 82x86 pixels; without additional empty space

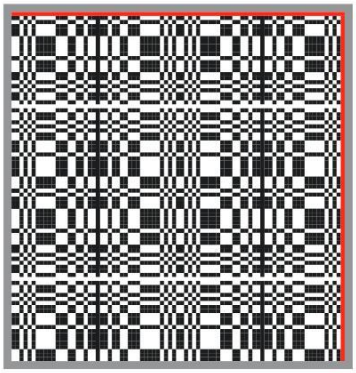

(b) 2x2 Reconstruction URA-Pattern; matrix with 83x87 pixels; one empty row and one empty line marked in red

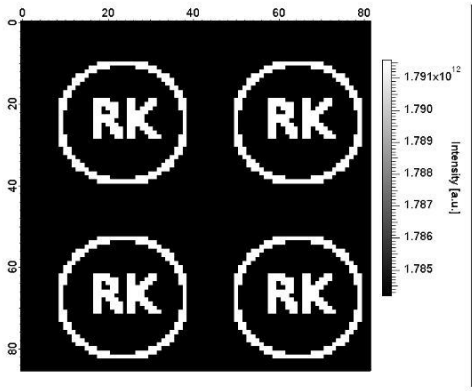

(c) Reconstruction with a 2x2 Reconstruction URA-Pattern without additional empty space

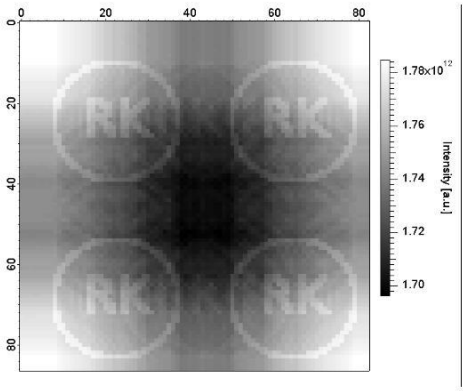

(d) Reconstruction with a 2x2 Reconstruction URA-Pattern with one empty row and one empty line

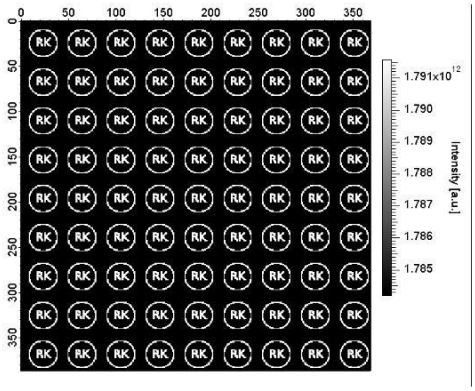

(e) Reconstruction with a 9x9 Reconstruction URA-Pattern without additional empty space

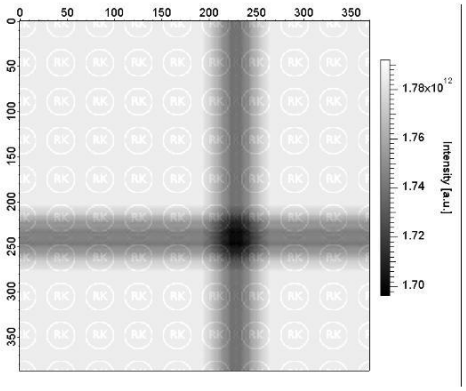

(f) Reconstruction with a 9x9 Reconstruction URA-Pattern with one empty row and one empty line

Figure 3.6: Influence of the Reconstruction URA-Pattern on the quality of the final reconstruction; The x and y axes denote pixels of the matrix.

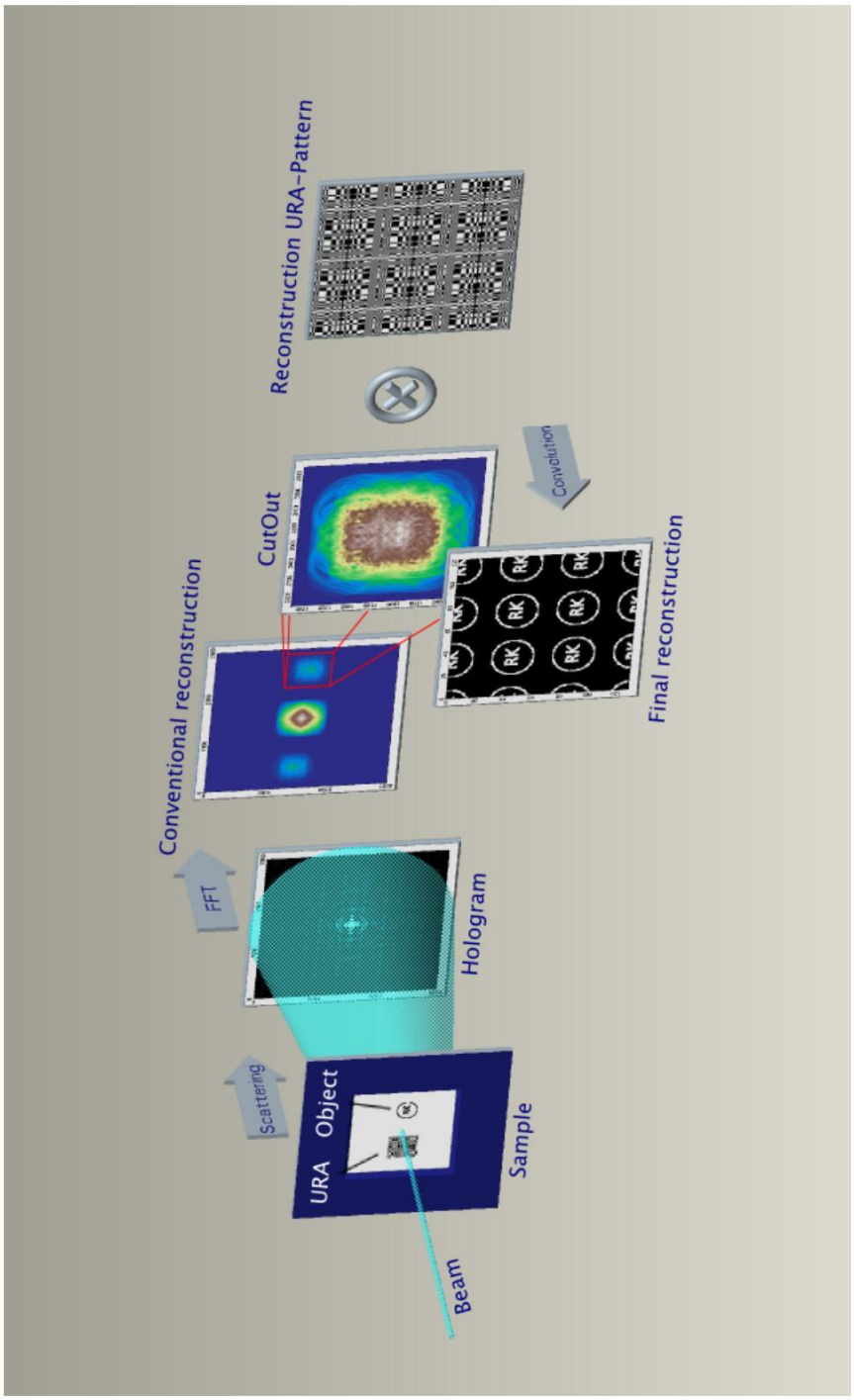

Figure 3.7: The principle for FTH via convolution; The scattered light from the exit surface of the entirely illuminated sample is detected by a CCD-camera. The complex conjugate cross-correlation from the Fourier transformed hologram is convolved with the Reconstruction URA-Pattern resulting in the reconstructed objects.

3.3.1 Ratio of spacing to hole diameter (RSH)

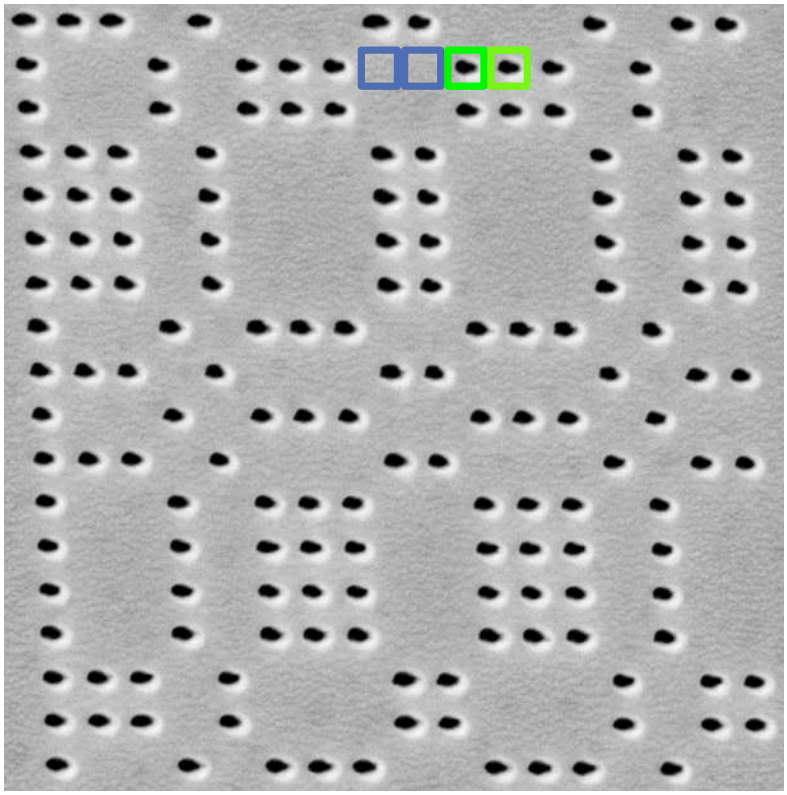

Figure 3.8: SEM-picture of an URA-Pattern with round holes; The blue squares are examples for opaque URA-Elements, whereas the green squares are examples for transparent URA-Elements.

The self-supporting Reference URA-Pattern produced by a Focused Ion Beam (FIB), an example is seen in figure 3.8, cannot be described with one pixel per URA-Element. One pixel can only represent either a transparent or an opaque area. A Reference URA-Pattern with URA-Elements consisting of only one pixel each is, therefore, not self-supporting. Though experiments with a not self-supporting Reference URA-Pattern exist [62], here only a Reference URA-Pattern is considered in which the transparent areas are milled through the entire layers requiring a self-supporting reference pattern.
In order to simulate a self-supporting Reference URA-Pattern, the number of pixels within one URA-Element is increased to 10 x 10 pixels. Whereas the opaque URA-Elements represent opaque areas, each transparent URA-Element represents

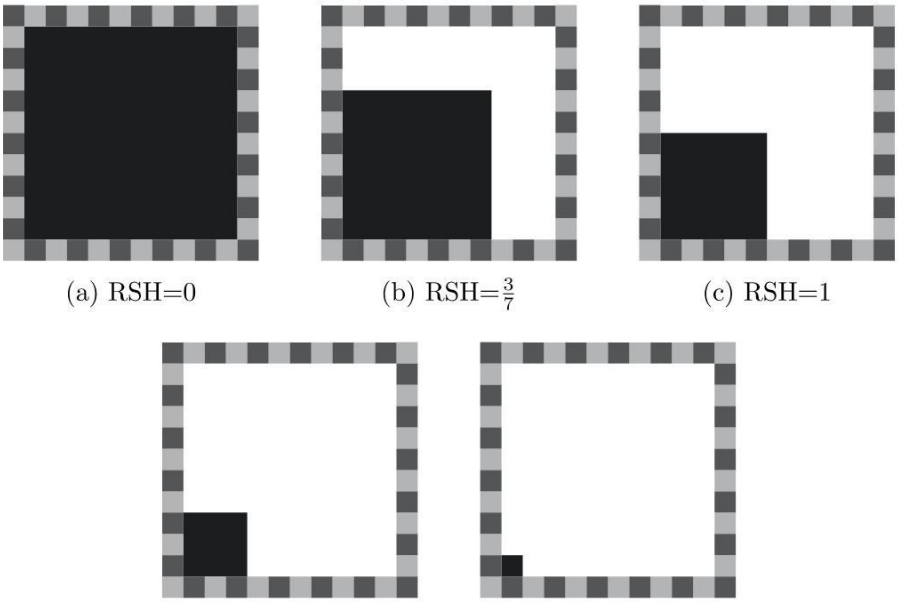

(a) RSH=0 (b) RSH=$\frac{3}{7}$ (c) RSH=1

(d) RSH=$\frac{7}{3}$ (e) RSH=9

Figure 3.9: Transparent URA-Elements with a size of 10x10 pixels and with different RSH-values; The border can be used to verify the RSH-value.

one hole with the size equal to one or several transparent pixels and with its surrounding opaque pixels. Furthermore, in this and in the next two sections, the transparent URA-Elements are identical to each other.
In figure 3.9 different transparent URA-Elements are shown. The black pixels represent transparent areas, whereas the white pixels represent opaque areas. In figure 3.10 the appropriate Basic URA-Patterns are shown.

The filling of opaque and transparent pixels in one dimension within a transparent URA-Element can be characterized by a ratio, called ratio of spacing to hole diameter (RSH). RSH is defined as:

$$\mathrm{RSH} = \frac{\mathrm{N}_O}{\mathrm{N}_T} \quad , \tag{3.7}$$

where N_O is the number of opaque and N_T the number of transparent pixels.

The influence in the final reconstruction of different RSH-values in the Reference and in the Reconstruction URA-Pattern is investigated in the following simulations.
Since the RSH-value in the Reference URA-Pattern can vary due to different influ-

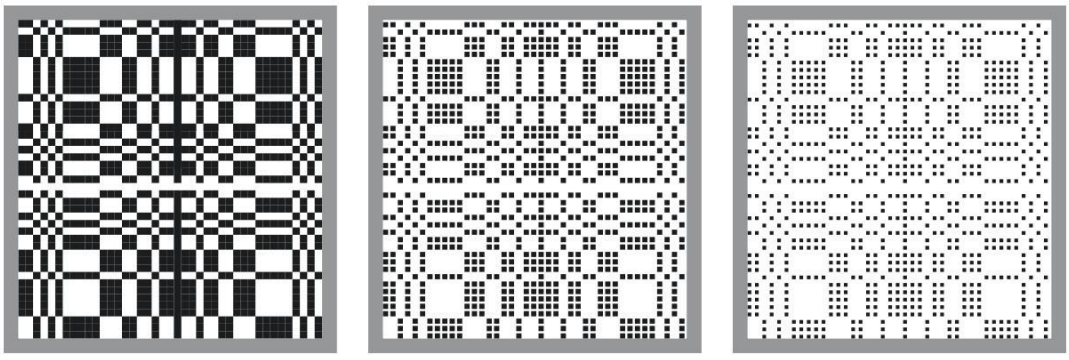

(a) RSH=0 (b) RSH=$\frac{3}{7}$ (c) RSH=1

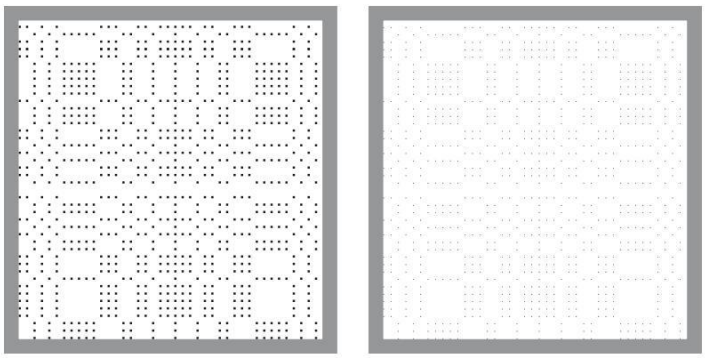

(d) RSH=$\frac{7}{3}$ (e) RSH=9

Figure 3.10: Basic URA-Patterns with different RSH-values

ences in the milling process, the RSH-value for the Reference URA-Pattern in the simulation is varied accordingly. The Reference URA-Pattern in the simulations consists of only one Basic URA-Pattern and has different RSH-values, which are RSH=$\frac{3}{7}$, RSH=1, RSH=$\frac{7}{3}$ and RSH=9.

The Reconstruction URA-Pattern consists of 10 x 10 pixels in its URA-Elements as well and is mosaiced by 3x3 Basic URA-Patterns. In order to find a way to reconstruct the object successfully without the use of a phase retrieval algorithm, the simulations are done with two different RSH-values in the Reconstruction URA-Pattern. At first the RSH-value of the transparent URA-Elements in the Reconstruction URA-Pattern is identical to the RSH-value of the transparent URA-Elements in the Reference URA-Pattern. In figure 3.11 these reconstructions are shown. In neither of the final reconstructions the quality is satisfying.

In figure 3.12 the final reconstructions are presented in which the RSH-value of the

Reconstruction URA-Patterns is RSH=0. RSH=0 for the Reconstruction URA-Pattern is kept constant for each simulation, independent of the RSH-value in the Reference URA-Pattern. All final reconstructions are perfect, neither artifacts nor a reduced quality is visible.

The simulations in this section show the ability of the reconstruction method via convolution to achieve a perfect reconstruction without a phase retrieval algorithm, when the RSH-value in the Reconstruction URA-Pattern is zero. In this case and as long as all transparent URA-Elements are identical within one URA-Pattern, the quality of the final reconstruction is independent of the RSH-value in the Reference URA-Pattern.

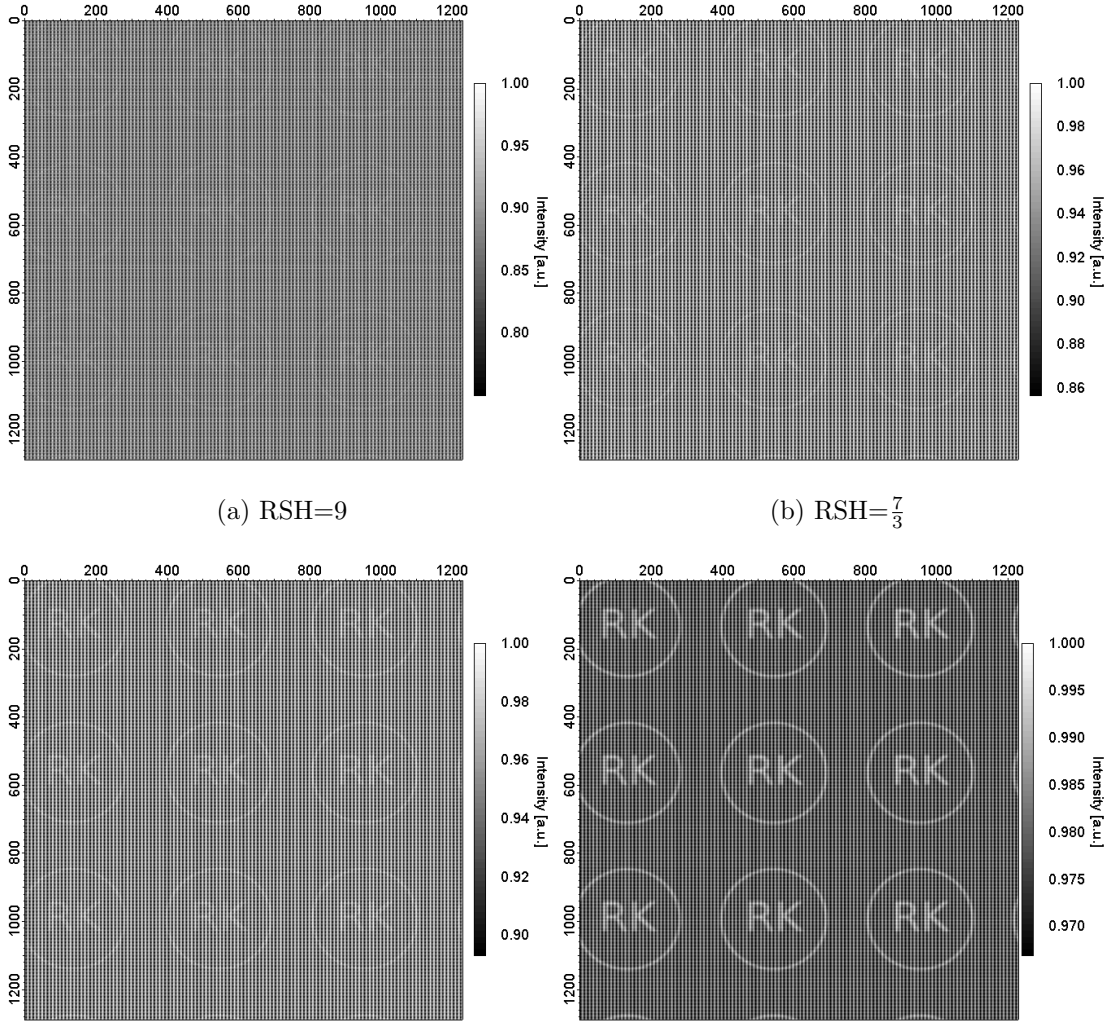

(a) RSH=9

(b) RSH=$\frac{7}{3}$

(c) RSH=1

(d) RSH=$\frac{3}{7}$

Figure 3.11: Final reconstructions with different RSH-values in the Reference URA-Pattern; The RSH-values in the Reconstruction URA-Pattern are identical to the RSH-values in the Reference URA-Pattern. The x and y axes denote pixels of the matrix.

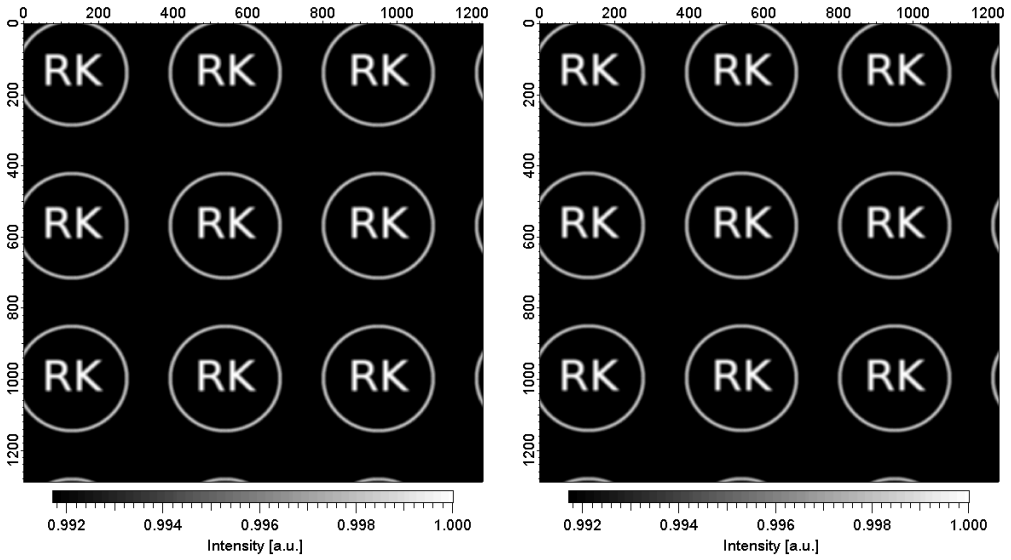

(a) RSH=9

(b) RSH=$\frac{7}{3}$

(c) RSH=1

(d) RSH=$\frac{3}{7}$

Figure 3.12: Final reconstructions with different RSH-values in the Reference URA-Pattern and a constant RSH=0 in the Reconstruction URA-Pattern; The x and y axes denote pixels of the matrix.

3.3.2 Mismatch of the URA-Element sizes

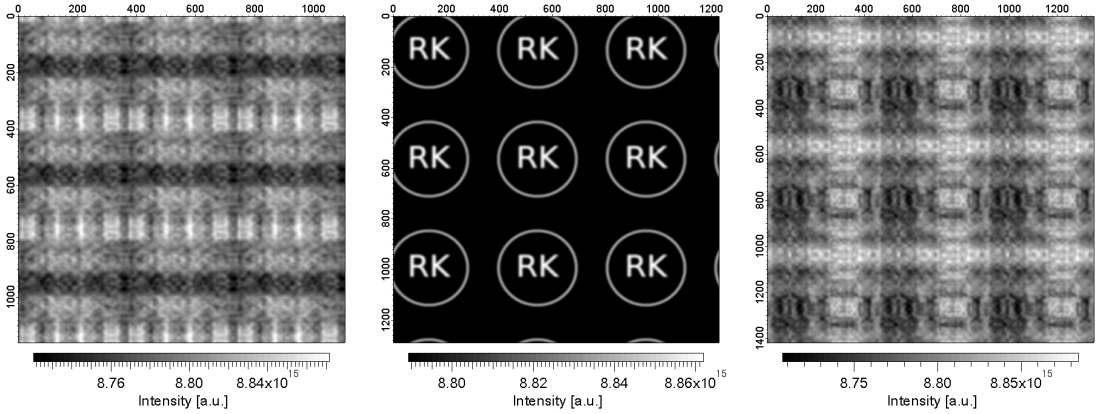

(a) Element size of 9 pixels in the Reconstruction URA-Pattern

(b) Element size of 10 pixels in the Reconstruction URA-Pattern

(c) Element size of 11 pixels in the Reconstruction URA-Pattern

Figure 3.13: Reconstruction of an object convolved via FTH with the same Reference URA-Pattern with an URA-Element size of 10 pixels, but with different Reconstruction URA-Patterns; The x and y axes denote pixels of the matrix.

In order to reconstruct an object properly, the size of the URA-Elements in the Reconstruction URA-Pattern has to be identical to the size of the URA-Elements in the Reference URA-Pattern. It can easily happen that in a real experiment the correct size of the URA-Elements in the Reference URA-Pattern is hard to determine.

As will be shown in the experiments of chapter 6 one way to determine the size of the URA-Elements is to modify the sample within the production cycle by adding a single pinhole near the Reference URA-Pattern. With the help of this additional pinhole, the URA-Pattern is imaged via conventional FTH, when the separation conditions are fulfilled. The reconstructed URA-Pattern defines the URA-Element size of the Reconstruction URA-Pattern.

In the following the consequences will be investigated, when it is not possible to determine the correct URA-Element size for the Reconstruction URA-Pattern. In figure 3.13 three reconstructions are shown. In all three reconstructions the Reference URA-Pattern is identical, it consists of one Basic URA-Pattern with

RSH=0 and an URA-Element size of 10x10 pixels. The Reconstruction URA-Patterns are mosaiced of 3x3 Basic URA-Patterns with RSH=0, but different URA-Element sizes.
The only successful reconstruction is found, when the Reconstruction URA-Pattern has an URA-Element size of 10x10 pixels as well, meaning when the URA-Element size in the Reconstruction URA-Pattern is identical to the URA-Element size in the Reference URA-Pattern. This is seen in figure 3.13b.
As soon as the URA-Element size differs by $\pm 10\%$, the final reconstructions are not successful anymore. The final reconstructions with a Reconstruction URA-Pattern of an URA-Element size of 9x9 pixels and of an URA-Element size of 11x11 pixels are seen in figure 3.13a and figure 3.13c, respectively. Both final reconstructions show no detail of the object.

3.3.3 Imperfect illumination

The correct coherent illumination of the sample with an URA-Pattern as reference is important. In a sample with an URA-Pattern as reference all holes of the URA-Pattern contribute to the same reconstructed object. Therefore, the lack of a homogeneous and coherent illumination is clearly visible in the final reconstruction. Four scenarios are investigated in this section.

1. The Reference URA-Pattern and the object are both illuminated coherently without spatial intensity variation.

2. The Reference URA-Pattern is illuminated with an intensity gradient described by a linear slope, ranging from 0 to 1. The object is illuminated with constant intensity.

3. The Reference URA-Pattern and the object are illuminated by a Gaussian beam profile, which has a FWHM of 911 pixels.

4. The Reference URA-Pattern and the object are illuminated by a Gaussian beam profile, which has a FWHM of 527 pixels.

Whereas the different illuminated samples are seen in figure 3.14, the final reconstructions are seen in figure 3.15. All scenarios are reconstructed with 3x3

mosaiced Reconstruction URA-Patterns with RSH=0.
As expected the first scenario, shown in figure 3.14a, delivers perfectly reconstructed objects, seen in figure 3.15a.
As soon as the object and the Reference URA-Pattern are not homogeneously illuminated, the final reconstructions get noticeable worse. Since the exit surface of the object is imaged, the inhomogeneously illuminated object is reconstructed according to the intensity of illumination, whereas the inhomogeneously illuminated Reference URA-Pattern will lead to strong artifacts.

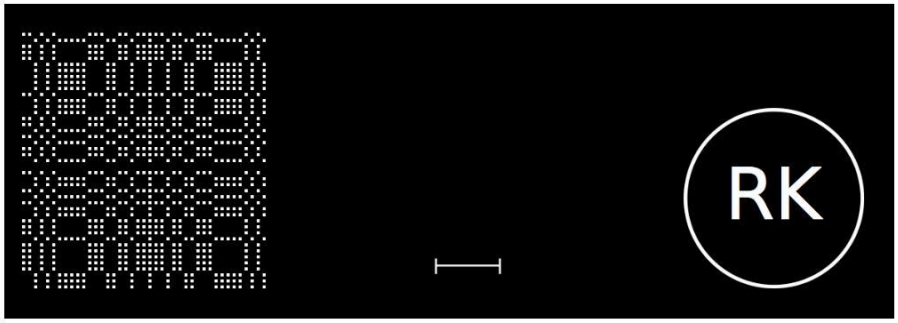

(a) First scenario

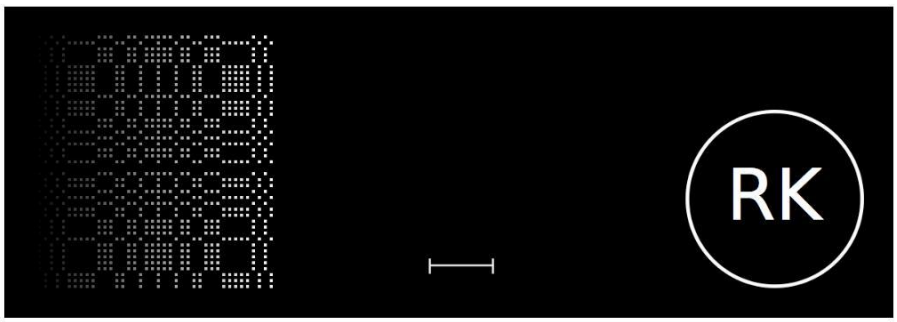

(b) Second scenario

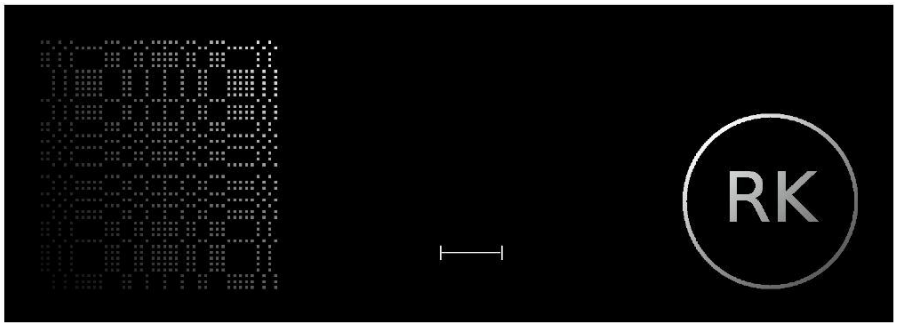

(c) Third scenario

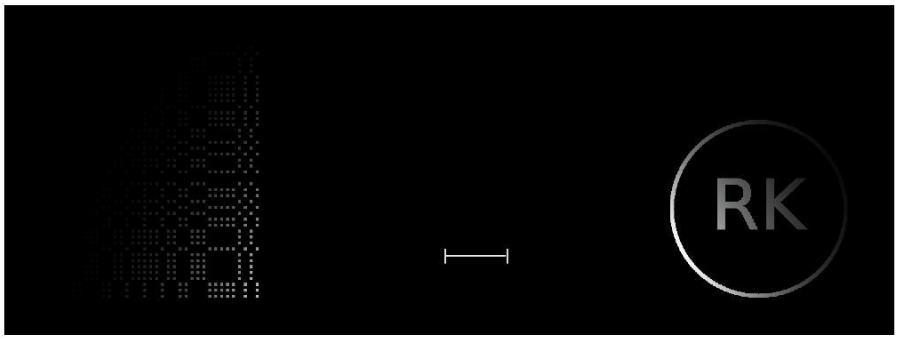

(d) Fourth scenario

Figure 3.14: Four scenarios with the same sample and a different coherent illumination; The scale bar denotes 100 pixels.

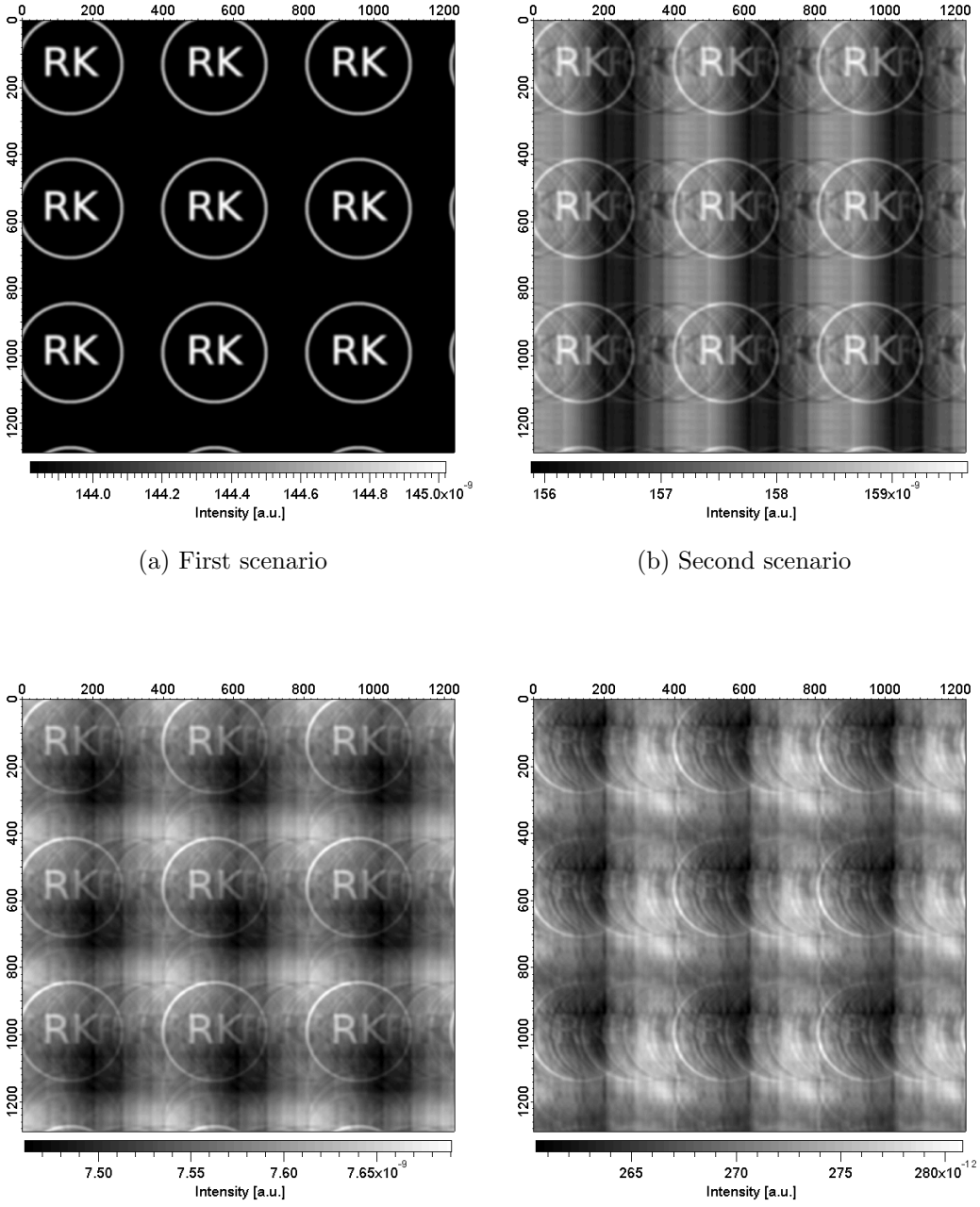

(a) First scenario

(b) Second scenario

(c) Third scenario

(d) Fourth scenario

Figure 3.15: Final reconstructions of the four scenarios with differently illuminated samples; The x and y axes denote pixels of the matrix.

3.3.4 Imperfect production

In section 3.3.1 the ability to reconstruct an object properly with a Reconstruction URA-Pattern, which has RSH=0, is explained. The condition for such a perfect reconstruction is that all transparent URA-Elements in the Reference URA-Pattern are identical. In this case the exact structure within the transparent URA-Elements can be neglected.
As soon as the transparent URA-Elements are not identical to each other, the final reconstruction deteriorates. Two parameters, which can influence the quality of the final reconstruction are:

1. The sizes of the holes within the transparent URA-Elements
2. The positions of the holes within the transparent URA-Elements.

In figure 3.16 the Reference URA-Patterns as well as the associated reconstructions can be seen.
Comparing the reconstructions of figures 3.16b and 3.16d discloses that the different positions of the holes lead to an uneven background with only slight artifacts in the signal intensity of the object. Although the hole diameter is equal, the different spacings between the holes destroy the characteristics of the URA-Pattern. The same happens, when the sizes of the holes differ in the Reference URA-Pattern. The different hole sizes lead to different spacings and destroy once more the characteristics of the URA-Pattern. In addition, the different individual hole sizes contribute individual images with different resolutions to the final image. As all holes in the Reference URA-Pattern contribute to the final reconstructed object, the different hole sizes result in a reduction of the quality in the final reconstruction.

These investigations lead to the conclusion that it is important to observe hole sizes and hole positions while producing a Reference URA-Pattern. Differences in hole sizes and in hole positions will worsen the final reconstruction.
Examples for mispositioned holes and for an imperfection of hole sizes in a Reference URA-Pattern produced by FIB-milling are presented in figure 3.17 and figure 3.18, respectively. Details of the FIB-production process will be discussed in section 5.4.

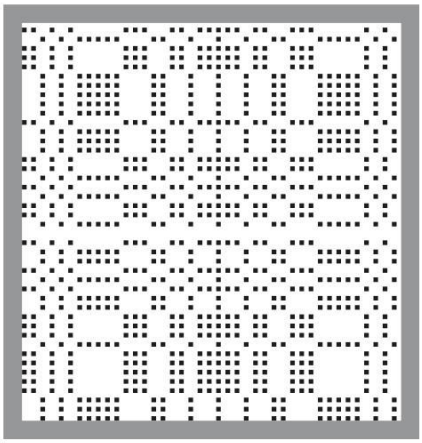

(a) Basic URA-Pattern with perfectly produced holes

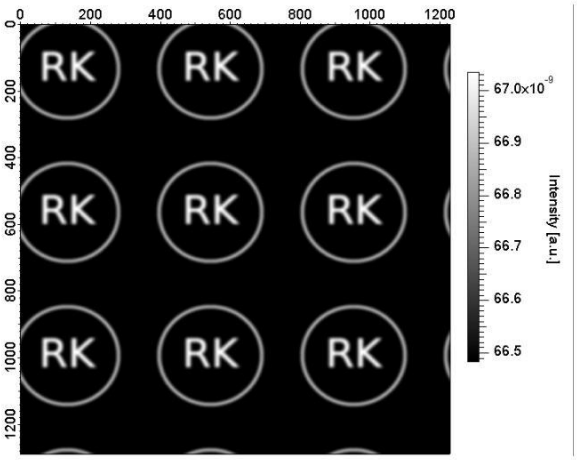

(b) Final Reconstruction with perfectly produced holes in the Reference URA-Pattern

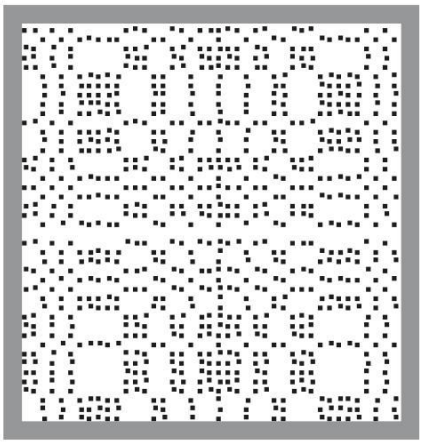

(c) Basic URA-Pattern with different hole positions

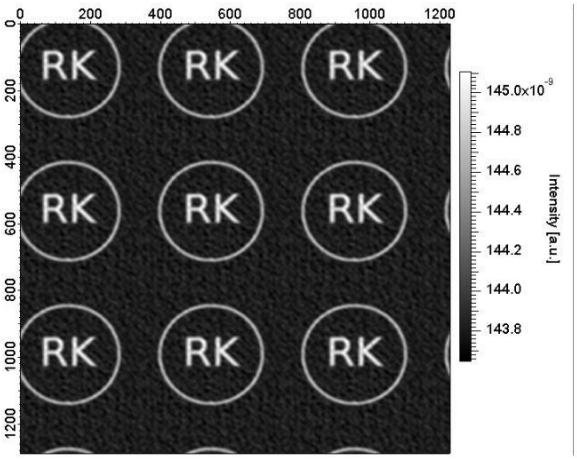

(d) Final Reconstruction with different hole positions in the Reference URA-Pattern

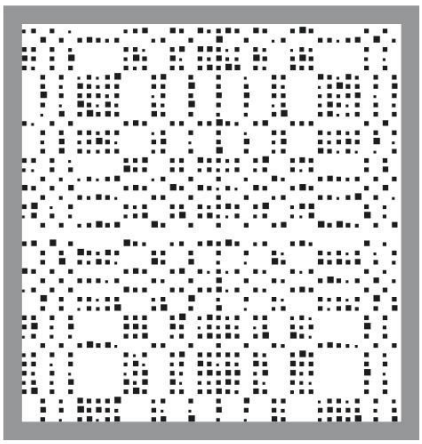

(e) Basic URA-Pattern with different hole sizes

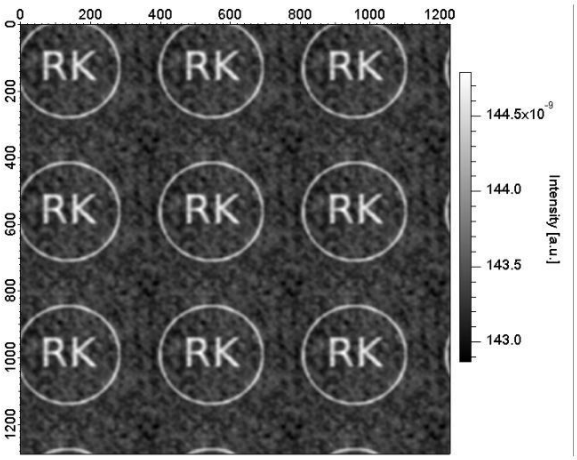

(f) Final Reconstruction with different hole sizes in the Reference URA-Pattern

Figure 3.16: Final reconstructions showing the quality of the production of a Reference URA-Pattern; The x and y axes denote pixels of the matrix.

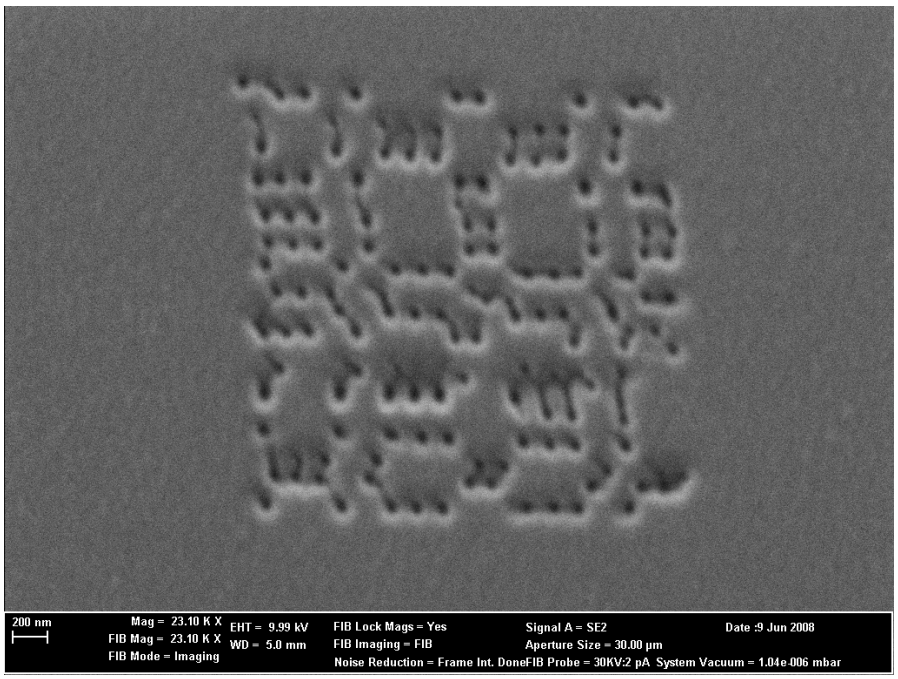

Figure 3.17: Example for imperfect hole positions in the Reference URA-Pattern

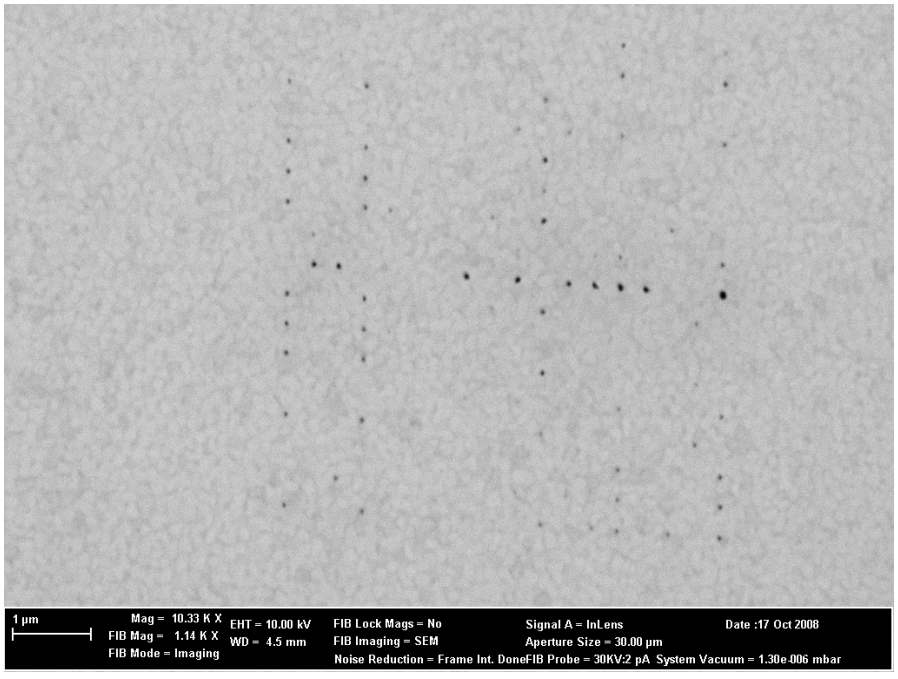

Figure 3.18: Example for imperfect hole sizes in the Reference URA-Pattern

Chapter 4

Fourier Transform Holography with Extended Reference by Autocorrelation Linear Differential Operation (HERALDO)

FTH with a HERALDO-Pattern leads to a completely different reconstruction method compared to the reconstruction methods using multiple references. In HERALDO the reference points are mathematically generated after the hologram is detected.
Furthermore, the HERALDO-Pattern can be adjusted according to the sample of investigation due to the high flexibility for different reference patterns.

Principle of HERALDO

In figure 4.1 the principle of HERALDO compared to conventional FTH is illustrated. In the first line the reconstruction via conventional FTH is shown, whereas in the second line the reconstruction via HERALDO is seen. Both reconstruction methods are based on the same concept, the original object is convolved with a reference point leading directly to the reconstructed object. The difference lies in

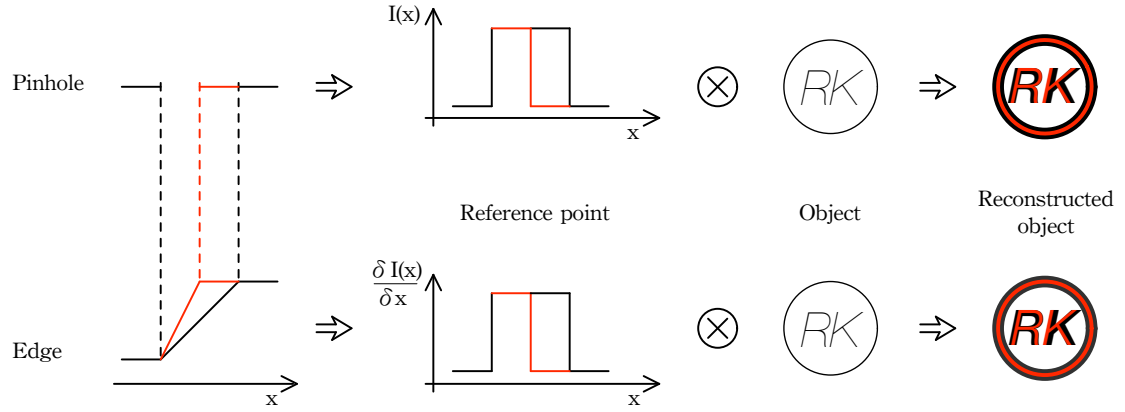

Figure 4.1: Comparison between conventional FTH and HERALDO; The upper line shows the reconstruction via conventional FTH, whereas the lower line shows the reconstruction via HERALDO. Two different sizes of reference points are shown: red: smaller reference point, black: larger reference point. The resulting final reconstructions are seen in the right pictures, which demonstrate the effect of different resolutions.

the reference point itself. Whereas in conventional FTH, the reference point is a single pinhole, the reference point in HERALDO must be mathematically generated by taking the derivative, for instance at the endpoints of a line.
In both methods the resolution of the reconstructed object depends on the quality of the reference point. Whereas the resolution in conventional FTH depends on the diameter of the pinhole, the resolution in HERALDO depends on the transition between highest transmission and highest absorption along the derivative is taken at a corner of a reference. The shorter the transition the higher is the resolution. In addition to the resolution, the contrast in the final reconstruction can be influenced by the HERALDO-Pattern as well, contrary to conventional FTH. The contrast in the final reconstruction is higher the higher the transmission difference between highest transmission and highest absorption at the corner of a reference. The relation between transmission difference and contrast is quadratic. Increasing the transmission difference by a factor of two leads to a contrast increase by a factor of four. An illustration is seen in figure 4.2.

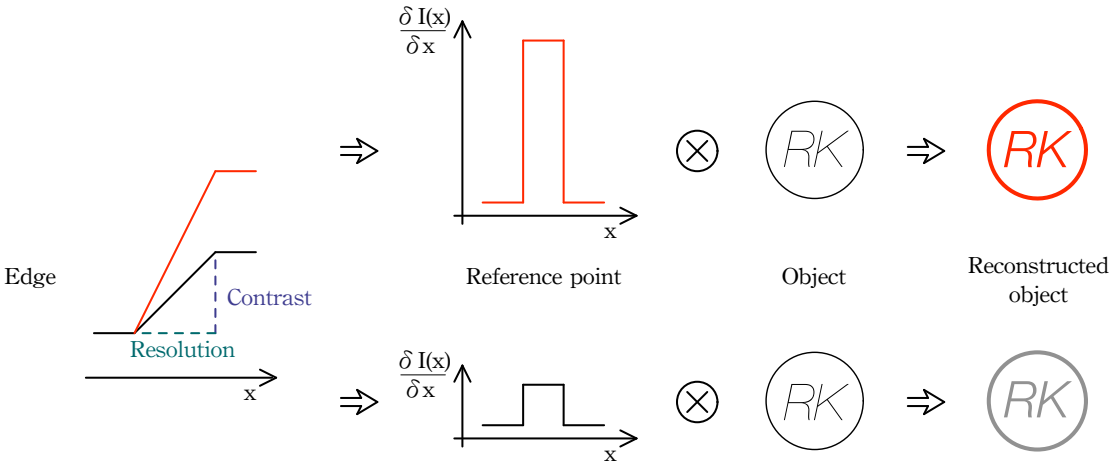

Figure 4.2: Illustration of the relation between transmission difference and contrast in the final reconstruction

4.1 Differential operator

4.1.1 General linear differential operator

The concept of using the HERALDO-Pattern as reference is to reconstruct the object by applying a n-th order linear differential operator:

$$\mathscr{L}^{(n)}\{\cdot\} \equiv \sum_{k=0}^{n} a_k \frac{\partial^n}{\partial x^{n-k}\partial y^k}\{\cdot\} \tag{4.1}$$

onto the autocorrelation of the entire sample leading to:

$$\mathscr{L}^{(n)}\{f \otimes f^*\} = \mathscr{L}^{(n)}\{o \otimes o^*\} + \mathscr{L}^{(n)}\{r \otimes r^*\} + \mathscr{L}^{(n)}\{o \otimes r^*\} + \mathscr{L}^{(n)}\{r \otimes o^*\}\,. \tag{4.2}$$

Considering the separation conditions for the HERALDO-Pattern the last two terms can resolve the object, when the linear differential operator applied on the reference $r(x, y)$ will lead to:

$$\mathscr{L}^{(n)}\{r(x,y)\} = A\delta(x - x_0)\delta(y - y_0) + g(x,y) \quad , \tag{4.3}$$

where A is an arbitrary complex-valued constant and $g(x, y)$ reflects the geometry of the extended reference. If a linear differential operator, solving equation (4.3), can be found, the following identities are used in order to resolve the object:

$$\mathscr{L}^{(n)}\{o \otimes r^*\} = (-1)^n \left[o \otimes \mathscr{L}^{(n)}\{r^*\}\right] \tag{4.4}$$

$$\mathscr{L}^{(n)}\{r \otimes o^*\} = \mathscr{L}^{(n)}\{r\} \otimes o^* \quad . \tag{4.5}$$

Using only the first summand of equation (4.3) by making the assumption that the function $g(x, y)$ is zero around the position of the δ-functions at (x_0, y_0) and $(-x_0, -y_0)$ with at least a radius equal to the radius of the object and negligible elsewhere, the following equations are obtained:

$$\mathscr{L}^{(n)}\{o \otimes r^*\} = (-1)^n A^* o(x + x_0, y + y_0) \tag{4.6}$$

$$\mathscr{L}^{(n)}\{r \otimes o^*\} = A\, o^*(x - x_0, y - y_0) \quad . \tag{4.7}$$

Here, the shifting property of the δ-function is used. Equations (4.6) and (4.7) show the ability to reconstruct the object properly, if an appropriate linear differential operator is found and applied onto the cross-correlation.
In reference [40] different HERALDO-Patterns and their appropriate linear differential operators are shown. In this thesis a slit as reference will be investigated and the appropriate $\mathscr{L}^{(n)}$ is the first derivative in the direction of this slit, which is approximated as a line.

4.1.2 Linear differential operator for a slit

The appropriate linear differential operator for a slit is derived along the x-axis at first in a non-rotated and secondly, in a rotated system. The rotated and the non-rotated system enclose the included angle α.

Non-rotated system

A line with the length L as reference in the HERALDO-Pattern can be described mathematically as:

$$r(x, y) = \delta(y) \left[H\left(x + \frac{L}{2}\right) - H\left(x - \frac{L}{2}\right) \right] \quad , \tag{4.8}$$

with $H(x)$ as the Heaviside function, which is defined as:

$$H(x) = \begin{cases} 0, & \text{if} \quad x < 0 \\ 1, & \text{if} \quad x > 0 \\ \frac{1}{2}, & \text{if} \quad x = 0 \end{cases} \quad . \tag{4.9}$$

The length L must be larger than the diameter of the object in order to fulfill the separation conditions for a HERALDO-Pattern.
Since

$$\frac{\partial}{\partial x} H(x) = \delta(x) \quad , \tag{4.10}$$

the appropriate linear differential operator is found by:

$$\mathscr{L}^{(1)}\{\cdot\} = \frac{\partial}{\partial x}\{\cdot\} \quad . \tag{4.11}$$

This operator applied onto the reference line will result in:

$$\frac{\partial}{\partial x} r(x,y) = \delta(y)\left[\delta\left(x+\frac{L}{2}\right) - \delta\left(x-\frac{L}{2}\right)\right] \quad . \tag{4.12}$$

With equation (4.12) two reference points are obtained in accordance with the separation conditions for a HERALDO-Pattern.

Rotated system

If the derivative is not along the x-axis in the non-rotated system, either $\mathscr{L}^{(1)}\{\cdot\}$ or the coordinate system must be rotated. Here, the latter one has been chosen. In the rotated system the new coordinates $(\tilde{x}, \tilde{y})$ are defined as:

$$\tilde{x} = x\,cos(\alpha) - y\,sin(\alpha) \tag{4.13}$$

$$\tilde{y} = x\,sin(\alpha) + y\,cos(\alpha) \quad . \tag{4.14}$$

The first order linear differential operator for a slit in the rotated system is derived as:

$$\mathscr{L}^{(1)}\{\cdot\} = \frac{\partial}{\partial x}\{\cdot\} = cos(\alpha)\frac{\partial}{\partial \tilde{x}}\{\cdot\} + sin(\alpha)\frac{\partial}{\partial \tilde{y}}\{\cdot\} = \mathbf{e}_\alpha \cdot \nabla_{\tilde{\mathbf{x}}}\{\cdot\} \quad , \tag{4.15}$$

where ∇ is the Nabla-operator and $\mathbf{e}_\alpha$ is the unit vector with the included angle α to the x-axis.

The operator in equation (4.15) will be applied onto the cross-correlation between the object and the slit, which is an operation in real space.
The application of a linear differential operator in real space can be realized via a multiplication in Fourier space. Since the one-dimensional Fourier transform is:

$$F(k) = \int_{-\infty}^{\infty} f(x) e^{-i2\pi kx} dx \quad , \tag{4.16}$$

the derivative $\frac{\partial}{\partial k}F(k)$ will lead to:

$$\begin{aligned}\frac{\partial}{\partial k}F(k) &= \int_{-\infty}^{\infty} f(x)\frac{\partial}{\partial k}e^{-i2\pi kx}dx \\ &= -i2\pi \int_{-\infty}^{\infty} x\, f(x)e^{-i2\pi kx}dx \quad .\end{aligned} \tag{4.17}$$

Here, the angle has not been considered, yet. The importance of equation (4.17) lies in the multiplication of x with $f(x)$ meaning the derivative of $\frac{\partial}{\partial k}F(k)$ can be transformed into a simple multiplication for easier numerical calculation.
Including the angle α and considering a 2D case, the derivative $\mathbf{e}_\alpha \cdot \nabla_\mathbf{k}F(\mathbf{k})$ is:

$$\mathbf{e}_\alpha \cdot \nabla_\mathbf{k}F(\mathbf{k}) = -i2\pi \iint_{-\infty}^{\infty} \Big(x\, cos(\alpha) + y\, sin(\alpha)\Big) f(x,y)e^{-i2\pi(\mathbf{k}\cdot\mathbf{x})}dxdy \quad . \tag{4.18}$$

Equation (4.18) is the formula used for the reconstruction of the experimental data in chapter 6.

The angle α must be determined experimentally in order to use equation (4.18). The determination of the angle can be done either from the diffraction pattern or by Fourier transforming the hologram into real space without multiplication. In the first case it can be exploited that the reference line produces a strong diffraction pattern with the included angle $90° + \alpha$ in regard to the x-axis. In the second case it can be exploited that the autocorrelation of the line also includes the angle α relative to the x-axis.

4.2 Reconstruction in HERALDO

HERALDO with a line as reference will be simulated in this section. The sample is shown in figure 4.3a. The convolution of the object with the line via FTH leads to the hologram shown in figure 4.3b. A 2D FFT results in the conventional reconstruction seen in figure 4.3c. Here, the objects can already be imagined at the ends of the two lines. The line profile through the complex conjugate cross-correlation, seen in figure 4.3e, shows the edges, in which the two objects are encoded. Since the reference line has an included angle $\alpha = 0$ to the x-axis, equation (4.12) will be used for the final reconstruction. Equation (4.12) describes a first derivative

with respect to x of the cross-correlation. After the differentiation with respect to x of the entire conventional reconstruction, figure 4.3d is obtained. As seen in the appropriate line profile, figure 4.3f, and in equation (4.12), the δ-functions at the ends of the line have opposite signs resulting in reconstructed objects with positive and negative intensity, respectively.

For the final reconstruction in section 6.2 it must be kept in mind that the theoretical description of the derivative of the Fourier transformed hologram applies to the case that first the magnitude of the conventional reconstruction is obtained and subsequently the derivative of the Fourier transformed hologram is calculated. In that way the reconstructed objects of the same cross-correlation have different signs in their intensities.

The signs in the intensities of the reconstructed objects will be equal as soon as the differentiation is transferred into a multiplication, as it has been done in the measurement in section 6.2. There, the magnitude of the conventional reconstruction is taken at last, after the multiplication is applied, making all intensities of the reconstructed objects positive.

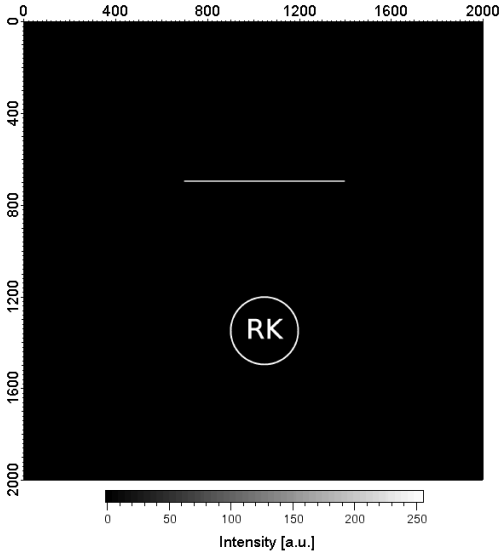

(a) The HERALDO-Sample

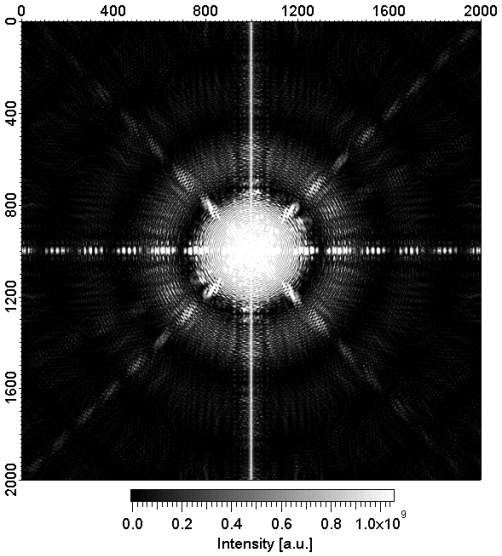

(b) Hologram

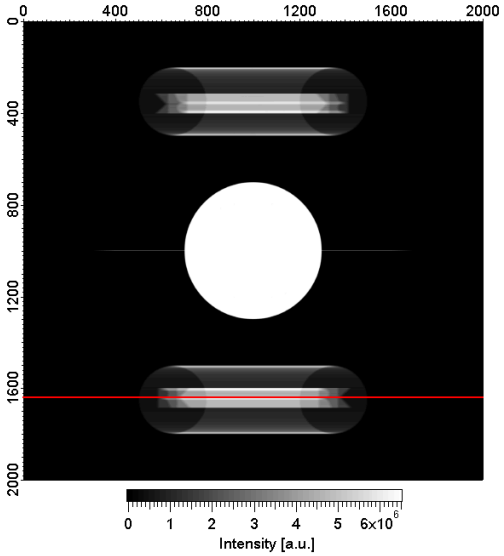

(c) The Fourier transformed hologram

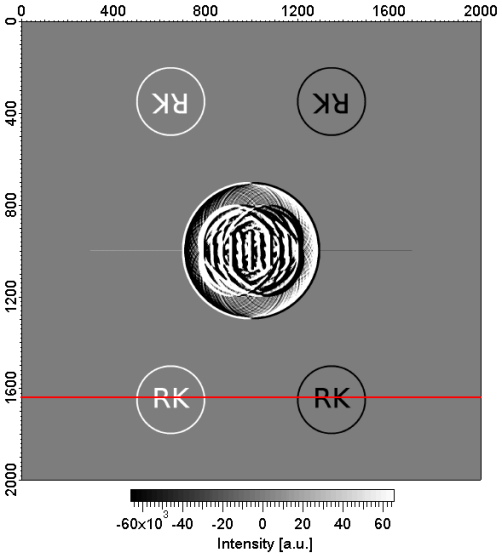

(d) Final reconstruction

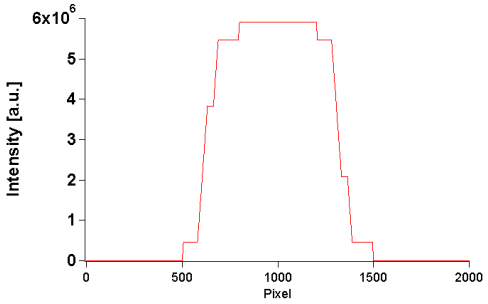

(e) Line profile to c)

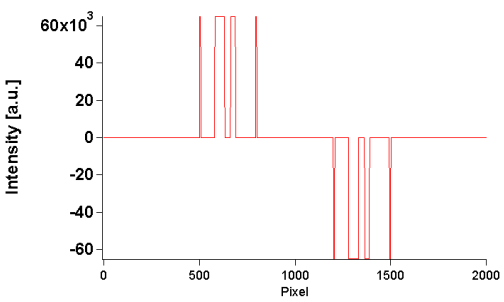

(f) Line profile to d)

Figure 4.3: Reconstruction via HERALDO; The x and y axes denote pixels of the matrix.

4.3 Advantages and disadvantages

Advantages

Intensity of the reconstructed object

In conventional FTH with a point-like reference structure the increase of the signal intensity is the direct consequence of increasing the diameter of the pinhole, which leads to a reduction in the resolution.
In HERALDO the increase of the signal intensity is not directly connected with only one parameter. Here, the signal intensity depends on the line width as well as on the transmission difference between highest transmission and highest absorption at the reference corner. While the increase of the line width reduces the resolution, the increase of the transmission difference between highest transmission and highest absorption at the reference corner raises the signal intensity without losing resolution. This characteristic gives the main advantage over conventional FTH.

Production

Producing small pinholes in multiple reference patterns by a FIB is still a challenge today. An easier way is the production of a line or a rectangle. In the milling process of a pinhole the removed mask material redeposits itself also in the hole. This makes the production of high aspect structures very difficult.
In contrast the area for redeposition is much larger in a line or rectangle providing the possibility to mill the line in such a way that the removed mask material does not deposit itself at the position of the ion bombardment leading to a higher aspect structure.

Disadvantages

Large opening

Considering the same amount of effective reference points the HERALDO-Pattern has a larger open area for soft X-rays compared to reference patterns consisting of only pinholes.
Due to the wide opening in a HERALDO-Pattern the dynamic range of the hologram is mostly determined by the scattered light at low $|q|$-values. Since the

dynamic range of the CCD-camera is limited, the effective dynamic range in order to resolve the interference pattern between object and reference is shorter in the HERALDO-Pattern than in the multiple reference pattern.
Therefore, minimizing the openings in the reference pattern results in a higher resolution to resolve the interference pattern.

Noise and derivation

Noise is always present in measurements. Typically, the noise level in the final reconstruction is set by the signal intensity, the exposure time and the properties of the CCD-camera.
In a measurement with a HERALDO-Pattern as reference, however, the noise level is additionally influenced by the reconstruction method via HERALDO. In the reconstruction via HERALDO the noise is further increased, when the derivative from the noisy Fourier transformed hologram is taken. The increase of the noise level in the final reconstruction is plausible by looking at the derivative itself. The higher the slope between two points the higher is the value of the derivative.
The increase of noise due to the derivative is the main drawback for a HERALDO-Pattern as reference in FTH.

4.4 Rotation

Typically, in soft X-ray FTH in transmission mode the samples are measured orthogonal to the sample surface. In this case the resolution in regard to the reference points in both, the multiple and the extended reference pattern, is defined by the dimensions in the reference pattern and cannot be changed during measurement. In the sample with an URA-Pattern the resolution is defined by the diameter of the pinholes, whereas in the sample with a HERALDO-Pattern the resolution is defined by the transitions between highest transmission and highest absorption along the directions of the derivatives at the corners.

As soon as the possibility is given that the sample can be rotated, the resolution in regard to the reference points is not clearly defined anymore. Rotating the sample will include another parameter, the thickness of the reference pattern. Here, the

rotation is only considered in which the rotation axis lies within the plane of the surface.
In soft X-ray FTH in transmission mode the thickness is very high compared to the typical lengths in the reference patterns. Most often the ratio is 1:10.

In multiple reference patterns, like the URA-Pattern, the high aspect ratio leads to the situation that these samples cannot be rotated by large angles. The pinholes have typically a diameter of 100 nm in a layer with a thickness of 1 μm. After approximately 0.1° every passing photon of the incoming light will interact with one of the side walls in the pinhole. This situation is independent of the orientation of the rotation axis. Therefore, rotating a sample makes only sense, when the aspect ratio between thickness and at least one length in the reference pattern is low.

A HERALDO-Pattern can fulfill this condition. For the description of the rotation with a HERALDO-Pattern only the special case of a single line as reference is considered any further. In the special case of the single reference line, treated as 1D structure, it only makes sense to discuss the rotation further, when the rotation axis is perpendicular to the length of the line.
All reference lines in the HERALDO-Samples for soft X-ray FTH produced so far had a length of 1 μm and larger. In these cases the aspect ratio between layer thickness and line length has always been 1:1 and lower. With a low aspect ratio of 1:1 and lower the sample can be rotated by 45° and more and still provides an opening for the photons.
It will be shown in the following that the rotation of the single reference line leads to two purposes, the increase of the resolution and the contrast in the final reconstruction on the one side and to the feasibility of doing tomography on the other side.

Resolution and contrast

Whereas the increase of the contrast of the reconstructed objects depends only on the rotation angle γ, the increase of the resolution depends in addition on the edge shape.

While the material absorbs according to the Beer-Lambert-Bouguer law: $I(x) = I_0 e^{-\mu x}$, the assumption is made that the thickness of the material is so thin that the light is not entirely absorbed, in order to understand the benefit of the rotation. In this case the basics can be understand, firstly, how the resolution depends on the rotation angle γ and the edge shape and secondly, how the contrast depends on the rotation angle γ.

In figure 4.4 different reference lines are seen. In the first column the line profiles of the single reference lines are illustrated. Each reference line is illuminated from up to down. The resulting reference points, illustrated in the second column, convolved with the object, seen in the third column, result in two reconstructed objects, shown in the fourth column.

At first the reference line will have sharp edges at its ends. In the illustration it can be verified that the resolution is highest, when the reference point is close to a δ-function.
In the first case the edges of the line ends are parallel to the beam of illumination and the sample is illuminated orthogonal to the surface. In this case the transition between highest transmission and highest absorption can be approximated to an infinitesimal short step length leading to a reference point with a shape close to a δ-function.
The resolution decreases the larger the length of the transition between highest transmission and highest absorption. In figure 4.4b an example of a lower resolution is seen.
In figure 4.4c the rotation of the reference line is taken into consideration. In this example the rotation angle γ is set equal to 90°-ϕ with ϕ as the steepness angle of one edge in the reference line. In this case it leads to one optimum rotation angle γ_{opt}=90°-ϕ. Here, the edge parallel to the beam exhibits a resolution close to that of a δ-function, whereas the other side of the line exhibits a decreased resolution after rotation.

Taking rounded edges into consideration leads to broadened reference points, as seen in figure 4.4d.
Rotating a reference line with rounded edges leads to an increase and a decrease in resolution like in the case of sharp edges, too, but a resolution close to a δ-function

cannot be achieved under any angle γ. In figure 4.4e such a situation is illustrated. After rotation the FWHM of one soft edge is smaller, whereas the FWHM of the second edge is wider as it is in the case with γ=0.

Beside decreasing and increasing the resolution the contrast is changed during rotation as well. With increasing the rotation angle γ the projected thickness along the propagation of light raises, too, resulting in an increase of the intensity difference between highest transmission and highest absorption. However, this scenario is independent of the edge shapes at the reference line ends.

Tomography

The second purpose for rotating a HERALDO-Sample is the ability to carry out tomography. Since the object may be a three dimensional structure and is measured in transmission mode, the projection of the absorption or the phase shift inside the object along the propagation of light is represented in the final reconstruction. Rotating the sample will reveal the information of absorption or the phase shift in dependence on the angle γ. Combining all reconstructed objects, recorded at different angles γ's, allows to create a 3D visualization of the object. The visualized 3D image shows the absorption or the phase shift inside the object with the resolution given by the transition length at the corner under the angle γ. However, one drawback of soft X-ray tomography with HERALDO is the dependency on the angle in regard to the resolution. Thus, the resulting 3D image will show the inside of the object with different resolutions depending on the angle of view.

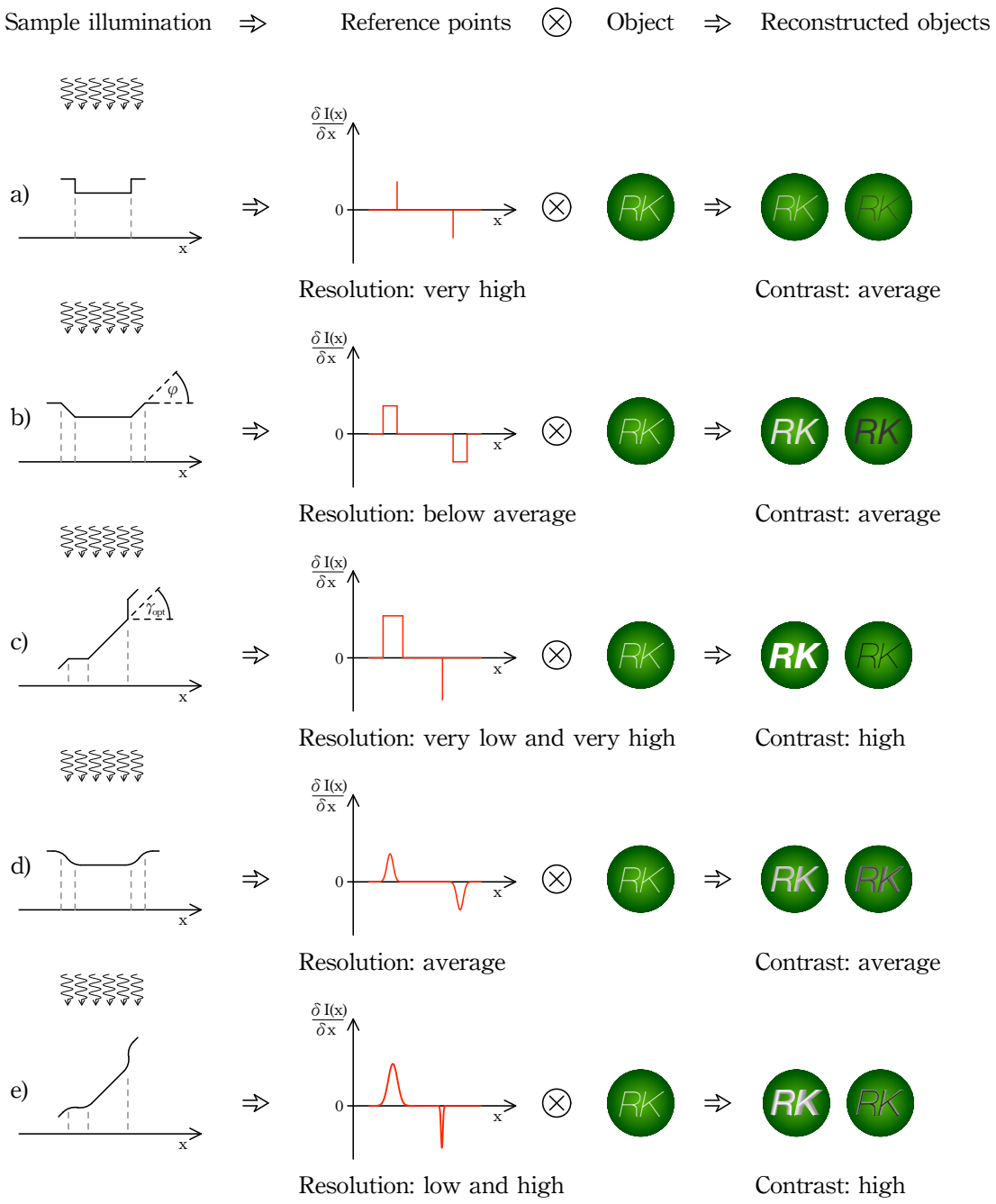

Figure 4.4: Rotation with HERALDO

Chapter 5

Experimental Setup

The experimental conditions for the measurements with the URA-Sample and the HERALDO-Sample are presented in this section. It contains the radiation source, the coherence of the radiation and the support of the sample needed to record an soft X-ray hologram.
Furthermore, the milling process of the holography mask via FIB is discussed.

5.1 Synchrotron source

The experiments with the URA-Sample and the HERALDO-Sample were both carried out at BESSY II. The high brilliance synchrotron facility BESSY II is a third generation light source in the vacuum ultraviolet to soft X-ray range. It stores electrons at an energy of 1.7 GeV and delivers radiation with a brilliance of $3{\cdot}10^{18}$ [photons/sec/(mm mrad)^2/0.1%BW] at about 300 eV.

The URA-Sample and the HERALDO-Sample have been investigated at beamline UE112_PGM-1 and at beamline U41_PGM, respectively.

Beamline UE112_PGM-1

In figure 5.1 the optical layout of the beamline UE112_PGM-1 is illustrated. The beamline UE112_PGM-1 has a plane grating monochromator operating in an energy range from 20 eV up to 600 eV. At the focus position the beam has a size of (80 x 30) μm, when the exit slit is closed to 20 μm. The beam divergence is 1.4 mrad

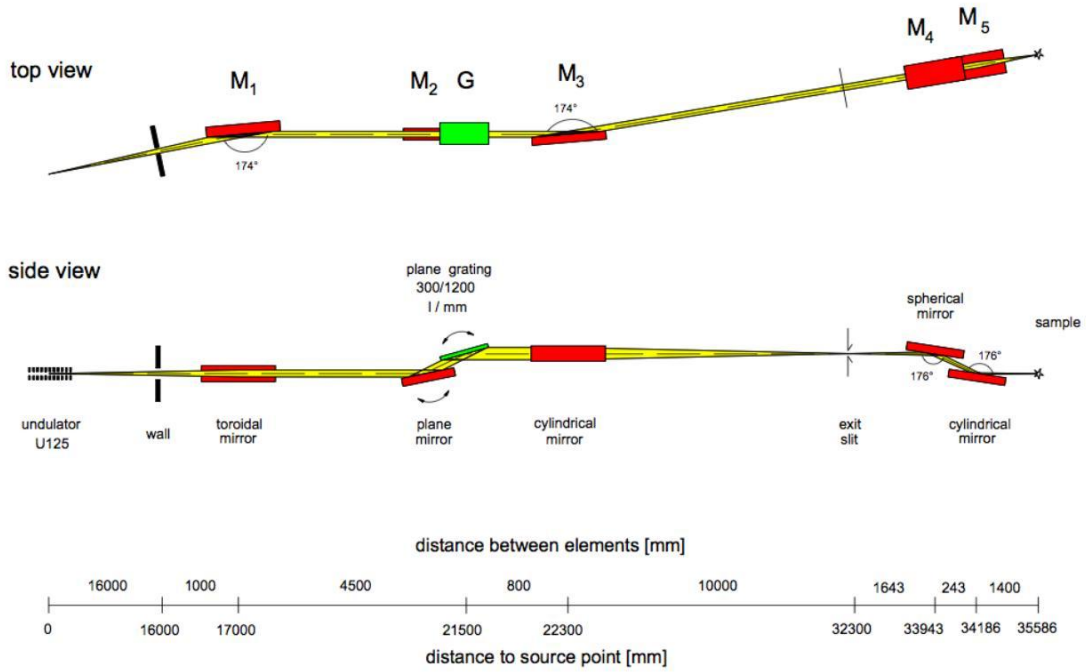

Figure 5.1: Optical layout of the beamline UE112_PGM-1 [83]

horizontally and 0.5 mrad vertically. At an energy of 150 eV and an energy resolution of 30000 [83] the longitudinal coherence length is 124 μm. In order to increase the transverse coherence length, the sample is moved 90 cm downstream behind the focus position, which leads to a transverse coherence length of 47 μm.

Beamline U41_PGM

In figure 5.2 an illustration of the optical layout of the beamline U41_PGM is seen. The energy range of this beamline goes from 170 eV to 1800 eV, which is delivered by a plane grating monochromator. At the focus position the beam has a size of (23 x 12) μm, horizontally and vertically. At this beamline the horizontal divergence is 1.2 mrad and the vertical divergence is 0.5 mrad. At an energy of 800 eV and an energy resolution of 2000 [84] the longitudinal coherence length is 2 μm. Furthermore, the sample was placed around 60 cm downstream behind the focus in order to increase the transverse coherence length to 66 μm.

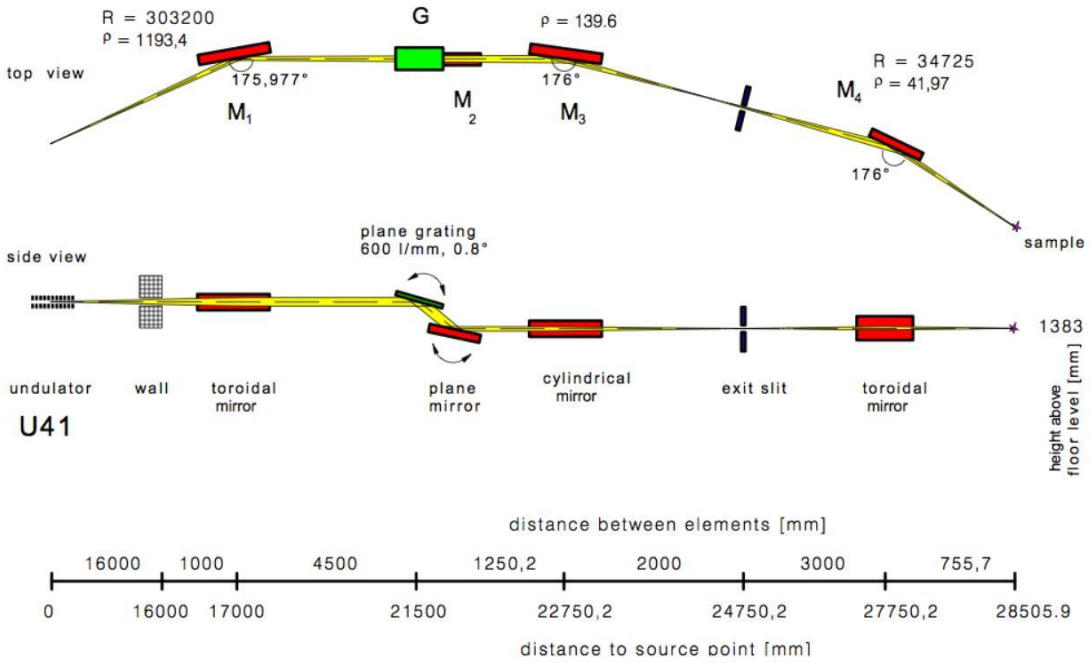

Figure 5.2: Optical layout of the beamline U41_PGM [84]

5.2 Coherence of light

In this thesis the term "light" typically denotes synchrotron radiation in the range of soft X-rays.

FTH is one of the imaging techniques in which the coherence of light is mandatory. Coherence is illustrated in figure 5.3. Two points in the wavefield are called coherently correlated, when the electric field amplitude and the phase of one point can be determined by knowing the electric field amplitude and the phase of the second point at any time. If this is true for any two points at arbitrary positions in the wavefield, then the entire radiation field is said to be coherent.

The wavefields of real sources are neither completely coherent nor fully incoherent. Fully incoherent means that there is no correlation at all at any time. All real sources are partly coherent, meaning within a specific distance the electric field amplitude and the phase of one point can be determined by any other point within this distance.

In figure 5.3 the coherence correlation is divided into the transverse and the longitudinal coherence length. The scheme illustrates both definitions. The transverse

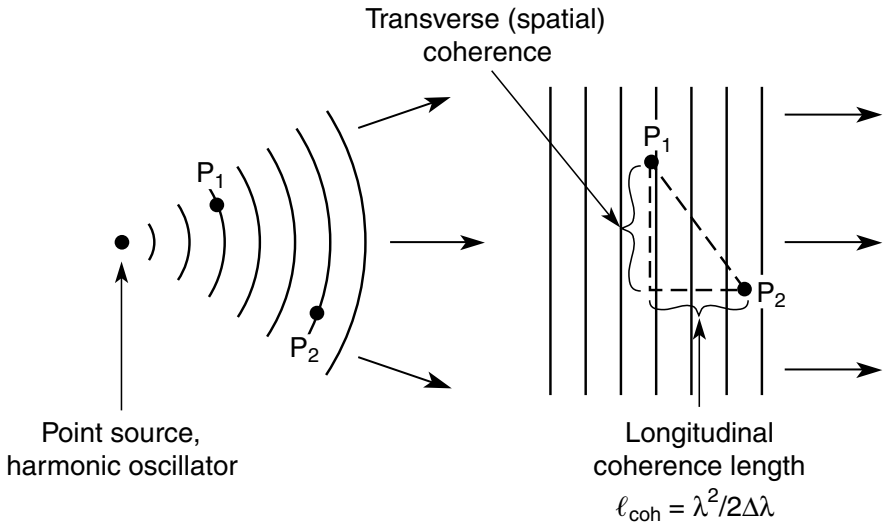

Figure 5.3: Transverse and longitudinal coherence [20]

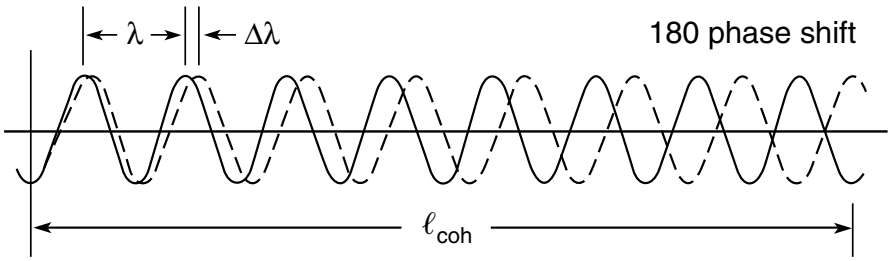

Figure 5.4: Longitudinal coherence length [20]

coherence length is the distance to which two points are coherently correlated orthogonal to the propagation of the light, whereas the longitudinal coherence length is the distance to which two points are correlated along the direction of propagation.

Via the shape of the wavefield the transverse coherence length is related to the finite source size and to the distance between the point of observation and the source. With the Heisenberg uncertainty equation $\Delta x \Delta k \geq \frac{\hbar}{2}$ the relation for the transverse coherence length is obtained:

$$t_{coh} = \frac{z\lambda}{2\pi d} \quad . \tag{5.1}$$

Here, λ is the wavelength in the wavefield, d the size of the source and z the distance between the point of observation and the source.

The longitudinal coherence length is defined over the bandwidth of the emitted radiation as illustrated in figure 5.4. In the scheme a light source is presented emitting radiation of the wavelength λ with a specific bandwidth $\Delta\lambda$, though only the longest and the shortest wavelength of the bandwidth are shown. At the source both wavelengths are in phase meaning two photons at the source are coherent correlated. At a specific distance l_{coh} the two wavelengths are exactly in antiphase. When two photons are considered, one at the source, the other one separated by the distance l_{coh} or larger, it is said that both photons are uncorrelated.
In form of an equation the longitudinal coherence length is:

$$l_{coh} = \frac{\lambda^2}{2\Delta\lambda} \quad . \tag{5.2}$$

This equation is obtained by setting $l_{coh} = N\lambda = (N - \frac{1}{2})(\lambda + \Delta\lambda)$ and transposing it to $N\lambda = l_{coh}$.

Coherent light sources

Coherently correlated photons can be created in different ways, from the emission of a white bulb to the radiation of an undulator. The important parameter of the radiation source is the brilliance, also known as spectral brightness. The better the brilliance of a light source the higher is the available coherent photon flux for an FTH experiment. The brilliance is defined as:

$$\text{brilliance} = \frac{[\text{total number of photons}]}{[\text{time}] \cdot [\text{area}] \cdot [\text{solid angle}] \cdot [\text{energy bandwidth}]} \quad . \tag{5.3}$$

Radiation from sources with low intrinsic coherence can be filtered to select the coherent part of the emitted radiation. In figure 5.5 a white light bulb is shown. The white bulb emitting polychrome light as an extended source (a) can be transformed into a point light source, having a higher transverse coherence length (b), into a monochrome light emitting source, having a higher longitudinal coherence length (c), or into both, a point source emitting monochrome light, having both, a higher transverse and a higher longitudinal coherence length (d).
Although the filtered point light source can be used as radiation source for FTH, the efficiency is very low due to a very low brilliance. Especially for measurements with short exposure times, a high brilliance source is mandatory. Suitable high brilliance sources for soft X-ray FTH are the undulator radiation of the synchrotron

radiation facility BESSY II and the undulator radiation of the Free Electron Laser FLASH.

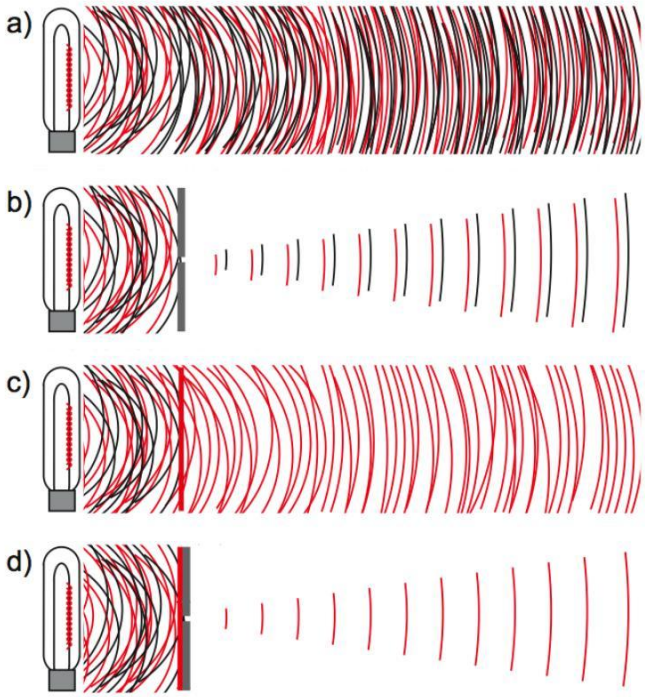

Figure 5.5: Creation of a monochrome point light source [70]; a: extended light source emitting polychrome light; b: point light source emitting polychrome light; c: extended light source emitting monochrome light; d: point light source emitting monochrome light

5.3 Support of the sample

FTH-mask

In this thesis the URA-Sample and the HERALDO-Sample are measured in soft X-ray FTH in transmission mode. Since the soft X-rays are absorbed within less than 1 μm from most materials, some special preparations have to be considered first. Beside being in vacuum the support for the sample has to be very thin in order to avoid a strong decrease in signal intensity.

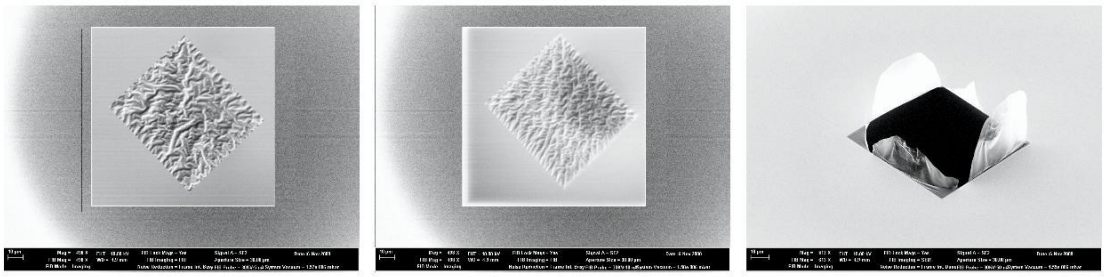

Figure 5.6: An entire Si_3N_4-membrane with a size of 50 μm x 50 μm and a thickness of 50 nm is irradiated by an ion beam of 1 nA until it brakes.

In recent years a suitable support has been found and already been used in several measurements, the Si_3N_4-membrane. Si_3N_4 is strong, when it comes to a freestanding thin membrane. Dimensions of a Si_3N_4-membrane are for instance 100 μm x 100 μm x 50 nm.
It should be noted, nevertheless, that later steps in the production of holography masks can destroy the Si_3N_4-membrane as seen in figure 5.6. In the example of figure 5.6 the entire Si_3N_4-membrane with a thickness of 50 nm was illuminated by a strong ion beam of 1 nA. After 60 s the membrane broke. While substantially lower ion currents of about 2 pA are typically used for the milling procedures of the holography masks, the ion currents must, nevertheless, be considered carefully, when membrane thicknesses of 20 nm and below are used. A wavelike pattern on the membrane is often a first sign for a possible destruction as shown in figure 5.6.

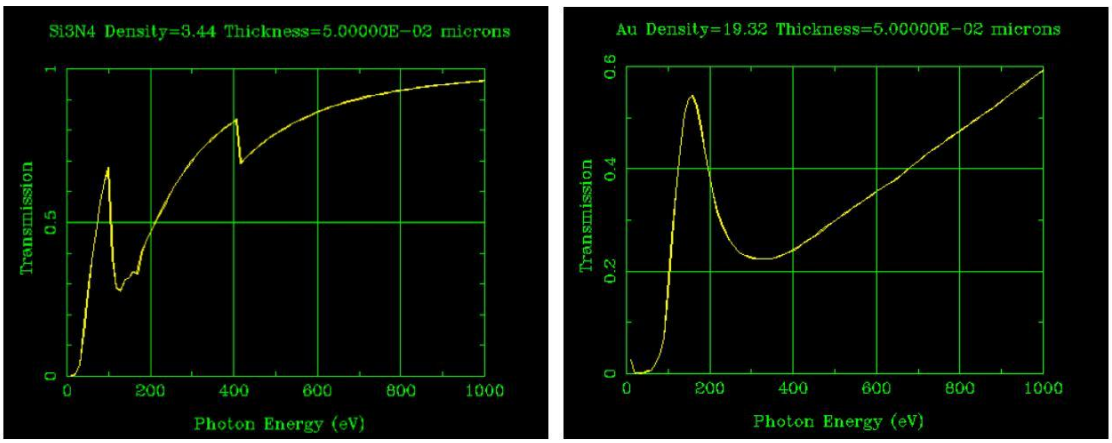

(a) Si_3N_4 (b) Au

Figure 5.7: Transmissions of different materials with a thickness of 50 nm [85]

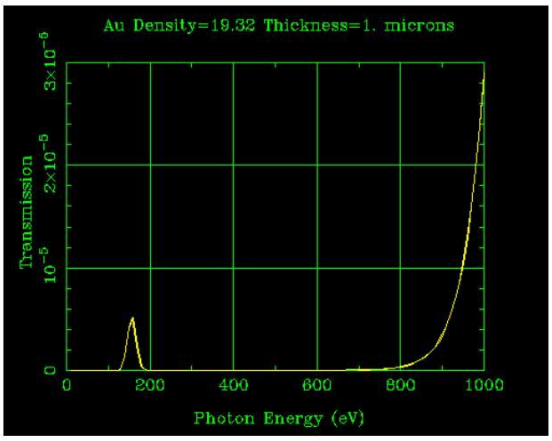

Figure 5.8: Transmission of gold for a thickness of 1 μm [85]

A further strength of Si_3N_4 is the low absorption coefficient for soft X-rays compared to other materials, at least in certain ranges of the soft X-ray spectrum. In figure 5.7 the transmissions between 10 eV and 1000 eV for a thickness of 50 nm are shown for Si_3N_4 and gold, respectively. It can be seen that above 500 eV the transmission is at around 80% and higher for Si_3N_4, whereas for gold the transmission above 500 eV is at around 30% and higher.
The HERALDO-Pattern has been measured at a photon energy of 800 eV. At 800 eV the transmission in Si_3N_4 lies by 93%, whereas in gold the transmission lies by 47%.
Though Si_3N_4 might not be the ideal supporting layer for the energy range below 500 eV, Si_3N_4 has also been used as support for measurements at 150 eV. At 150 eV Si_3N_4 has a lower transmission coefficient as gold, with a transmission of 30% compared to 50% in gold.

The samples in this thesis are only test samples in order to investigate the potential of the URA-Pattern and the HERALDO-Pattern as references in soft X-ray FTH in transmission mode. For this purpose Si_3N_4-membranes are covered with gold, typically with a thickness of 1 μm, in order to avoid unscattered light to be detected by the CCD-camera. The transmission for 1 μm gold is seen in figure 5.8. At 150 eV and a thickness of 1 μm the transmission is $4.3310 \cdot 10^{-6}$, whereas at 800 eV and a thickness of 1 μm the transmission is $0.33338 \cdot 10^{-6}$ times the intensity of the incoming radiation [85].

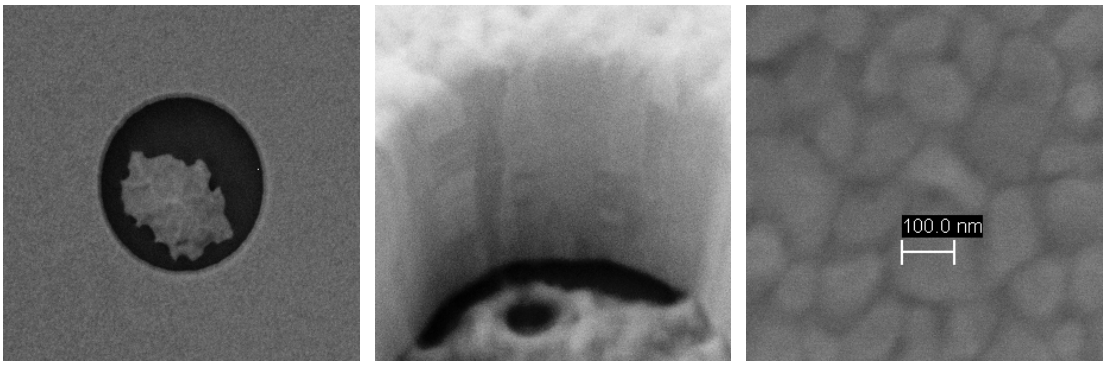

(a) Left overs of gold, after milling an object hole

(b) Crystallisation at the wall of the hole

(c) Gold crystallisation on Si_3N_4-membrane

Figure 5.9: Gold is a good absorber for soft X-rays, but is difficult to handle in the fabrication of object holes and reference holes due to its microcrystalline structure.

The structures are milled into the gold coated Si_3N_4-membrane with a FIB. Both, the object and the reference pattern, are milled entirely through the gold layer and the Si_3N_4-membrane.
Although gold is a good material for a soft X-ray absorber, the microcrystalline structure of gold provides a challenge for the milling of fine reference structures, as the milling yield depends on the relative orientation of the crystal axes to the focused ion beam. In figure 5.9 the effect is illustrated by the presence of "hard grains".

A scheme of a complete mask for soft X-ray FTH is seen in figure 5.10.

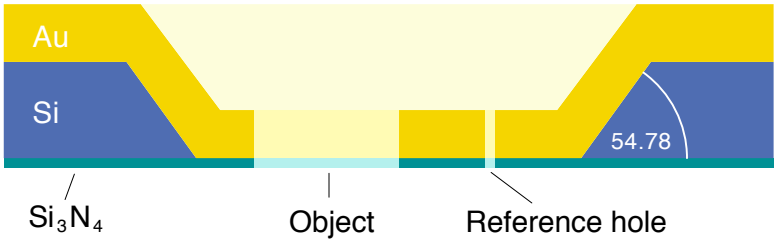

Figure 5.10: Mask for soft X-ray FTH

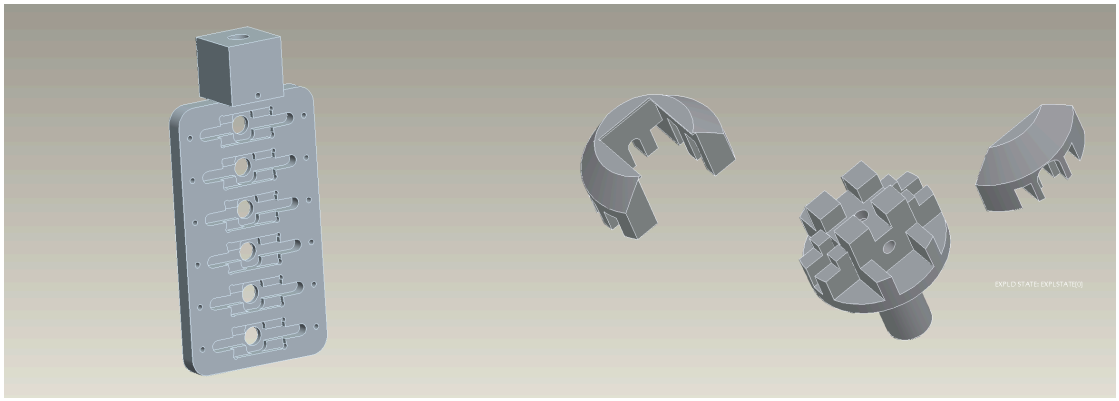

(a) Sample holder (b) FIB-holder

Figure 5.11: Two different membrane holders for measurements with soft X-rays

Membrane holder

Si_3N_4-membranes have been fabricated in two different sizes of silicon wafers. The one kind of a silicon wafer has a size of 10 mm x 5 mm, whereas the other kind has a size of 5 mm x 5 mm.
In order to fix the silicon wafer on the holder, two new holders have been constructed. One sample holder, seen in figure 5.11a, holds six silicon wafers.
In order to produce the samples the Si_3N_4-membranes have to be transferred into a FIB. To minimize the risk of damage, a special sample holder, seen in figure 5.11b, has been constructed, which fits both into the FIB and into the soft X-ray scattering apparatus.

5.4 Nanofabrication by Focused Ion Beam

The Focused Ion Beam (FIB) allows to produce structures in the range of some nanometers to several micrometers. The dual beam FIB used in this thesis consists of two main parts, the electron column and the ion column. The electron column

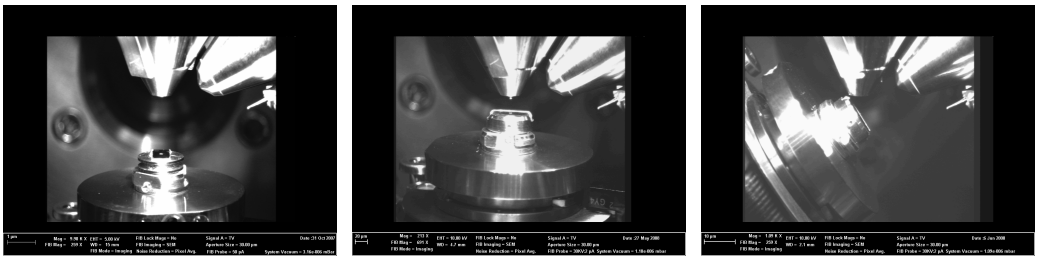

(a) Sample position for imaging with electrons while having a high depth of field

(b) Sample position for imaging with electrons while having a low depth of field

(c) Sample position for milling with ions

Figure 5.12: Different positions of the sample for different imaging modes

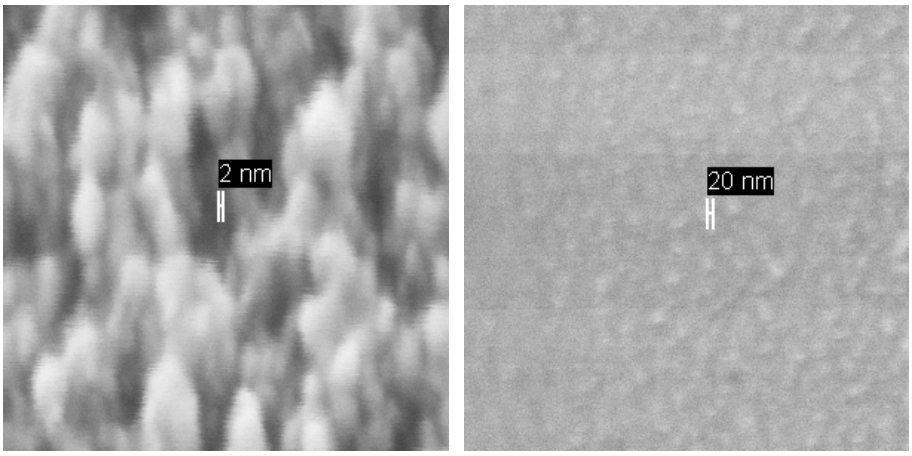

(a) Resolution of the electron column

(b) Resolution of the ion column

Figure 5.13: Resolution of the electron column and of the ion column

is used for imaging, whereas the ion column is used for the milling procedure due to the typically $\approx 1.3 \cdot 10^5$ higher mass of the ions compared to the electrons. The ions with their high momentum, gained through the acceleration by a high voltage, remove surface atoms leaving a crater in the material of production.

The unit for electrons as a stand alone machine is known as Scanning Electron Microscope (SEM). This unit consists of an electron gun, an electric field as accelerator and electromagnetic lenses to influence the shape of the electron beam and to focus the electrons on the sample. In figure 5.12a and figure 5.12b two pictures are shown how the sample will be placed in regard to the electron column. The distance between the sample and the end of the electron gun, which is called "Käppchen", can vary. The larger the distance between the "Käppchen" and the

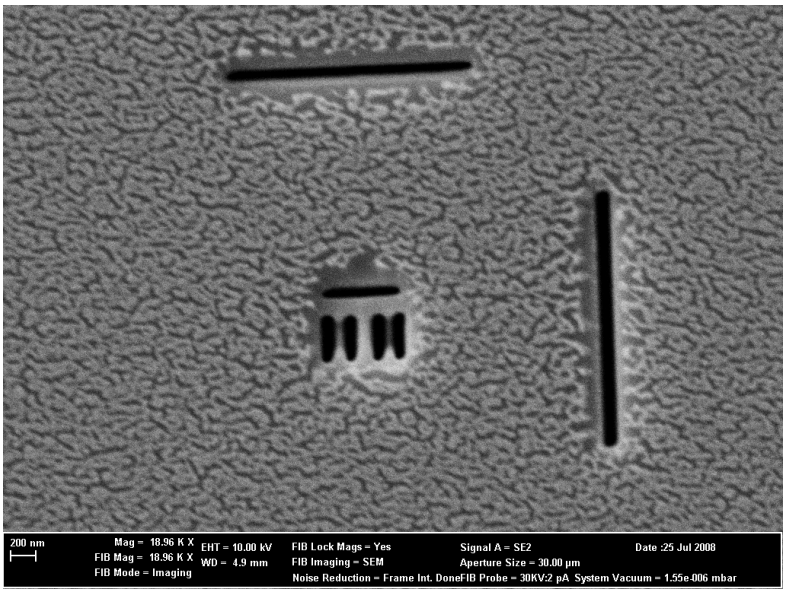

Figure 5.14: HERALDO-Pattern

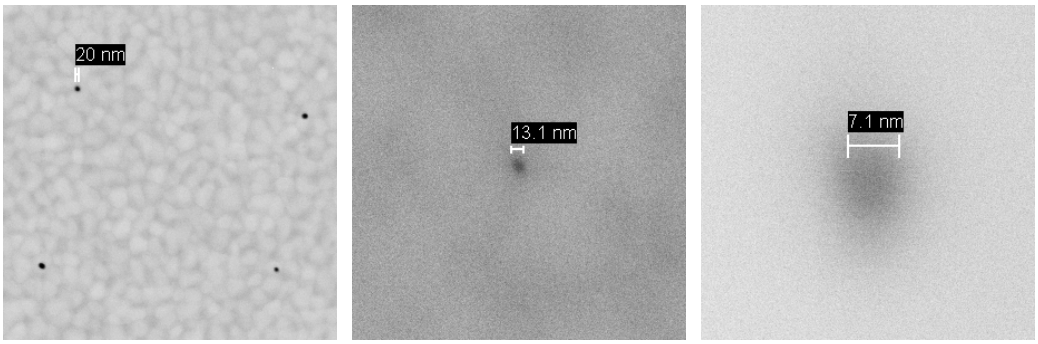

(a) 20 nm (b) 13.1 nm (c) 7.1 nm

Figure 5.15: Smallest achieved diameters for high resolution FTH

sample, the larger will be the depth of field.
In order to work with the electron column and the ion column at the same time the sample is very close to the "Käppchen" as seen in figure 5.12b and figure 5.12c.

In the electron column the electrons are accelerated by a maximum voltage of 10 kV. With this acceleration a resolution of 2 nm can be obtained, which is seen in the electron raster image 5.13a.

The ion column is similar to the electron column, but has to take into account the opposite charge and the larger mass of the ions accelerated here. It also consists

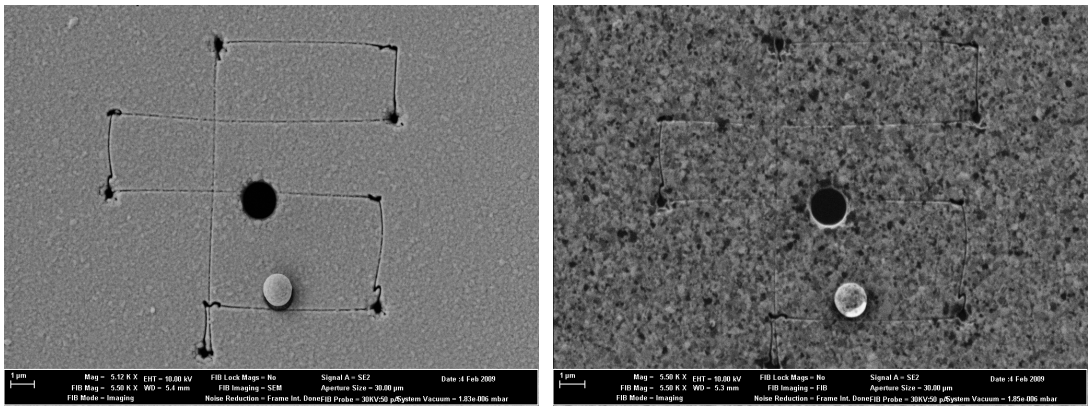

(a) Electrons (b) Ions

Figure 5.16: Different contrasts with electrons and ions

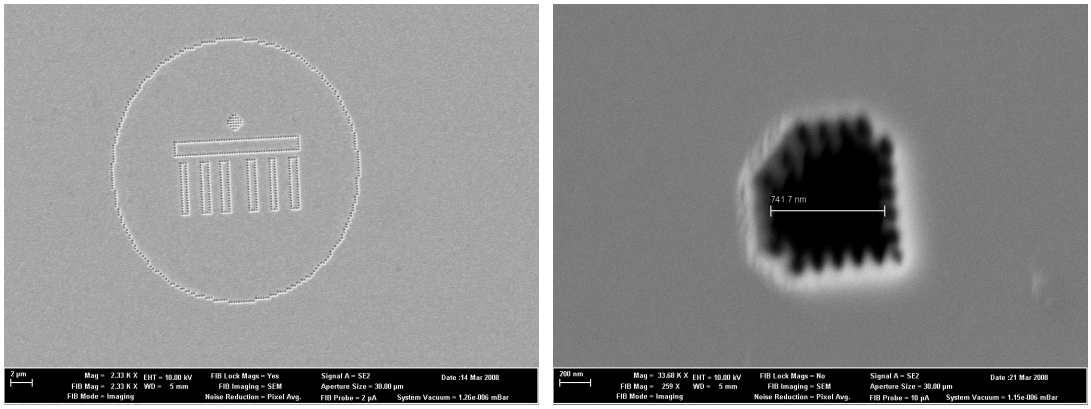

(a) Milling procedure with Cartesian coordinates (b) Hole

Figure 5.17: The milling procedure sets the ion beam according to Cartesian coordinates complicating the fabrication of smooth round holes.

of a gun, an accelerator unit and electromagnetic lenses to influence the shape of the ion beam and to focus the ions on the sample. The emitted ions are gallium ions and are accelerated by 30 kV. The number of accelerated gallium ions, the ion current, depends on the process the user wants to do. In the case of fabricating a mask for FTH, an ion current between 1 pA and 10 pA is used.

In figure 5.14 a HERALDO-Pattern, produced by the described FIB, is seen. It consists of an object and two reference lines. The achieved sizes of reference holes in multiple reference patterns had an average size of 40 nm. In figure 5.15 the smallest diameters achieved for a reference hole are seen.

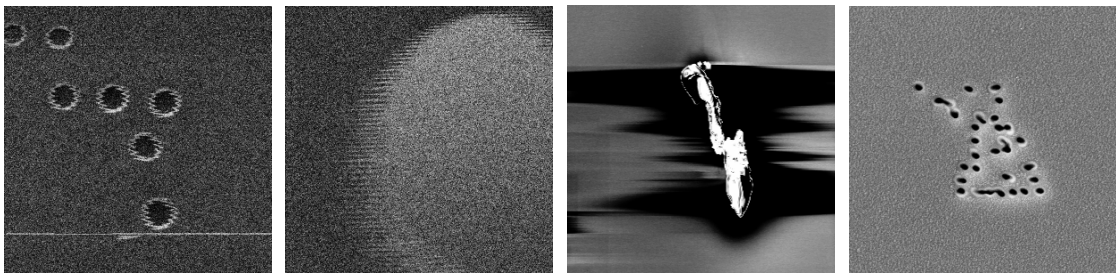

(a) 50 Hz noise (b) Higher noise frequency (c) Charge effects (d) Software problems

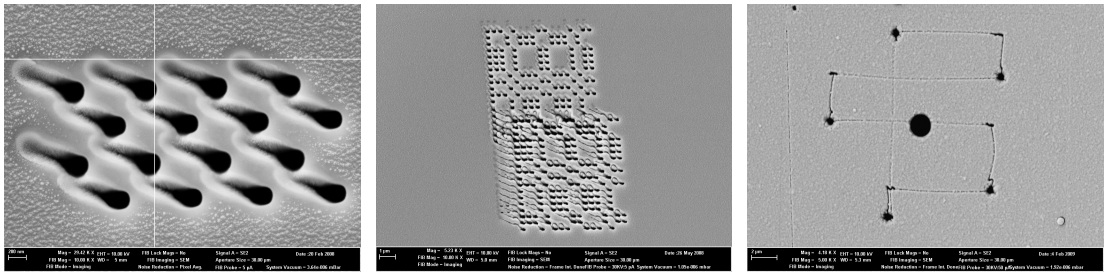

(e) Drift (f) Jumps (g) Hardware problems

Figure 5.18: Different kinds of FIB-production artifacts

If the sample is stable enough to survive the ion bombardments, the ion column can be used as imaging tool as well. In figure 5.13b a resolution of 20 nm is demonstrated. However, images taken with the ion column are not typically used in combination with a gold layer as the gold is significantly milled away during image acquisition. The images of the ion column shown here have been done at a time when the ion source was close to being empty. In this case the gold stayed long enough to be viewed.
In the relatively fortunate case of imaging with ions the sample can be imaged by the electron and the ion column showing different contrasts in the sample. An example is shown in figure 5.16. In figure 5.16a the sample is imaged by electrons, whereas in figure 5.16b, the sample is imaged by ions.

Though several samples have been fabricated with this particular FIB, some disorders were encountered, making the milling procedure difficult. Particular difficulties for structuring in the nanometer range, seen in figure 5.17 and in figure 5.18, were:

- variations in the nominal versus real ion current
- no support for circular shapes in the patterning software
- drift of the sample relative to the ion beam
- intermittent oscillatory noise on the pattern beam
- sudden jumps of the sample stage

The drift could partially be corrected by a drift correction, which uses image recognition on a reference structure.

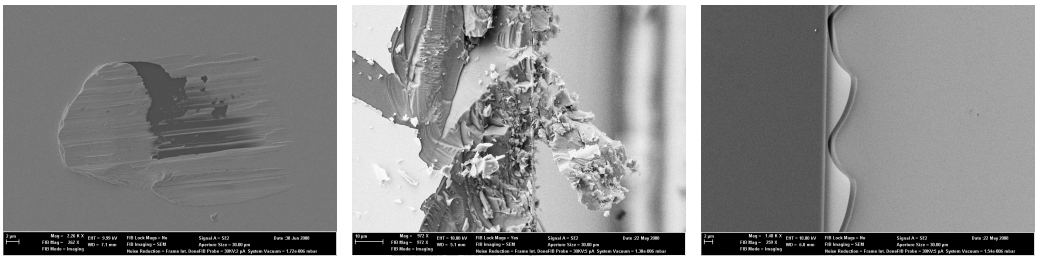

(a) Scratch (b) Parts broke off (c) Si_3N_4-membrane torn off

Figure 5.19: Three examples of damaging the wafer with a tweezers

In addition to the disorders some handling difficulties have been encountered as well. In figure 5.19a and in figure 5.19b two examples are shown, in which the surface of the wafer is scratched due to the use of tweezers. With a wafer size of 5 mm x 5 mm it might happen that the Si_3N_4-membrane will tear away from the silicon wafer. If the Si_3N_4-membrane is already sputtered with gold, the tearing off does not necessarily lead to a broken Si_3N_4-membrane as seen in figure 5.19c.

Production of the sample "RK26"

With this FIB the sample "RK26", shown in figure 5.20, is produced. The figure shows the test object at the bottom of the picture, the Reference URA-Pattern in the upper part and two additional reference pinholes at the right side of the picture. The four holes close together at the left side of the picture are markers for the drift correction. It turned out that the four point layout is most suitable

for a drift correction with a high repetition rate, like in the case of this sample. The structures of the sample have been produced separately.
The Reference URA-Pattern with its 162 pinholes is milled with an ion current of 2 pA, with 10 s per pinhole split in 100 repeats. The drift correction has been applied 172 times every 42 s.
The two additional pinholes are milled with an ion current of 2 pA as well, but with a milling time of 120 s for the lower pinhole and 240 s for the upper pinhole, without drift correction.
The object is milled with an ion current of 2 pA. The total milling time for the cross has been set to 200 s, whereas the four adjacent pinholes had a total milling time of 120 s each. Both structures are milled with 100 repeats and without drift correction.

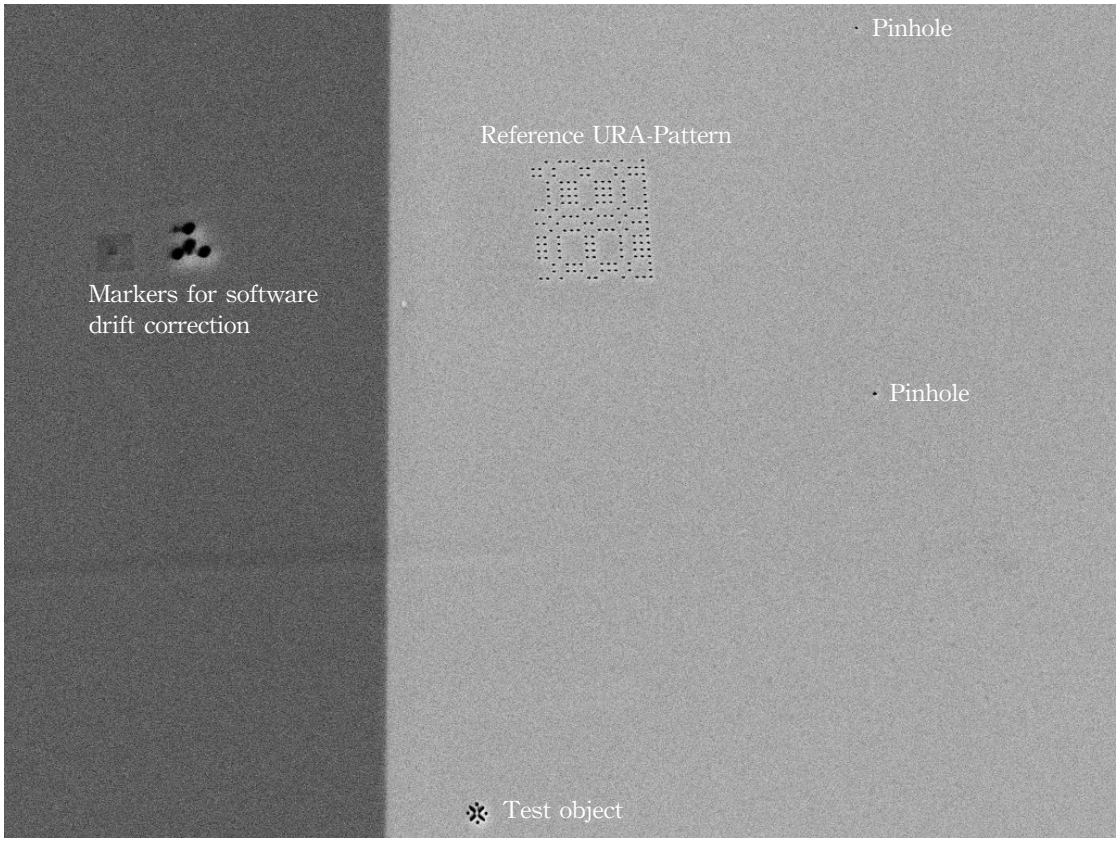

Figure 5.20: Sample "RK26"

Chapter 6

Results and Discussion

The considerations in chapter 3 and chapter 4 are the basis of the experiments described in this chapter. The measurement of the URA-Sample using its new way of hologram reconstruction and the measurement of the HERALDO-Sample are proof-of-principle experiments for soft X-ray FTH in transmission mode.

6.1 URA in soft X-ray FTH

Soft X-ray imaging with an URA-Pattern as reference in FTH has been recently reported in reference [62]. In this publication the authors used a self-supporting URA-Pattern to extract the reconstructed object from the experimental data by using a deconvolution method in combination with a phase retrieval algorithm [89]. In the following experiment the sample with an URA-Pattern as reference is measured in soft X-ray FTH in transmission mode and is reconstructed according to the convolution method described in section 3.3.1 without the need for a phase retrieval algorithm.

Sample "RK26"

The sample "RK26" is measured at beamline UE112_PGM-1 with an energy of 150 eV, which is equivalent to the wavelength of 8.3 nm. The sample is placed 900 mm behind the beamline focus position leading to a transverse coherence length of 47 μm. Further downstream at 217 mm behind the sample the CCD-camera is placed. At this distance the diffraction limited resolution is calculated

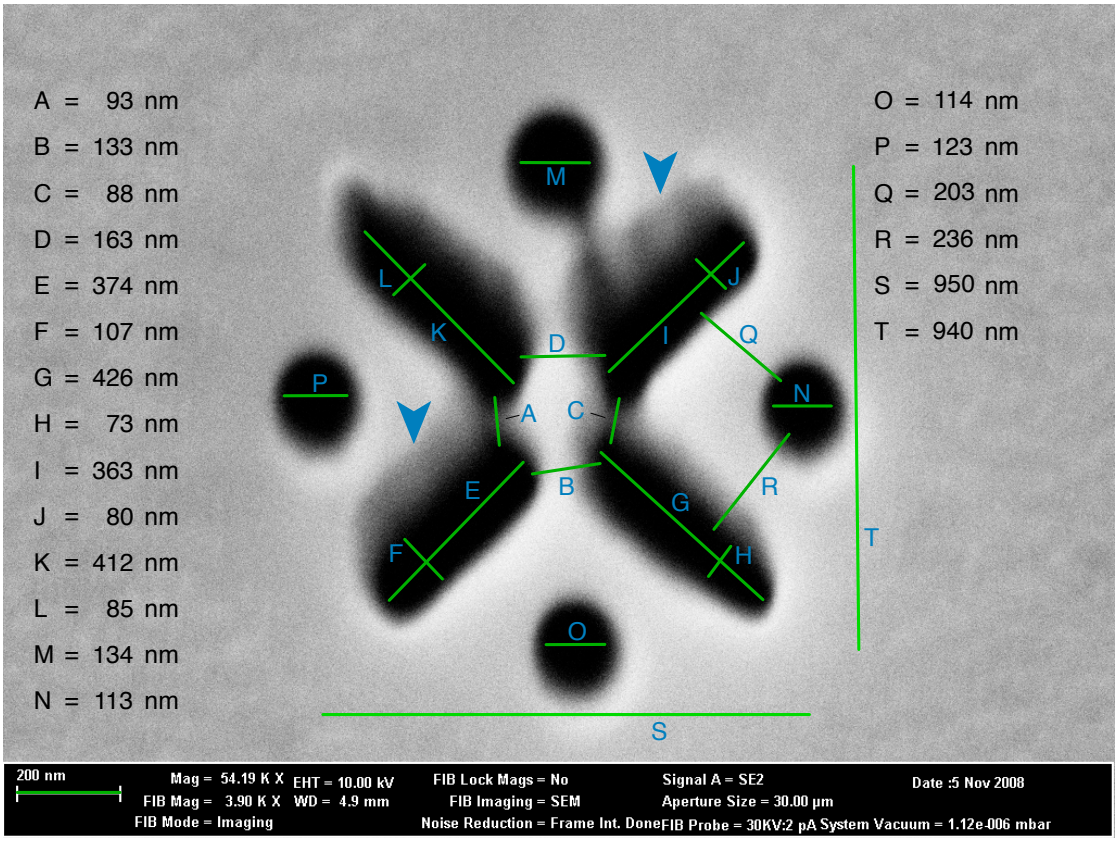

Figure 6.1: SEM-picture of the object in "RK26" with length markers; point of view: orthogonal to the surface; grey areas: edges with flat slopes; arrows: terraces arisen due to milling disorders, visible in the reconstructed object in figure 6.9b

to $d_{min_s} = 130\,\text{nm}$ and $d_{max} = 66\,\mu\text{m}$, according to section 2.3.1. d_{min_s} is calculated for the shortest distance between center and border of the CCD-chip. Since the CCD-chip is squared, the corners of the CCD-chip detect $|q|$-values belonging to distances down to $d_{min_l} = 92\,\text{nm}$. However, it should be kept in mind that only the distance d_{min_s} can be resolved in all directions.

The object, which will be investigated in this experiment, is seen in figure 6.1. Since the thickness of the layer, in which the structure is milled into, is over $1\,\mu\text{m}$, the distances marked in the SEM-picture show the smallest and largest possible distinguishable lengths in the different milled parts, respectively. Though the different lengths will be a lot smaller and larger on the other side of the layer, respectively, it must be kept in mind that the absorption in the measurement is lower, the deeper the structure is milled.

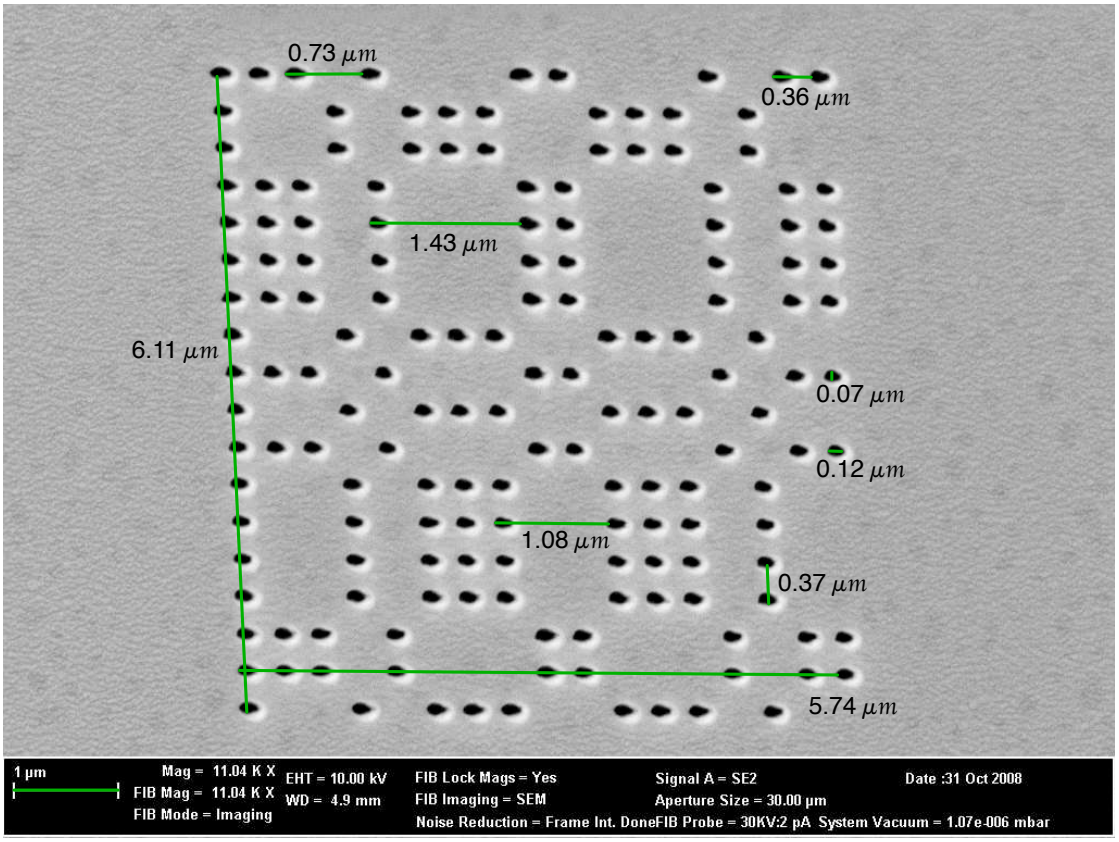

Figure 6.2: SEM-picture of the Reference URA-Pattern in "RK26"

Note that figure 6.1 shows a top view of the sample. Several side walls of the aperture have a significant slope such as the regions marked by arrows. As will be seen later, this effect is visible in the soft X-ray transmission images of the sample.

The object of figure 6.1 is convolved with a Reference URA-Pattern, which is seen in figure 6.2. The Reference URA-Pattern is assembled of only one Basic URA-Pattern, which consists of 17 x 19 URA-Elements and is created according to section 3.1.
The Reference URA-Pattern is larger than the object, which is, according to section 3.3, a precondition for the successful reconstruction via the convolution method. It will be seen that the size ratio of 1:6 between the Reference URA-Pattern and the object is found again in the final reconstruction.
Another precondition for the Reference URA-Pattern is the production of its holes. According to section 3.3.4, the transparent URA-Elements must be identical in or-

der to avoid artifacts. Looking at the size of the holes in figure 6.2, over 90% look very similar to each other. The holes within the transparent URA-Elements are well positioned, too, when the shear geometry is considered in the borders of the URA-Elements. In this case the borders have not a rectangle, but a rhombus shape. It will be shown in the convolution method that this shear geometry cannot be taken into account in the reconstruction procedure. Most probably this is the main reason for the poor performance of the convolution method with respect to increasing the signal to noise ratio of the reconstructed object, while sustaining the high resolution of conventional FTH.
Under ideal conditions, avoiding the shear geometry and improving the diffraction limited resolution, the achievable resolution due to the diameter of the pinholes should be 70 nm along the y-axis and 120 nm along the x-axis, as seen in figure 6.2. In addition to the improved resolution, the reference beam intensity would be 162 times higher compared to conventional FTH due to the 162 pinholes in the Reference URA-Pattern.

In figure 6.3 the entire sample is shown. The SEM-picture shows the Si_3N_4-side. The large bright area and the large dark area in the SEM-picture show the location of gold and silicon, respectively, directly behind the Si_3N_4-layer. As a reminder, the material structure is seen in figure 5.10. Since the Si_3N_4-layer is only 100 nm thin, the primary electrons of the electron gun in the SEM penetrate through the Si_3N_4-layer and create secondary electrons, which penetrate back through the Si_3N_4-layer to the secondary electron detector used to generate the image. More secondary electrons are created in the gold than in the silicon, therefore, the gold appears brighter than the silicon.
The distance between the object and the Reference URA-Pattern is very large ensuring that the separation conditions of section 2.2 are followed.
The two additional pinholes, seen in figure 6.3, are not necessarily needed for the convolution method. However, this special feature in the sample allows the comparison between the convolution method, the deconvolution method and the conventional method, which will be considered later in this section.

The hologram of the sample is seen in figure 6.4. The center of the hologram is

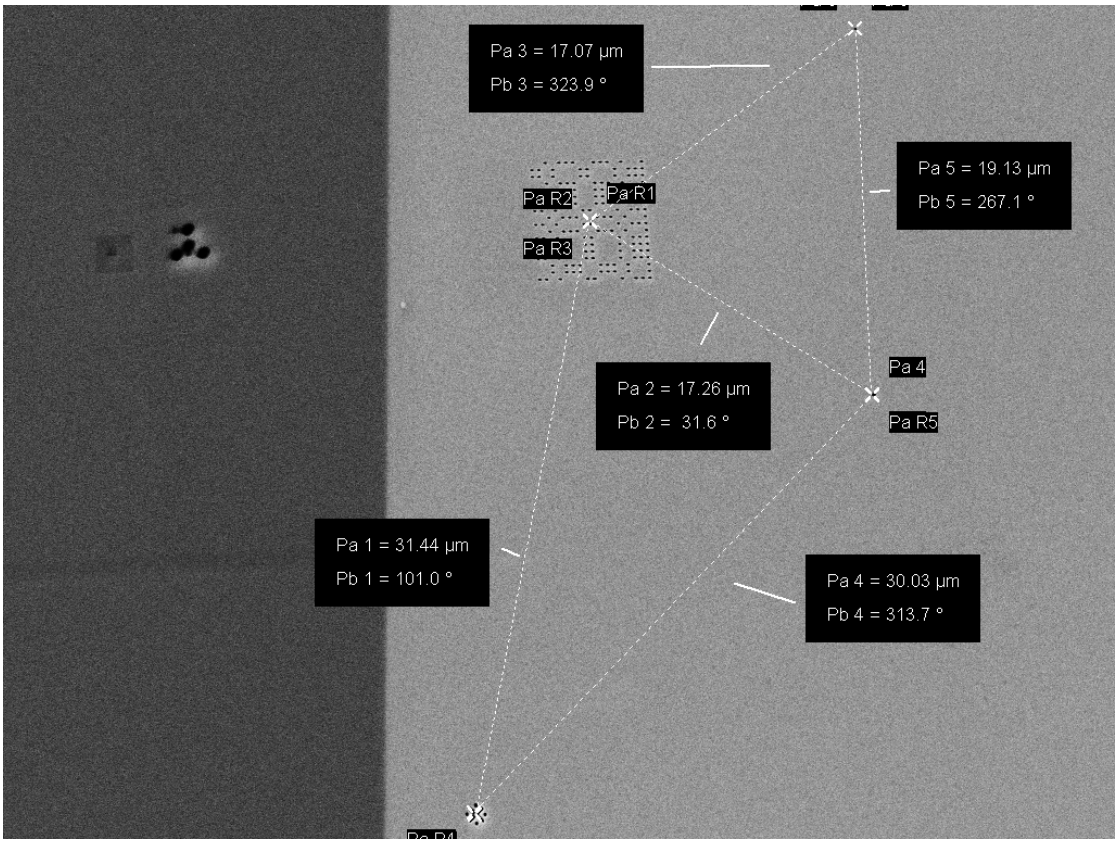

Figure 6.3: SEM-picture of the sample "RK26"; This picture is taken from the Si_2N_4-side of the wafer. The entire field of view is covered with Si_2N_4. The contrast between gold (bright on the right) and silicon (dark on the left) is seen through the thin Si_2N_4-layer on top.

well positioned in the middle of the CCD-chip leading to the ability to resolve d_{min_s} equally in all directions.

Due to the strong illumination, unscattered light passes through the sample and reduces the exposure time and, therefore, the effective dynamic range for the detection of the hologram. A beamstop, made out of a high vacuum compatible epoxy bead on a 150 μm tungsten wire, blocks the unscattered light. Unfortunately, the beamstop blocks also scattered light with low $|q|$-values. Since the beamstop is positioned acentric in regard to the center of the hologram, different ranges of $|q|$-values are covered. Due to the shape and position of the beamstop, lengths of 5 μm and larger in all directions in the sample are reconstructed with a reduced quality in the final reconstruction. In addition, since the beamstop is elongated and acentric positioned along the x-axis, lengths in the same direction

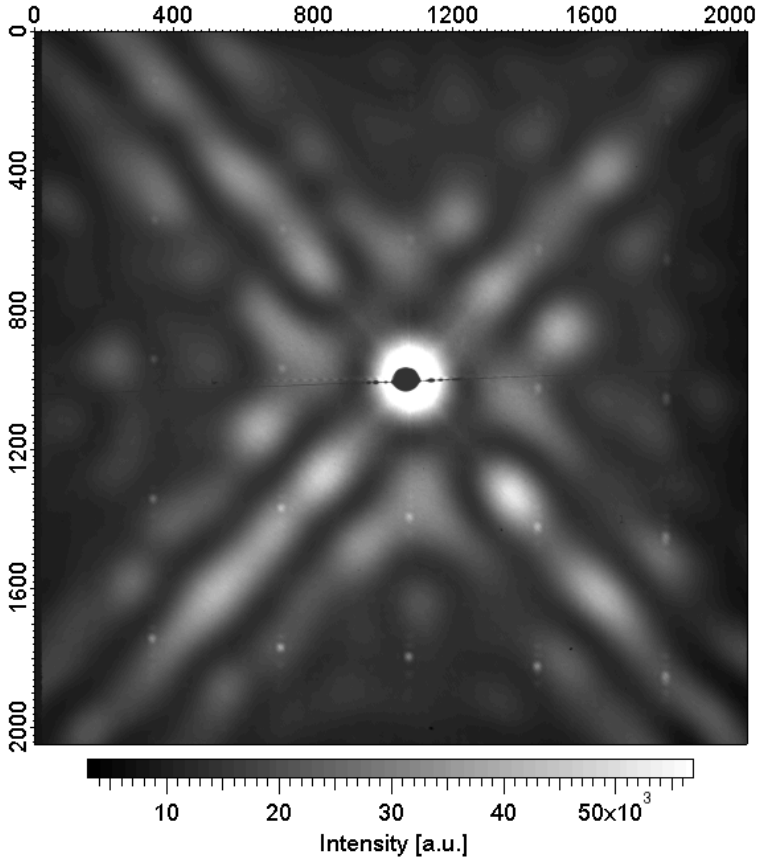

(a) Entire hologram

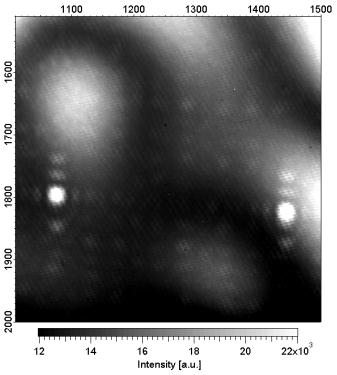

(b) Cutout

Figure 6.4: Hologram of "RK26"; The x and y axes denote pixels. 1 pixel is equal to $0.03\,\mathrm{nm}^{-1}$.

with a size of $2.5\,\mu$m and above cannot be properly reconstructed. However, the longest distance in the object is smaller than $1\,\mu$m, meaning the beamstop does not influence the quality of the final reconstruction.

A slight influence on the quality of the final reconstruction is exerted by the Bragg-Peaks, created by the Reference URA-Pattern. In several $|q|$-regions the Bragg-Peaks are more intense than the diffraction pattern of the object. The remaining diffraction pattern of the Reference URA-Pattern, apart from the Bragg-Peaks, is almost not visible in the entire view and only slightly visible in the cutout.

Though the Bragg-Peaks are more intense than the diffraction pattern of the object, they are not the most intense areas in the hologram and thus not limiting the CCD exposure time. The area with low $|q|$-values is the most intense area and restricts the exposure time to 240 s. In order to reduce the noise level relatively to

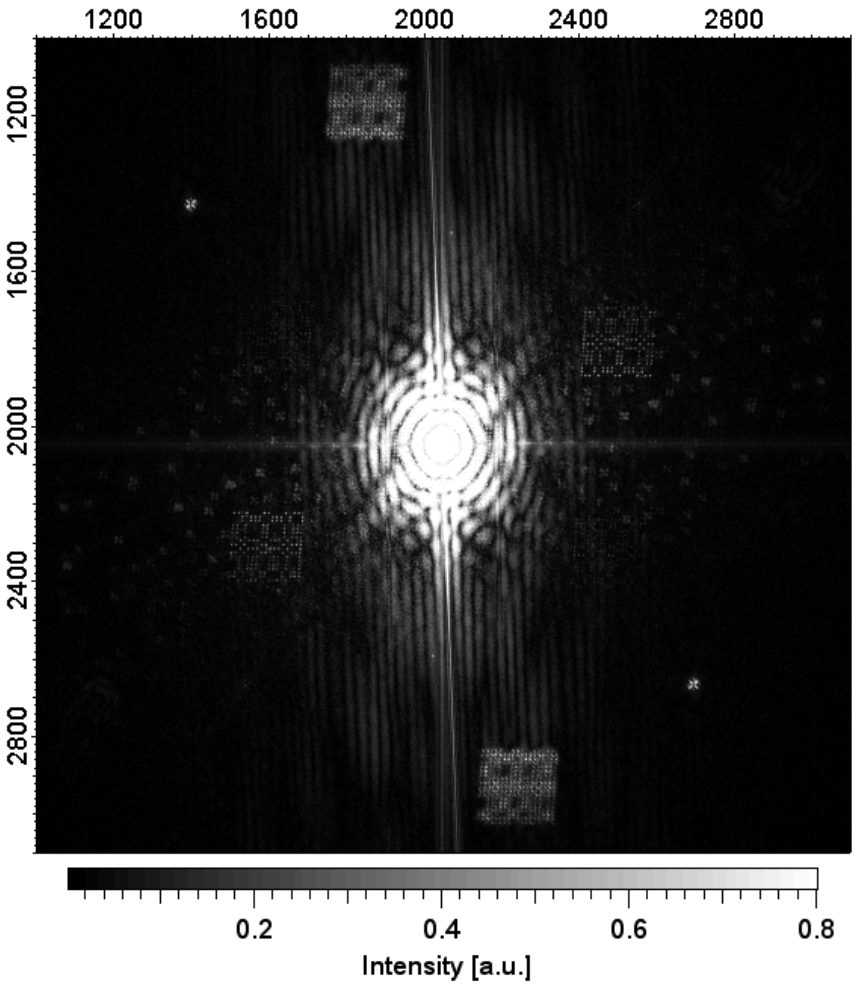

Figure 6.5: Entire view of the Fourier transformed hologram; The x and y axes denote pixels. 1 pixel is equal to 32 nm.

the signal intensity the measurement is accumulated 10 times leading to a summed exposure time of 2400 s.

The Fourier transform of the hologram is seen in figure 6.5. In the hologram different cross-correlations are visible. It is visible as well that artifacts from the center spread out and partly reach the cross-correlations. However, the influence of these artifacts is not significant. These artifacts in the background of the cross-correlations are removed by a rolling ball background subtraction function with 6 pixels as diameter, available in the program "ImageJ".

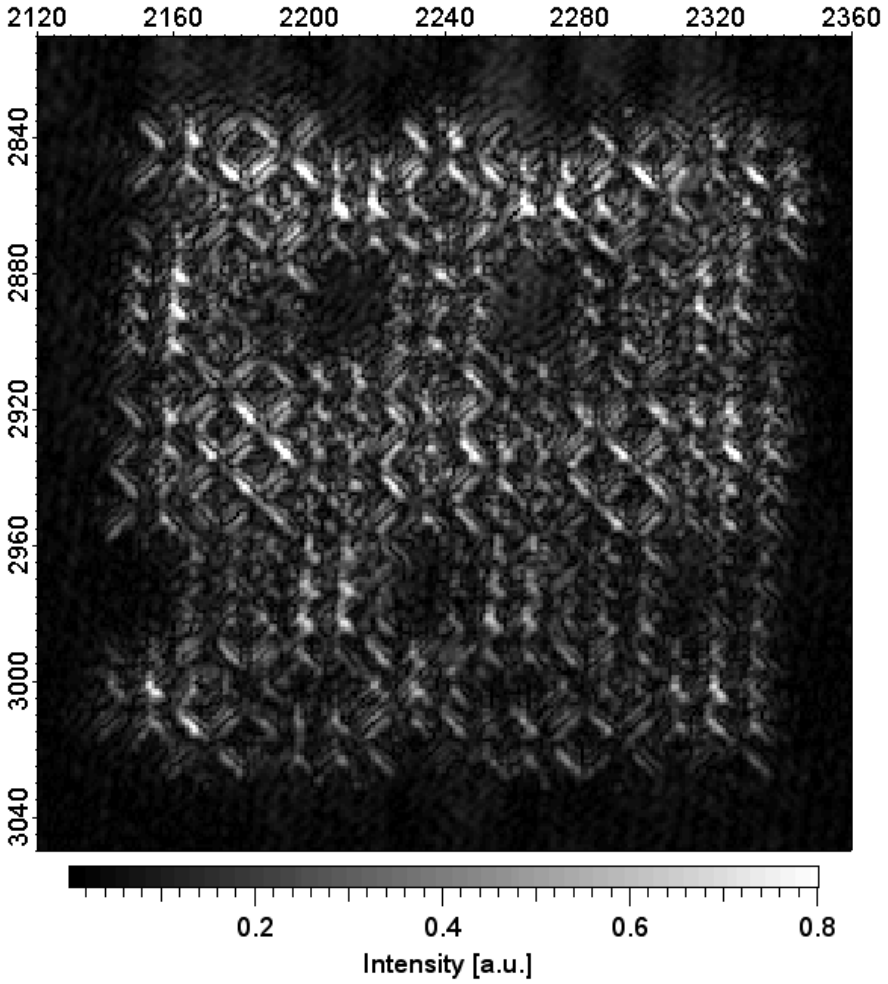

Figure 6.6: Cross-correlation between object and Reference URA-Pattern; The x and y axes denote pixels. 1 pixel is equal to 32 nm.

For the convolution method only the cross-correlation between the object and the Reference URA-Pattern is considered, which is seen in figure 6.6. This cross-correlation is convolved with the Reconstruction URA-Pattern, seen in figure 6.7. The Reconstruction URA-Pattern has an URA-Element size of 11 x 11 pixels. For now, the size of the URA-Elements is a free parameter due to experimental uncertainties. It will be seen later that the special design of the sample allows the direct determination of the URA-Element size in the Reference URA-Pattern and, therefore, according to section 3.3, the size of the URA-Elements in the Reconstruction URA-Pattern.

Furthermore, the Reconstruction URA-Pattern is mosaiced of 3 x 3 Basic URA-

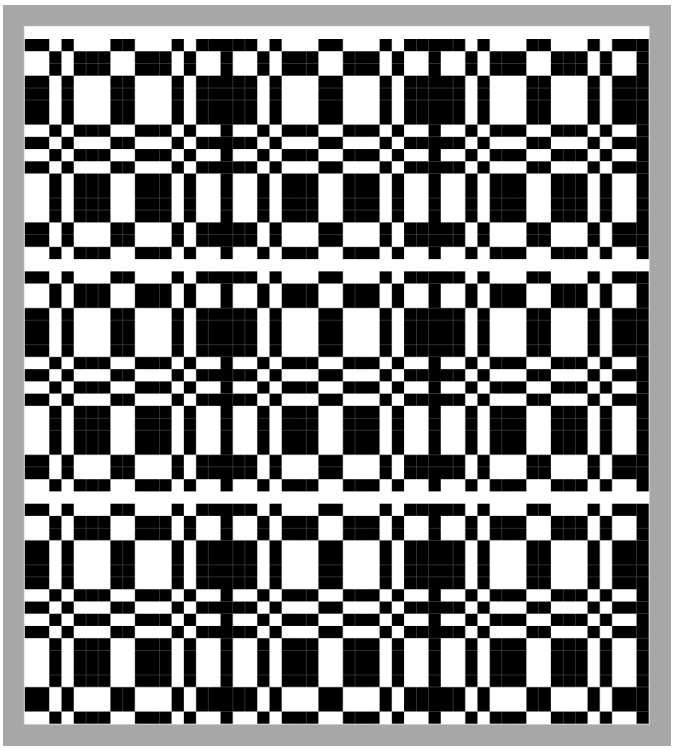

Figure 6.7: The Reconstruction URA-Pattern for the convolution method in order to reconstruct the object of "RK26"; The matrix consists of 561 x 627 pixels.

Patterns, which are generated the same way as the Basic URA-Pattern of the Reference URA-Pattern. Therefore, the Reconstruction URA-Pattern consists of 51 x 57 URA-Elements leading to a total size of 561 x 627 pixels. The total size of the Reconstruction URA-Pattern defines the size of the empty matrix, in which the cross-correlation between object and the Reference URA-Pattern is embedded, which has, therefore, a size of 561 x 627 pixels as well.
The most important parameter in the Reconstruction URA-Pattern is, however, the RSH value. According to section 3.3.1 the quality of the final reconstruction is only perfect, when RSH=0 in the Reconstruction URA-Pattern, which is the case here.

According to section 3.3 the 3 x 3 Basic URA-Patterns create nine reconstructed objects. In the final reconstruction of the convolution method, presented in figure 6.8, the nine reconstructed objects are seen, though five reconstructed objects are split by the border. The four properly reconstructed objects in the middle of the picture show the principal success of the reconstruction method via convolution. It

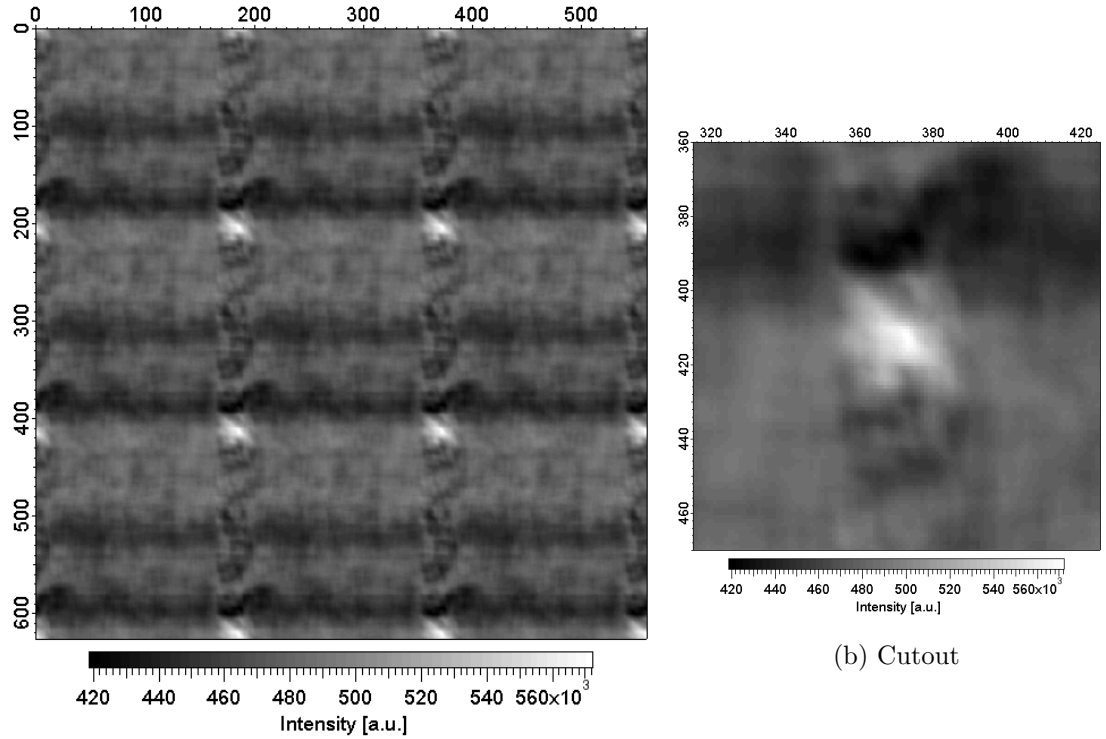

(a) Entire reconstruction

(b) Cutout

Figure 6.8: Final reconstruction of "RK26" via the convolution method without a phase retrieval algorithm; The x and y axes denote pixels. 1 pixel is equal to 32 nm.

should be noticed that this reconstruction has been done without a phase retrieval algorithm, which is the main idea behind the use of the URA-Pattern as reference in the convolution method.

However, the quality of the final reconstruction is poor. Though the reconstructed object is visible, it does not show the fine details of the original object, seen in figure 6.1. Due to the special design of the sample, critical parameters for a good final reconstruction can be checked. Critical parameters are the geometry, the homogeneous illumination and the transmission of the Reference URA-Pattern.

The illumination and the transmission can be checked by looking at the cross-correlation between object and Reference URA-Pattern. The illumination and the transmission are not perfectly homogeneous. The illumination and the transmission vary along the Reference URA-Pattern by about a factor of 3 as will be seen below, which certainly reduces the quality of the final reconstruction. However, the non-uniformity of the exit wave behind the URA is only one part of the quality

reduction.
The quality of the holes in the Reference URA-Pattern has already been discussed. The hole sizes and the hole positions have been evaluated by looking at the SEM-picture of figure 6.2. It has been found that the positions of the holes are well placed, when the shear geometry is neglected. However, this shear geometry seems to be the main reason for the loss of the quality in the final reconstruction. Over the entire height of the Reference URA-Pattern the URA-Elements in the top line are shifted by almost a full length of an URA-Element relative to the URA-Elements in the bottom line. This shift should be considered in the Reconstruction URA-Pattern. However, shifting the URA-Elements in relation to each other in the Reconstruction URA-Pattern leads to additional empty spaces and with it to additional strong artifacts as seen in figure 3.6d. Therefore, the shear geometry is very disadvantageous and should be addressed at the fabrication level in future experiments.
Moreover, as said above, the quality of the final reconstruction depends on the hole sizes in the Reference URA-Pattern. While the sizes of the holes only have a small variance in the SEM-picture of figure 6.2, it will be shown below that the transmission through the different holes varies noticeable within the Reference URA-Pattern. According to section 3.3.4, this variation reduces the quality of the reconstruction further.
Another parameter, which influences the quality of the final reconstruction, is the correct size of the URA-Elements in the Reconstruction URA-Pattern. Though the URA-Element size can be determined, especially through the special design of the sample, the size of the URA-Element is not exactly 11 x 11 pixels, but on average 11.1 x 10.8. Due to the requirement for an integer number for the pixel size in the numerical treatment, the rounding to the next integer leads to a further reduction of the quality, according to section 3.3.2.

The sample "RK26" is specially designed in so far as two additional pinholes are placed near the Reference URA-Pattern as seen in figure 6.3. Both pinholes follow the separation conditions for many pinholes as described in section 2.2. After the Fourier transform of the hologram the upper pinhole in figure 6.3 creates low contrast cross-correlations. Therefore, it is not considered any further. The lower pinhole creates cross-correlations with good contrast as seen in figure 6.9a and

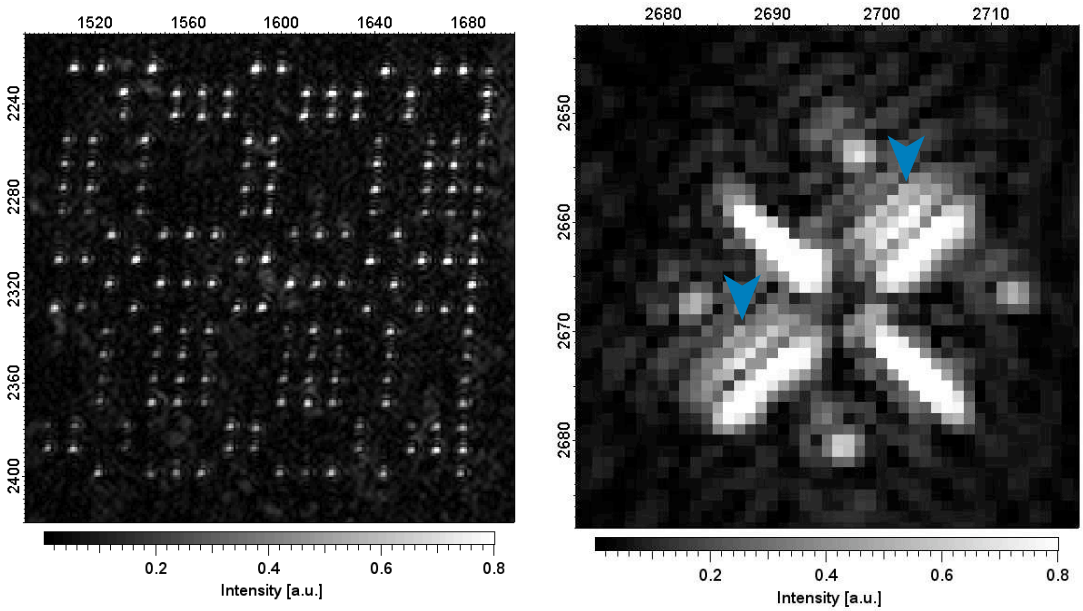

(a) Reconstructed URA

(b) Reconstructed object

Figure 6.9: Reconstructions via conventional FTH; The x and y axes denote pixels. 1 pixel is equal to 32 nm.

in figure 6.9b. Figure 6.9 shows the reconstructions via conventional FTH. Since the convolution method and conventional FTH are based on pinholes as reference points, figure 6.9b clearly shows how the object should be reconstructed via the convolution method. Moreover, since the reconstruction in figure 6.9b has only one pinhole as reference and the Reference URA-Pattern for the convolution method consists of 162 pinholes, the final reconstruction in the convolution method should be approximately 162 times as intense as the reconstruction in figure 6.9b.
Note that the lines indicated by arrows are not artifacts of the imaging process, but do correspond to the side wall slope as indicated in figure 6.1. Most likely sample creep during the FIB-milling process, as seen in figure 5.18, generated terraces which show up strongly in the transmission image.

In order to determine approximately the resolution in the convolution method, the resolution in the reconstruction via conventional FTH is determined first. In the conventional FTH-image shown in figure 6.9b the resolution is diffraction limited to 92 nm in the diagonal and to 130 nm along the coordinate axes.
In contrast, the resolution achieved in the convolution method is significantly

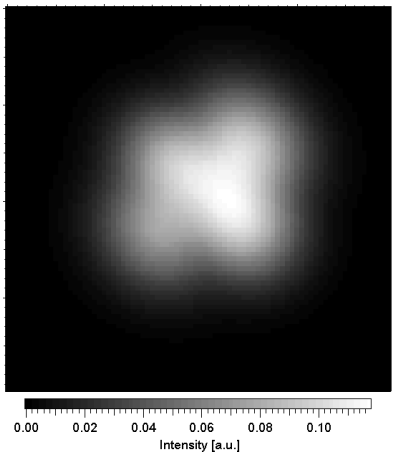

Figure 6.10: Convolution of the reconstructed object of figure 6.9b with a Gaussian shape profile; The x and y axes denote pixels. 1 pixel is equal to 32 nm.

poorer. The image obtained is shown in figure 6.8. To determine the resolution obtained in the convolution method the reconstruction in figure 6.9b is convolved with a Gaussian shaped profile. The FWHM of the Gaussian shape profile in the resulting convolution in figure 6.10 is 500 nm. Therefore, the resolution in the convolution method is determined to 500 nm.

In addition, the special design of the sample "RK26" unveils the transmission in the Reference URA-Pattern. The reconstructed URA-Pattern is seen in figure 6.9a. This image shows the exit surface intensity of the Reference URA-Pattern at the photon energy of 150 eV. It should be noted that this information is typically not available, e.g. from a SEM-picture. The reconstruction of the URA-Pattern shows that approximately 30% of the holes within the Reference URA-Pattern are entirely milled through, whereas 5% of the holes absorb to much light in order to contribute a significant amount to the final reconstruction. The rest of the holes has a reduced transmission, but still contributes to the final reconstruction. These different transmissions lead in the reconstruction via convolution to additional artifacts as mentioned previously.

The reconstruction via the convolution method is one way to achieve an image of the original object, when the URA-Pattern is used as reference. Since the original object and the Reference URA-Pattern are convolved via FTH, an alternative

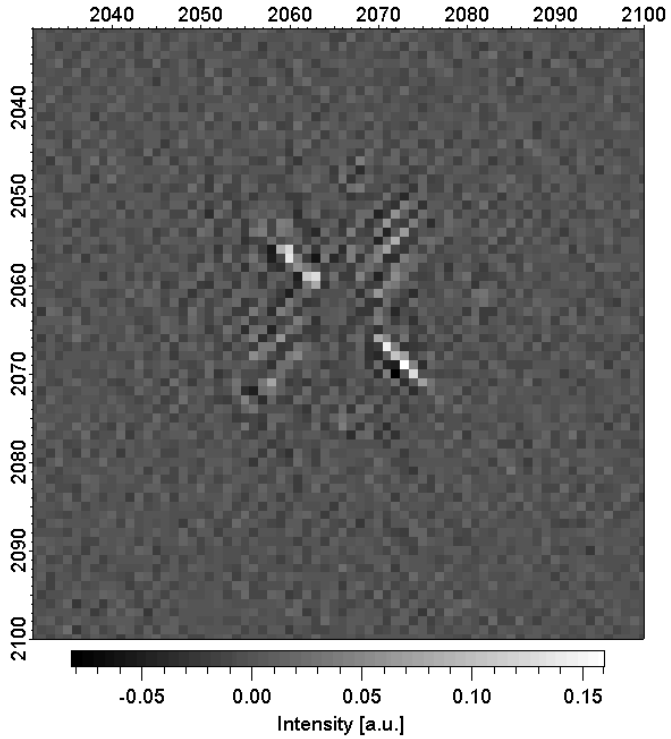

Figure 6.11: Final reconstruction of "RK26" via the deconvolution method with a heuristic "Wiener filter"; The x and y axes denote pixels. 1 pixel is equal to 32 nm.

way of reconstructing the original object is the reconstruction via deconvolution. This route is possible as the exit surface intensity of the Reference URA-Pattern is determined, which is shown in figure 6.9a.
A reconstruction via deconvolution, according to equation 3.5 in section 3.2, is presented in figure 6.11. The "Wiener filter" had a value of K=1e^{-9}.
Overall the quality of the final reconstruction in figure 6.11 is not as good as the quality of the reconstruction via conventional FTH. Though the resolution is high and identical to the resolution in conventional FTH with a single pinhole, the contrast is very low making many parts of the object hard to distinguish from the otherwise smooth background.

The quality of all three final reconstructions is compared again in figure 6.12. Under the condition the experiment has been done, including the production process, the reconstruction via conventional FTH achieves best results. The convolution

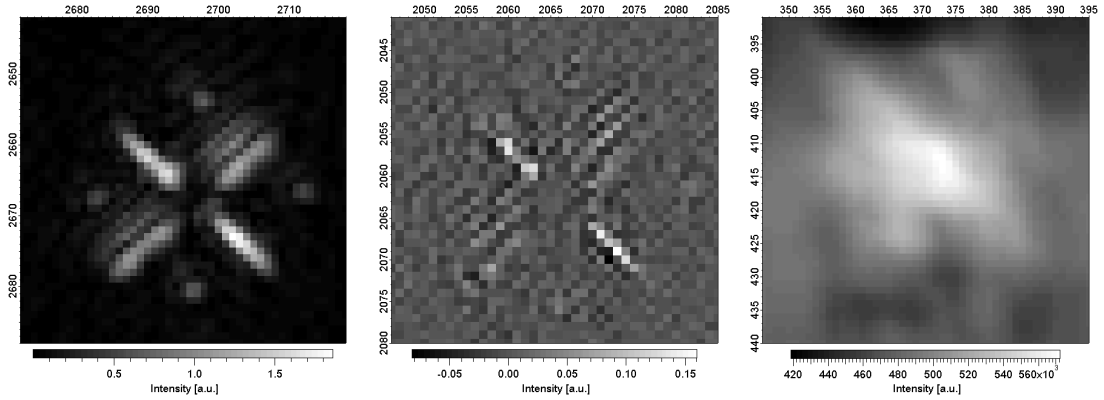

(a) Conventional FTH (b) Deconvolution (c) Convolution

Figure 6.12: Comparison of all three reconstruction methods; The x and y axes denote pixels. 1 pixel is equal to 32 nm.

method achieves the worst results: apparently signal intensity is gained at the expense of resolution. Moreover, the resolution of the reconstruction via deconvolution taking the real transmission of the URA-Pattern into account is very much superior to the results achieved via convolution.
The poor quality of the final reconstruction in the convolution method is mainly due to the shear distortion in the Reference URA-Pattern, as it is not considered in the reconstruction process. In contrast, in the final reconstruction via the deconvolution method the shear geometry is explicitly included in the reconstruction procedure leading to a better quality as in the case of the convolution method.
Future improvements can be made by optimizing especially the production quality of the Reference URA-Pattern. For a Reference URA-Pattern with high accuracy relative to the defined URA-geometry the convolution method is a promising technique to retain the resolution of a single pinhole and to increase the signal intensity.

Finally, one more note should be given to the Fourier transform of the hologram. Unexpectedly, additional object images are found near the reconstructed URA-Pattern as seen in figure 6.13. Although they cover a relative large area around the reconstructed URA-Pattern, these additional images do not effect the reconstructed URA-Pattern significantly. The additional images must arise from cross-correlations between the object and tiny pinholes. It seems that through the sputtering process of the polycrystalline gold mask, tiny channels have been cre-

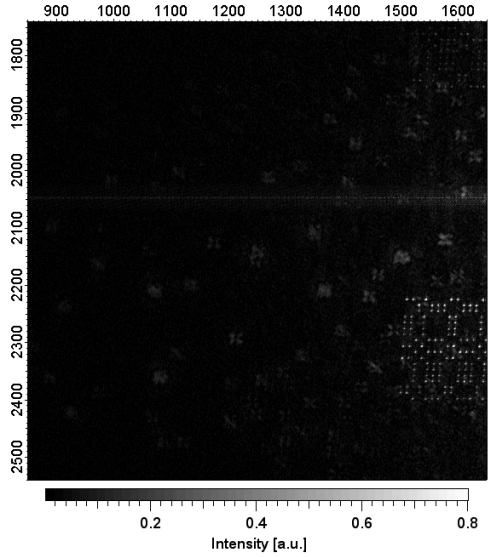

Figure 6.13: Reconstructed objects due to tiny cracks near the object; The x and y axes denote pixels. 1 pixel is equal to 32 nm.

ated, which act as tiny reference points. From the positions of the additional cross-correlations in the Fourier transformed hologram, their location on the mask can be determined. A reinspection of this area via SEM is planned for the near future in order to assess the nature of these unexpected reference beams.

6.2 Soft X-ray HERALDO

The use of a HERALDO-Pattern as reference in visible light has been reported recently [41]. Here, the use of the HERALDO-concept in the soft X-ray regime is demonstrated for the first time. For this proof-of-principle experiment the reference for HERALDO is a single line, which will create two reconstructed objects in one cross-correlation as described in section 4.2. The HERALDO-Sample for the experiment has been produced via FIB-milling by O. Wilhelmi from the FEI company according to our sample design.

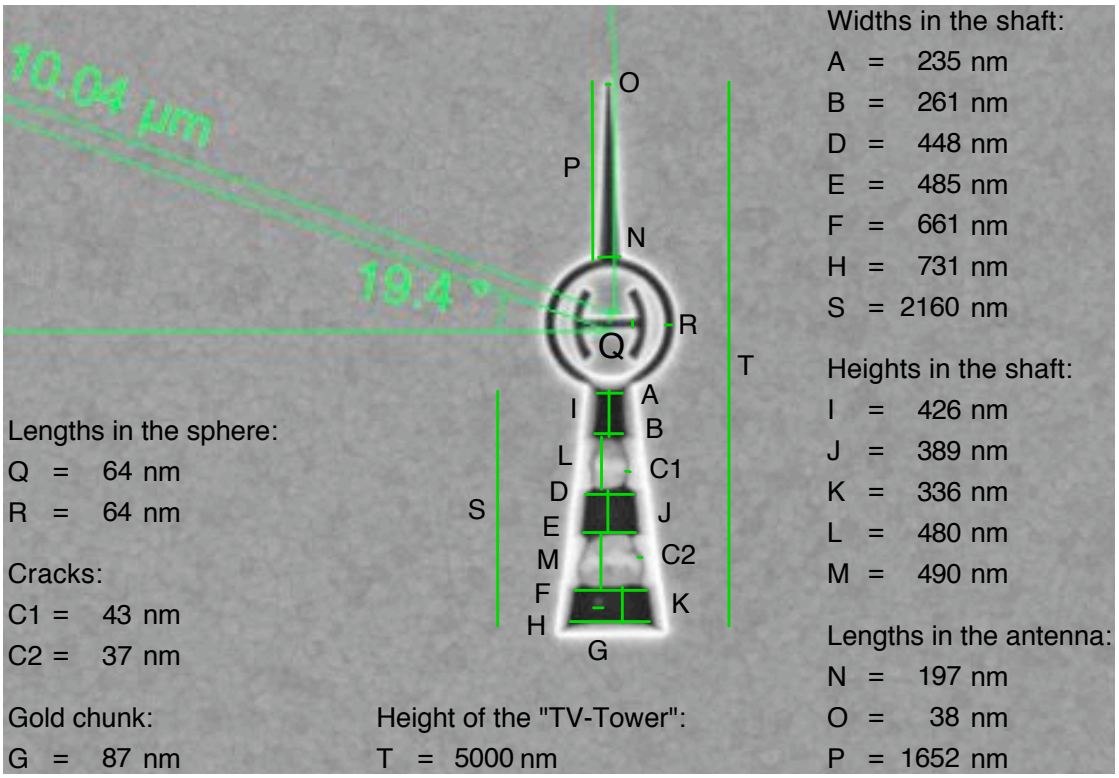

Figure 6.14: Object of the HERALDO-Sample "TV-Tower"

Sample "TV-Tower"

A FTH-experiment with the HERALDO-Sample "TV-Tower" has been carried out at beamline U41_PGM with a photon energy of 800 eV, which is equivalent to a wavelength of 1.5 nm. The sample is placed 600 mm behind the beamline focus point leading to a transverse coherence length of 66 μm. Further downstream the

CCD-camera is placed at a distance of 250 mm behind the sample. The diffraction limited resolution at this position is calculated to $d_{min_s} = 28\,\text{nm}$, $d_{min_l} = 20\,\text{nm}$ and $d_{max} = 14\,\mu\text{m}$.

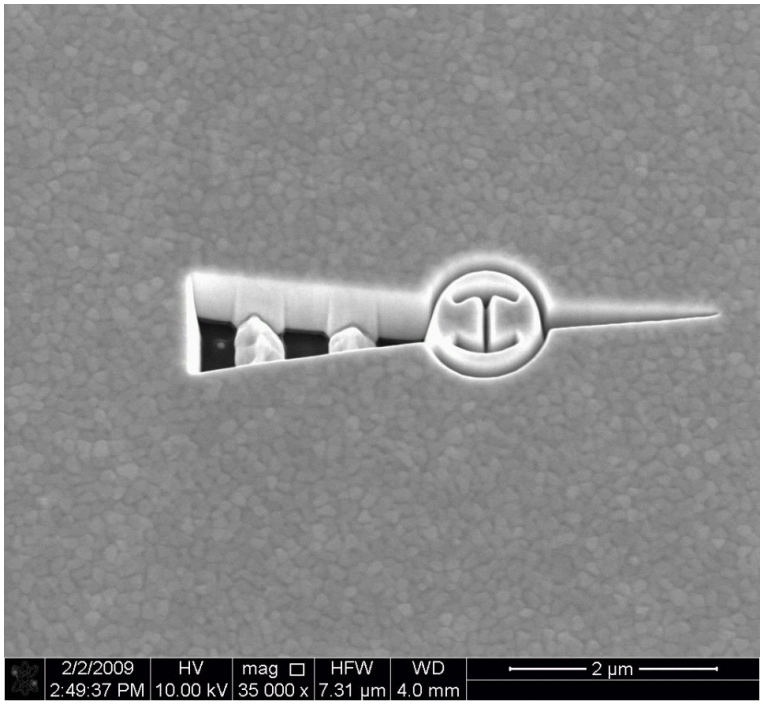

(a) Entire object

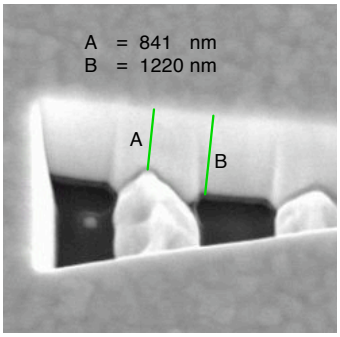

(b) Cutout

Figure 6.15: Side view of the object in the sample "TV-Tower"

The test object is displayed in figure 6.14, which represents the "TV-Tower" of Berlin. It will be seen that the object has some fine structures suitable for determining the resolution in the final reconstruction, like the thin antenna, the sphere of the "TV-Tower" and a gold chunk in the lowest opening of the "TV-Tower". While the gold chunk is hardly visible in figure 6.14, the gold chunk is better to see in figure 6.15. The gold chunk indicates the fact that the openings in the object are milled through the gold layer, but not through the Si_3N_4-layer.

In figure 6.15 an additional design feature is visible. The areas between the openings are only milled half through the gold layer. It will be shown that these areas are distinguishable in the final reconstruction leading to the ability to image objects with parts of different heights.

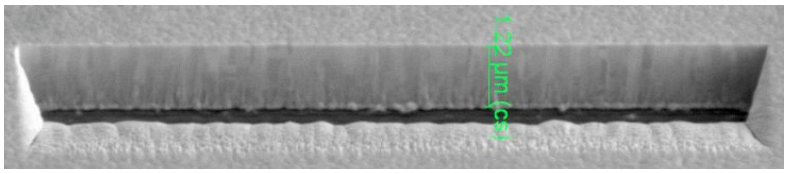

Figure 6.16: Thickness of the gold layer

Since figure 6.15 is a view under an angle of 54°, the thickness of the layer is visible. According to figure 6.16 the thickness of the gold layer is 1.22 μm. Although the gold layer is very thick leading to a transmission of 1.26e^{-8} times the incoming photons with an energy of 800 eV, it will be seen that the thickness is not high enough to absorb the entire beam leading to the detection of scattered and unscattered photons.

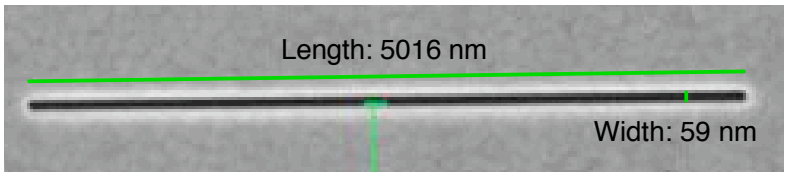

Figure 6.17: Reference line in the sample "TV-Tower"

The reference in the HERALDO-experiment is a line, which is seen in figure 6.17. The line is longer by a factor of six compared to the largest width in the object and, therefore, fulfilling the separation conditions for a HERALDO-Pattern as described in section 2.2. Furthermore, in figure 6.17 the quality of the reference line can be evaluated. There are no additional nooks visible along the line meaning only the ends will create the reconstructed objects. However, it will be seen in the final reconstruction that apparently nooks exist within the depth of the line, which influence the soft X-ray transmission and give rise to "ghost images".

In figure 6.18 the entire sample is seen. The distance between the reference line and the object is so high that the separation conditions of section 2.2 are clearly followed. The additional pinhole on the left side is not considered any further. It does not disturb the cross-correlations of interest.

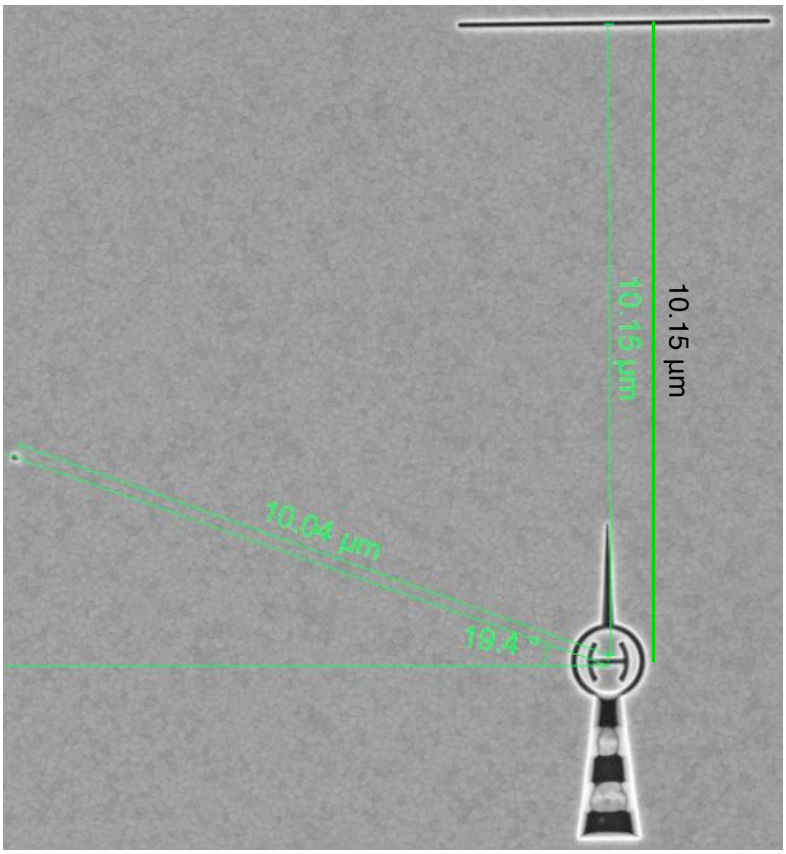

Figure 6.18: Front side of the entire sample "TV-Tower"

It is important to know for the evaluation of the final reconstruction, which structures are milled *through* the gold layer. The sample from the backside is seen in figure 6.19a.

The most important part is the reference line, which is seen in figure 6.19c. Also at the backside of the reference line no additional nooks are visible. Comparing figure 6.19c with figure 6.17 the transition length between highest transmission and highest absorption is determined by the difference of the line lengths to 103 nm at each end of the line. The transition length of 103 nm is only an approximation in regard to the final resolution, since the correct absorption of the light is not considered.

The object, seen in figure 6.19b, is not milled through the Si_3N_4-layer as mentioned above. However, it can be seen that only the big openings of the object are milled through the gold layer. All other fine structures consist of gold in their opening and are not visible.

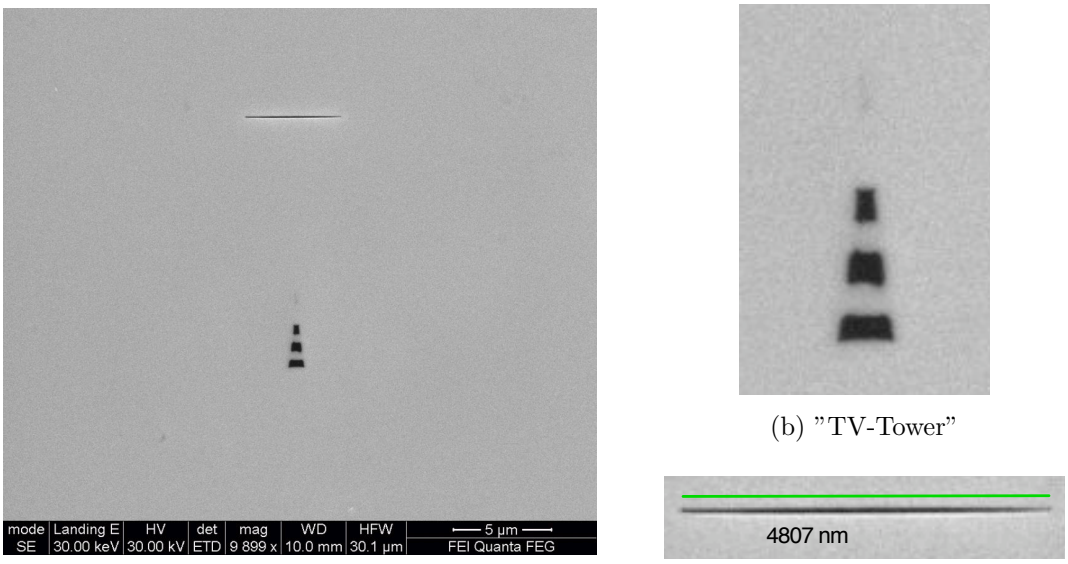

(a) Entire view

(b) "TV-Tower"

(c) Reference line

Figure 6.19: Back side of the HERALDO-Sample with its reference line and its object

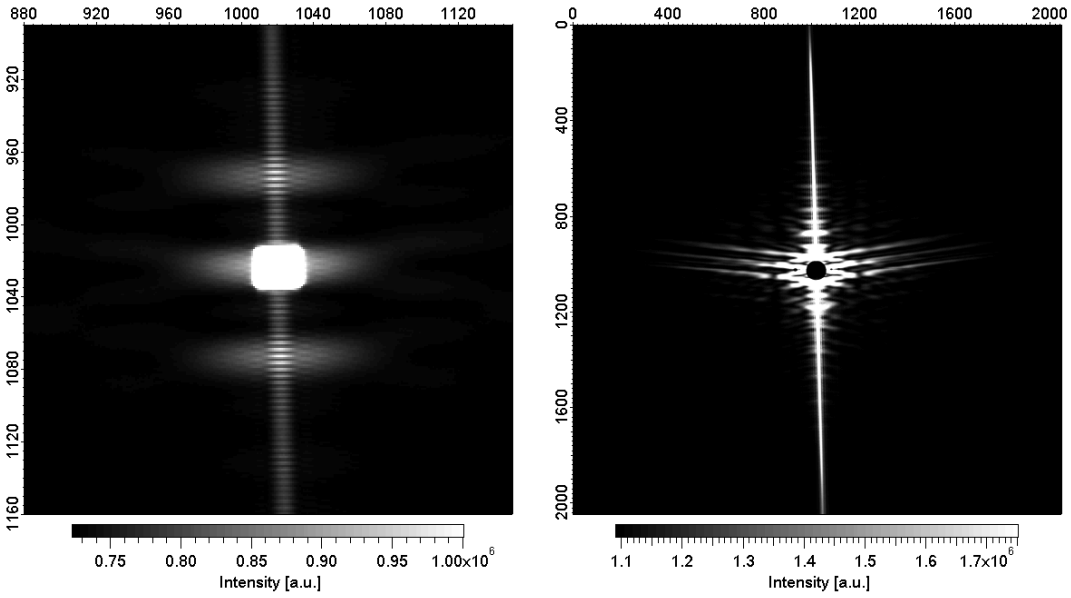

(a) The measured hologram without beamstop; sum of 400 exposures

(b) The measured hologram with beamstop; sum of 600 exposures

Figure 6.20: Measurements with the HERALDO-Pattern, without and with beamstop; The x and y axes denote pixels. 1 pixel is equal to $0.07\,\mathrm{nm}^{-1}$.

The HERALDO-Sample has been measured twice, once without beamstop and once with beamstop, shown in figure 6.20. Both measurements had an exposure time of 1 s and were accumulated 400 times without beamstop and 600 times with beamstop in order to improve the noise statistic.
In the middle of the hologram without beamstop, seen in figure 6.20a, the projection of the membrane window is clearly visible as a rounded square. The projection is generated by light which transmits through the membrane window without being scattered by the sample, despite a high absorption coefficient of $\mu = 15\,\frac{1}{\mu m}$.
The projection covers the area with low $|q|$-values, in which the first maxima of distances of 1.1 μm and larger along the x-axis and distances of 1.3 μm and larger along the y-axis are located. These distances will not be reconstructed properly. Since the object is larger than 1.3 μm along the y-axis, the background-level at two points separated by a distance larger than 1.3 μm along the y-axis is not comparable.

The dynamic range in the hologram is typically more expanded than the dynamic range of the CCD-camera. Through the transmission of the unscattered light, seen in figure 6.21a alone, the dynamic range in the hologram is enlarged even further. In order to increase the dynamic range later in the reconstruction to the same extent as the dynamic range in the hologram the second measurement is done including the beamstop as seen in figure 6.20b. The beamstop is large enough to cover all unscattered light.
The two measurements are stitched together in figure 6.21 in order to gain the requested high dynamic range. The stitched hologram alone is seen in figure 6.21b. Since the unscattered light creates strong artifacts after the Fourier transform of the hologram, the middle of the hologram is cut as seen in figure 6.21c and replaced by a 2D Gaussian shape profile as seen in figure 6.21d.

According to section 4.2 the object is reconstructed via equation (4.18) by applying firstly a multiplication and afterwards a Fourier transform. The angle α needed for the multiplication is determined in the hologram to $\alpha = $-1.55°.
The stitched hologram multiplied by the angle α is seen in figure 6.22. The correct angle α is confirmed by looking at the streaks created by the thin reference line in

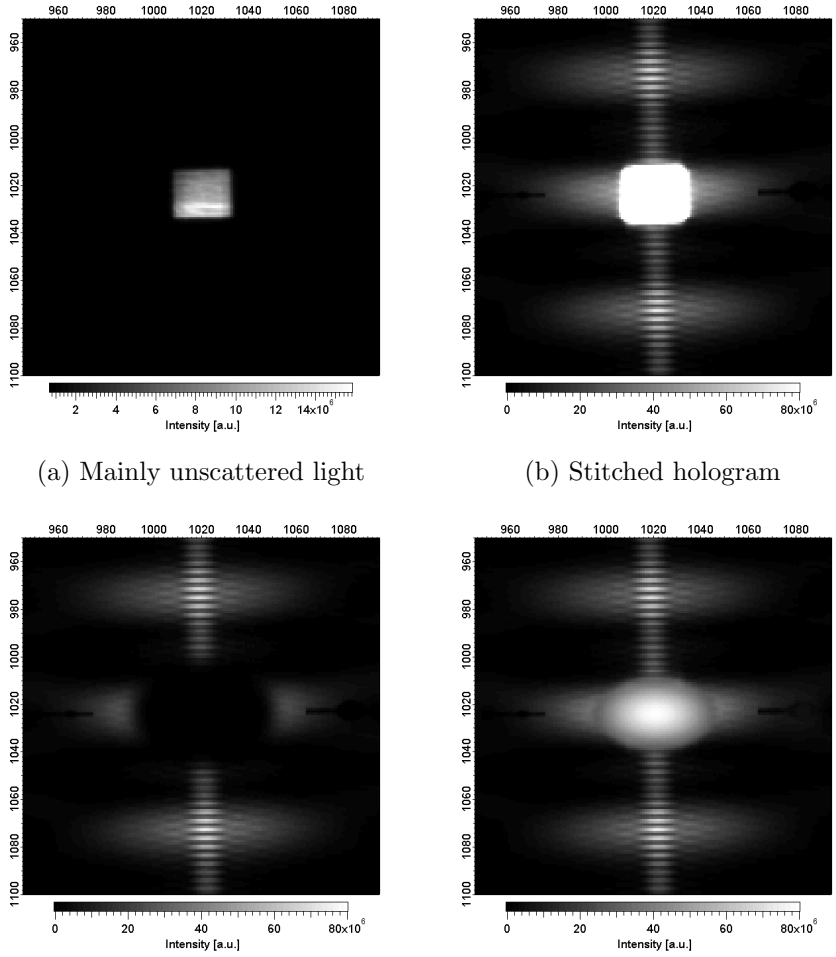

(a) Mainly unscattered light

(b) Stitched hologram

(c) Cut of the unscattered light

(d) Cut area replaced by 2D Gaussian shape profile

Figure 6.21: Stitching the holograms together; The x and y axes denote pixels. 1 pixel is equal to $0.07\,\mathrm{nm}^{-1}$.

figure 6.22, which are exactly split in two halves.

The Fourier transform of the multiplied hologram leads to the real part as seen in figure 6.23a, which shows clearly the different signs in the intensities of the reconstructed objects.
Taking the magnitude of the Fourier transformed hologram leads to the final reconstruction in figure 6.23b. In the associated cutout, seen in figure 6.24a, both reconstructed objects of the same cross-correlation have positive intensities as expected according to section 4.2.

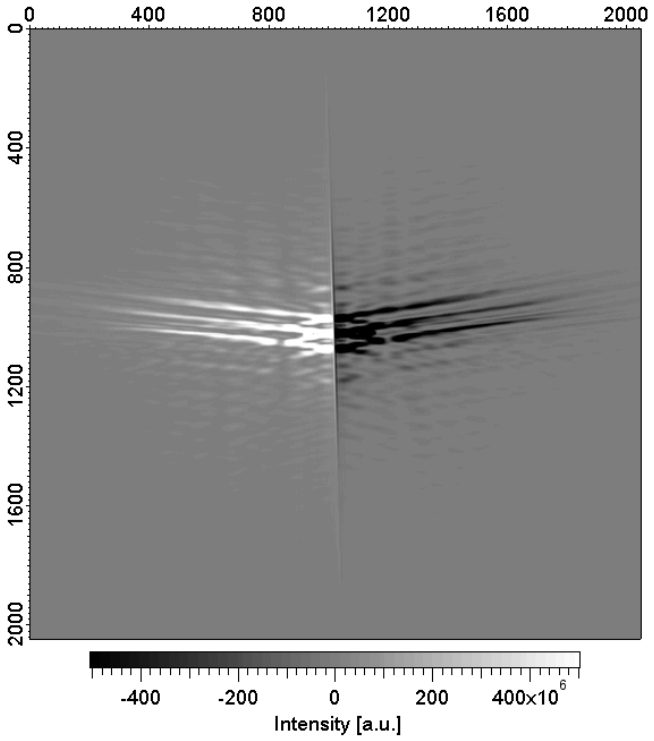

Figure 6.22: Stitched hologram multiplied by α; The x and y axes denote pixels. 1 pixel is equal to $0.07\,\mathrm{nm}^{-1}$.

The artifacts, which look like branches from the middle of the final reconstruction, are fortunately not disturbing the reconstructed object significantly. Beside the branch-like artifacts there are other artifacts visible between the reconstructed objects in figure 6.24a. These artificial structures appear to be faint "ghost images" created in between the end points of the reference line. It is suspected that these artifacts are due to the quality of the reference line. Tiny nooks in the side walls of the line - not visible in the SEM-images from the front and back - will act as weak references in the HERALDO-process.

The resolution in the final reconstruction is determined by looking at the antenna of the "TV-Tower" in figure 6.14. By comparing figure 6.24a with figure 6.14, the visible height of the reconstructed antenna is determined to $1.26\,\mu$m, which leads to a resolution of 48 nm. The high resolution is confirmed by the comparison with other fine structures like the crack between the two upper openings or by the gold chunk in the lowest opening of the "TV-Tower", seen in figure 6.25a and in figure

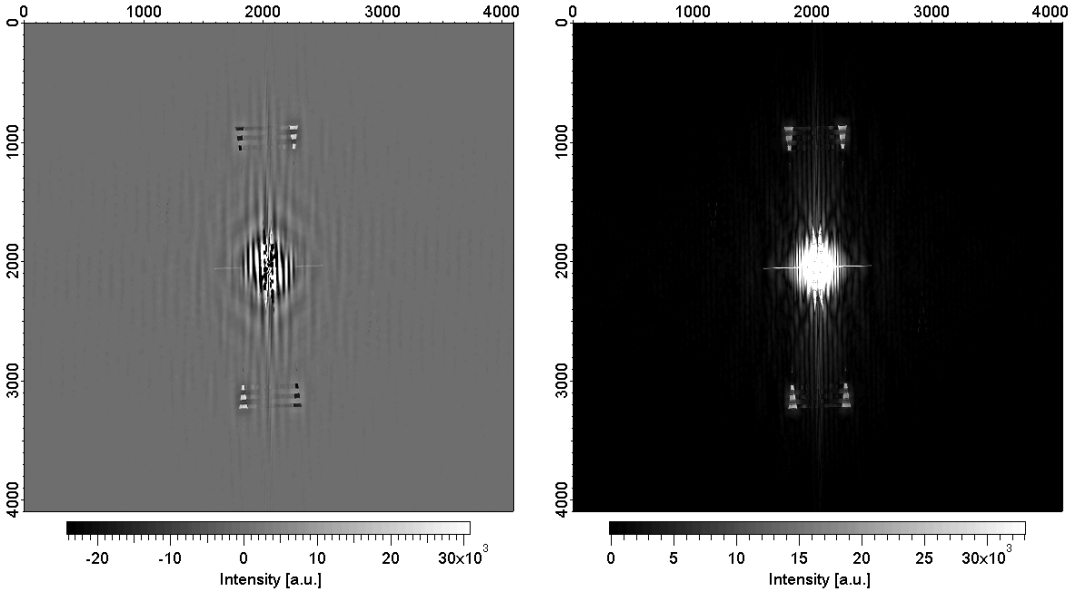

(a) Real part (b) Magnitude

Figure 6.23: The real part and the magnitude of the final reconstruction of the HERALDO-Sample; The x and y axes denote pixels. 1 pixel is equal to 14 nm.

6.25b, respectively. Features with a size of 3 pixels á 14 nm can be discerned.
In the final reconstruction with a false color scale, seen in figure 6.24b, the fine structures are clearer to see. Furthermore, in the false color image, it is well visible that the parts between the openings are not entirely milled through the gold layer, which are displayed by a green to yellow color.
From this successful reconstruction at 48 nm resolution it can be concluded that the HERALDO-concept is a suitable approach to generate a reference in soft X-ray FTH.

One advantage of the HERALDO-Pattern is the feasibility to be rotatable. In figure 6.26 the sample is rotated by $\gamma = -10°$. It is visible that the left reconstructed object has a worse resolution than the right reconstructed object. In section 4.4 it is explained that the resolution is increased by shorten and decreased by lengthen the transition length between highest transmission and highest absorption. Here, the edges of the reference line in this sample are not parallel to the beam under orthogonal illumination, therefore, the resolution increases and decreases by rotating the sample. The result can be seen comparing figure 6.26 with figure 6.24a.

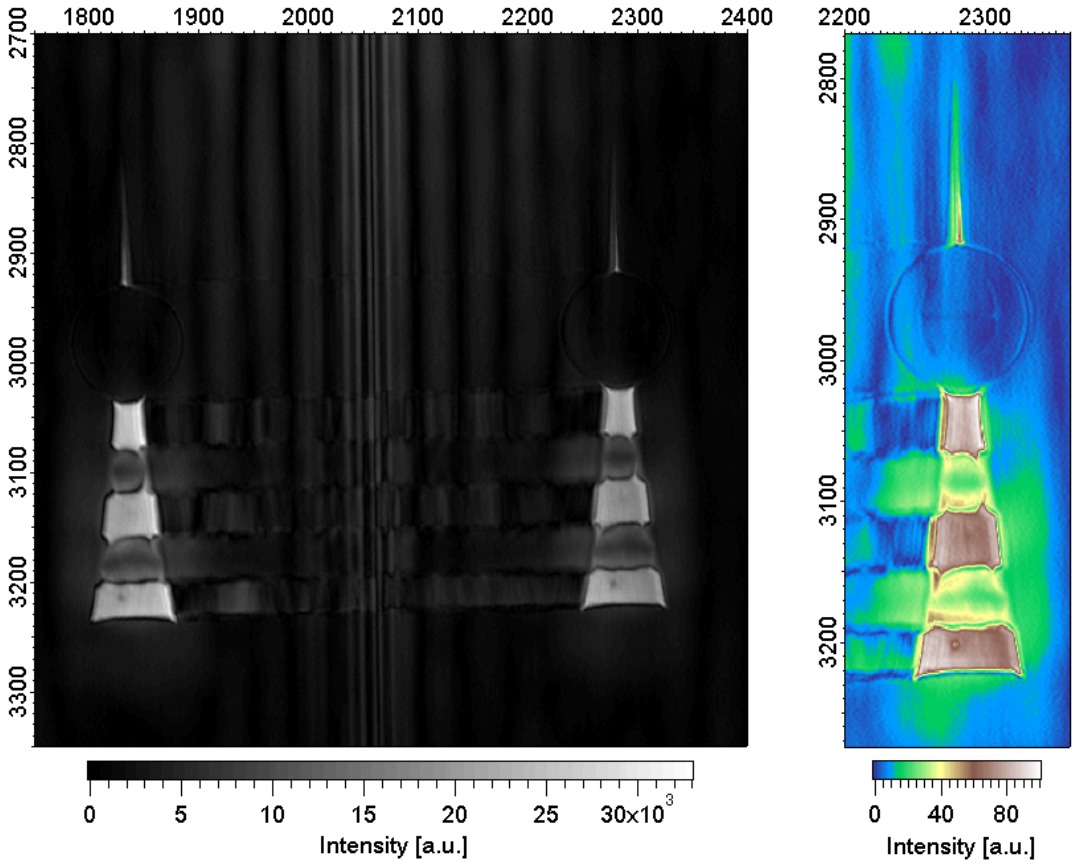

(a) Cutout

(b) Cutout in false color

Figure 6.24: Cutout with the magnitude of the final reconstruction of the HERALDO-Sample; The x and y axes denote pixels. 1 pixel is equal to 14 nm.

In figure 6.26 the sphere of the "TV-Tower" is taken for the determination of the resolution, which is 28 nm.
Furthermore, in the same comparison of figure 6.26 with figure 6.24a the increase of the contrast due to the rotation is visible. While rotating the sample, the path-length of the light to propagate through the sample increases resulting in a higher intensity difference between highest transmission and highest absorption. According to section 4.4 this increase of the intensity difference leads to an increase of the contrast in the final reconstruction.

Besides increasing the resolution, another advantage is that the rotation can be used to view the object under different angles, as explained in section 4.4. Viewing the object under different angles and detecting the absorption along the direction

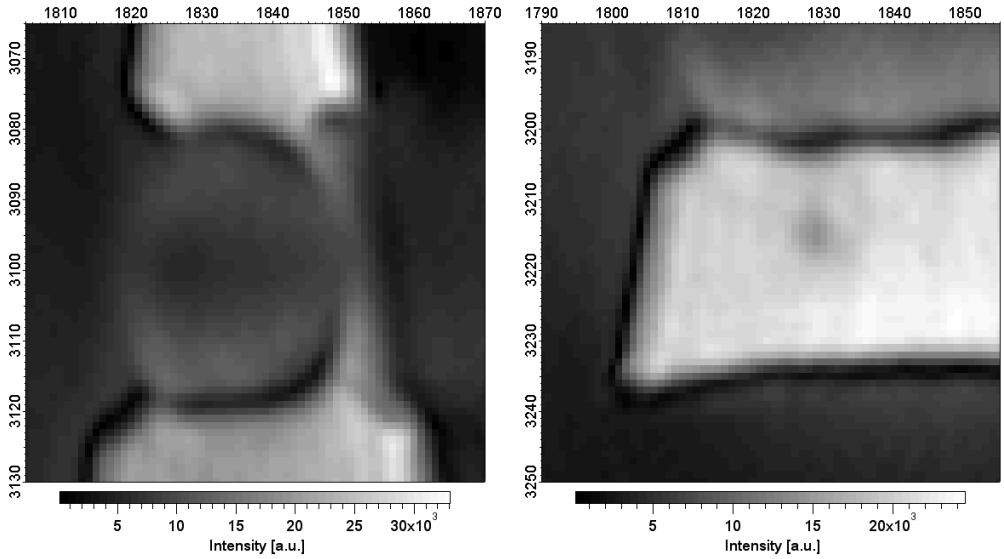

(a) Crack (b) Gold chunk

Figure 6.25: Parts in the shaft of the "TV-Tower" for the confirmation of the high resolution; The x and y axes denote pixels. 1 pixel is equal to 14 nm.

of view different projections are recordable. From a suitable number of projections a 3D image can be retrieved in principle, showing the spatial absorption inside the object. To illustrate the concept, figure 6.27 shows the object under 0°, 10° and 20°. While the data quality certainly needs to be improved, one can see that different projections with different information content are obtained.
It is thus clear that tomography will be a principal possibility with a HERALDO-Sample, although the fact that the image resolution changes as a function of angle is an impediment.

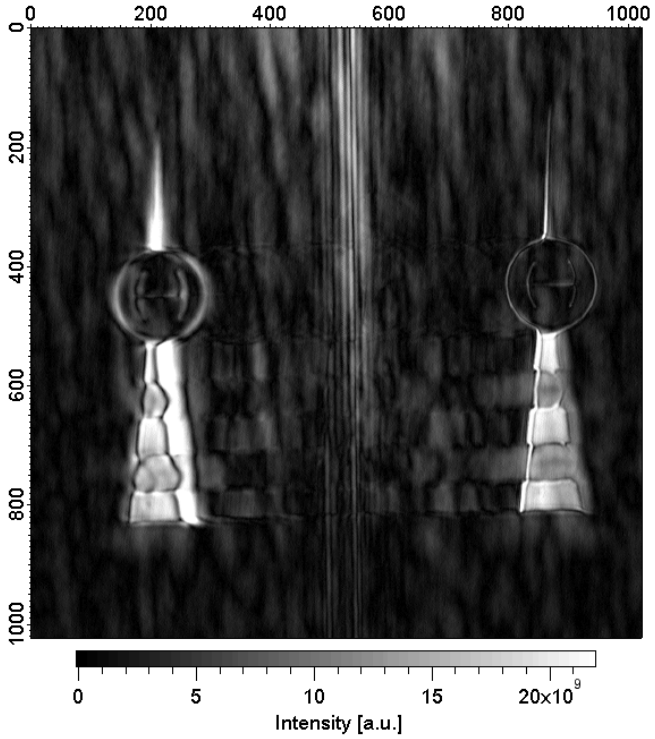

Figure 6.26: Sample "TV-Tower" rotated by -10°; The x and y axes denote pixels. 1 pixel is equal to 14 nm.

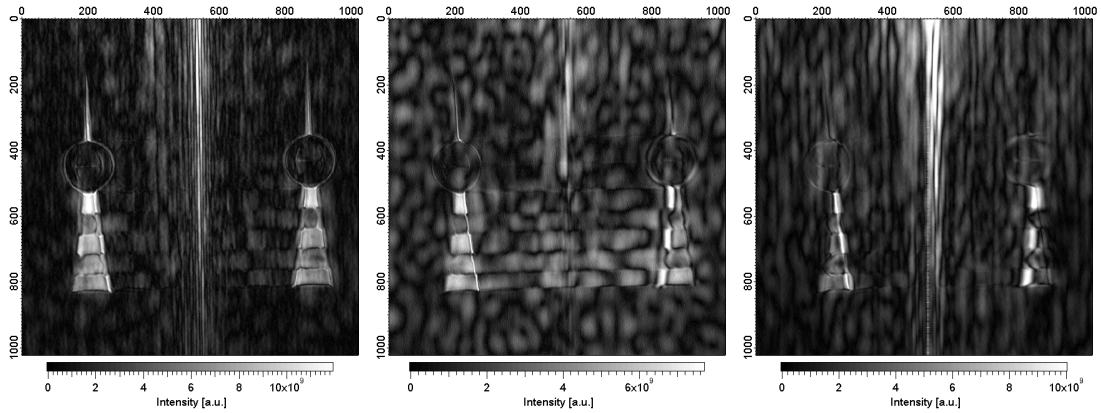

(a) $\gamma = 0°$ (b) $\gamma = 10°$ (c) $\gamma = 20°$

Figure 6.27: Rotation series with a HERALDO-Sample; The x and y axes denote pixels. 1 pixel is equal to 14 nm.

Chapter 7

Summary and Outlook

In soft X-ray FTH in transmission mode several parameters, from the quality of the reference structure to the transverse coherence length of the incoming beam, are under investigation in order to gain a better quality of the reconstructed object in the final reconstruction. In experiments with a short exposure time one parameter is especially longing for improvement, the signal intensity. In conventional FTH with only one single pinhole the signal intensity can be improved by increasing the exposure time, if the object is static. However, when dynamics in objects are investigated or when investigated objects are not radiation resistant, this is not always an option. In such cases, a possibility to increase the signal intensity is most welcome.

In this thesis it is presented that the signal intensity can be increased, when the number of reference points is raised, which can happen in two different ways. Either the layout of conventional FTH with its one pinhole is modified by increasing the number of pinholes or a new layout is taken and the reference points are mathematically generated after the hologram is detected. The former one leads to the multiple reference pattern, whereas the latter one leads to the extended reference pattern.

The first reference pattern investigated in this thesis is the URA-Pattern, which belongs to the multiple reference pattern. The URA-Pattern is a compact reference pattern, in which the pinholes are arranged in a specific way, so that all distances between them appear equally often. Although each pinhole follows the separation condition of conventional FTH, the distances between the pinholes are

so close that the reconstructed objects overlap each other.
In order to disentangle the reconstructed object the complex conjugate cross-correlation is convolved with a second URA-Pattern, the Reconstruction URA-Pattern. The Reconstruction URA-Pattern and the Reference URA-Pattern are based on the same Basic URA-Pattern, except for the RSH-value, which describes the ratio between the spacing and the diameter of the holes. The RSH-value is the most important parameter in order to disentangle the reconstructed object without the need of a phase retrieval algorithm. The RSH-value in the Reconstruction URA-Pattern is always zero, independent of the RSH-value in the Reference URA-Pattern.
In order to use the convolution method properly, the Reference URA-Pattern must follow several requirements. Beside being produced with a very high accuracy and being entirely homogeneously illuminated, the Reference URA-Pattern must be larger than the object.

With the available FIB of the Helmholtz-Zentrum Berlin a sample with a test object and an URA-Pattern as reference has been produced. The sample consists of a self-supporting Basic URA-Pattern with 162 pinholes as reference. The aim of the first measurement is to show the ability of the convolution method to reconstruct an object without a phase retrieval algorithm under the condition that the Reference URA-Pattern is a self-supporting URA-Pattern with RSH>0.
Due to the 162 times more pinholes in the Reference URA-Pattern compared to conventional FTH with its one pinhole, the signal intensity in the final reconstruction should be increased by a factor of approximately 162. Furthermore, the resolution should be as good as in conventional FTH, which is 130 nm.
However, the quality of the final reconstruction is poor, the expected superiority of the convolution method compared to conventional FTH could not be shown.
There are several parameters, which need to be improved in order to make the convolution method competitive with conventional FTH. The most important improvement is the quality of the Reference URA-Pattern. At first the shear geometry in the Reference URA-Pattern should be avoided in the fabrication process by any means. The shear geometry mainly reduces the quality of the final reconstruction. Secondly, the size of the pinholes must be produced more homogeneously. Thirdly, the coherent illumination of the sample should be more homogeneously, too.

The same URA-Sample includes a pinhole located next to the object and the Reference URA-Pattern. The pinhole is used in order to reconstruct the object separately via conventional FTH. This reconstruction allows the comparison of the convolution method with conventional FTH. Under the given circumstances the reconstruction via conventional FTH leads to a superior reconstructed object.
In the chosen mask design the pinhole reconstructs the Reference URA-Pattern as well. The convolved object can thus be reconstructed by a deconvolution method as the Reference URA-Pattern is well characterized in its transmission at the wavelength used in the experiment. The shear deformation of the Reference URA-Pattern is automatically accounted for in the deconvolution method, which is the reason why the reconstruction via deconvolution is superior to the reconstruction via convolution under the given circumstances. The resolution achieved via deconvolution is 130 nm, the same as in conventional FTH with a single pinhole. However, the contrast of the final reconstruction via deconvolution is poor compared to conventional FTH.
The deconvolution with an URA-Pattern as reference is new in so far that the URA-Pattern for the deconvolution is reconstructed in the same measurement as the cross-correlation between object and Reference URA-Pattern, providing more precise information about the Reference URA-Pattern like the real transmission of the pinholes.

The second reference pattern introduced in this thesis belongs to the extended reference pattern, the HERALDO-Pattern. The HERALDO-Pattern consists only of reference structures, which include corners or kinks. These corners or kinks in the reference structure of a HERALDO-Sample act as reference points. The reference points have to be mathematically generated after the hologram is detected. In the Fourier transformed hologram a reference point is obtained by taking the derivative along the edges at a corner or a kink. The higher the intensity difference between highest transmission and highest absorption at the edge perpendicular to the direction of the derivation the higher is the contrast in the final reconstruction. The resolution depends on the transition length between highest transmission and highest absorption at this edge. The smaller the transition the higher is the resolution.

So far, HERALDO-experiments have only been reported using visible radiation. In this thesis first soft X-ray HERALDO-experiments are presented. The HERALDO-Pattern consists of a single line with its ends acting as reference points. To produce the reference points the derivative has been taken along the line length. Using the HERALDO-approach it has been possible to encode and reconstruct an image of a test object. A resolution of 48 nm has been achieved.
Furthermore, a special feature of the HERALDO-Pattern is presented. The special feature is to rotate the entire sample, allowing to increase the resolution and the contrast in the final reconstruction. With a rotation of -10° a resolution of 28 nm is achieved.
In principle a rotation can be used to view the sample under different angles leading to the feasibility to do tomography. This approach is demonstrated by an experiment with a sample rotation of 10° and 20°.
The results in the HERALDO-measurement can be improved by increasing the quality of the reference line like producing sharp corners and avoiding any hidden nooks.

Comparing the multiple and the extended reference pattern leads to advantages and disadvantages for both reference patterns.
The advantage of the URA-Pattern is its compactness and its small open area. The disadvantage is its complexity to produce the accurate pinhole pattern.
The advantage of the HERALDO-Pattern is its ease of production and the ability to vary the contrast and the resolution in the final reconstruction by rotating the sample. The disadvantage is its wide opening and the higher sensitivity to noise compared to multiple reference patterns.
Despite the disadvantages for each reference pattern both kinds of reference patterns are interesting for future soft X-ray FTH-experiments. They both have the potential to increase the signal intensity during a constant exposure time. Especially for future single shot FEL-experiments with an exposure time of several femtoseconds, the multiple and the extended reference pattern are of interest.
In addition the feasibility of the HERALDO-Pattern to be rotatable may lead to new kinds of experiments with depth resolution.

Bibliography

[1] J.G. Ables. Fourier transform photography: A new method for x-ray astronomy. *Proc. Astron. Soc. Australia*, 1:172–173, 1968.

[2] R. Accorsi and R.C. Lanza. Near-field artifact reduction in planar coded aperture imaging. *Applied Optics*, 40(26):4697–4705, 2001.

[3] S. Boutet, M.J. Bogan, A. Barty, M. Frank, W.H. Benner, S. Marchesini, M.M. Seibert, J. Hajdu, and H.N. Chapman. Ultrafast soft x-ray scattering and reference-enhanced diffractive imaging of weakly scattering nanoparticles. *Journal Of Electron Spectroscopy And Related Phenomena*, 166-167:65–73, 2008.

[4] E.O. Brigham. *FFT-Anwendungen*. R. Oldenbourg Verlag, 1997.

[5] C. Brown. Multiplex imaging with multiple-pinhole cameras. *J. Appl. Phys.*, 45(4):1806–1811, 1974.

[6] C.M. Brown. Multiplex imaging and random arrays. *Dissertation*, 1972.

[7] A. Busboom. Construction of pseudo-noise arrays from quadratic residues. *Signal Processing*, 72(1):33–38, 1999.

[8] A. Busboom, H. Elders-Boll, and H.D. Schotten. Combinatorial design of near-optimum masks for coded aperture imaging. *IEEE icassp97*, 4:2817–2820, 1997.

[9] A. Busboom, H. Elders-Boll, and H.D. Schotten. Uniformly redundant arrays. *Experimental Astronomy*, 8(2):97–123, 1998.

[10] A. Busboom and H.D. Luke. Hexagonal binary arrays with perfect correlation. *Applied Optics*, 40(23):3894–3900, 2001.

[11] A. Busboom, H.D. Schotten, and H. EldersBoll. Coded aperture imaging with multiple measurements. *Journal Of The Optical Society Of America A-Optics Image Science And Vision*, 14(5):1058–1065, 1997.

[12] T. Butz. *Fouriertransformation für Fußgänger.* Vieweg+Teubner, 6.auflage edition, 2009.

[13] T.M. Cannon. Tomographical imaging using uniformly redundant arrays. *Applied Optics*, 18(7):1052–1057, 1979.

[14] T.M. Cannon and E.E. Fenimore. A class of near-perfect coded apertures. *Ieee Transactions On Nuclear Science*, 25(1):184–188, 1978.

[15] E. Caroli, J.B. Stephen, G. Di-Cocco, L. Natalucci, and A. Spizzichino. Coded aperture imaging in x- and gamma-ray astronomy. *Space Science Reviews*, 45(3):349–403, 1987.

[16] W. Chao, B.D. Harteneck, J.A. Liddle, E.H. Anderson, and D.T. Attwood. Soft x-ray microscopy at a spatial resolution better than 15 nm. *Nature*, 435(7046):1210–1213, 2005.

[17] R. Chen, H. Chang, Y. Huang, D. Tsai, S. Chattopadhyay, and K.H. Chen. Growth and characterization of vertically aligned self-assembled iro2 nanotubes on oxide substrates. *Journal of Crystal Growth*, 271:105–112, 2004.

[18] Y.W. Chen and K. Kishimoto. Tomographic resolution of uniformly redundant arrays coded aperture. *Review of Scientific Instruments*, 74(3):2232–2235, 2003.

[19] S. Clair, C. Rabot, Y. Kim, and M. Kawai. Adsorption mechanism of aligned single wall carbon nanotubes at well defined metal surfaces. *Journal Of Vacuum Science & Technology B*, 25(4):1143–1146, 2007.

[20] D.Attwood. *Soft X-rays and Extreme Ultraviolet Radiation.* Cambridge University Press, 1999.

[21] R.H. Dicke. Scatter-hole cameras for x-rays and gamma rays. *Astrophysical Journal*, 153(2):L101–L106, 1968.

[22] S. Eisebitt. X-ray holography - the hole story. *Nature Photonics*, 2(9):529–530, 2008.

[23] S. Eisebitt, M. Lörgen, W. Eberhardt, J. Lüning, S. Andrews, and J. Stöhr. Scalable approach for lensless imaging at x-ray wavelengths. *Applied Physics Letters*, 84(17):3373–3375, 2004.

[24] S. Eisebitt, M. Lörgen, W. Eberhardt, J. Lüning, and J. Stöhr. Lensless x-ray imaging of magnetic materials: basic considerations. *Appl Phys A: Materials Science & Processing*, 80(5):921–927, 2005.

[25] S. Eisebitt, M. Lörgen, W. Eberhardt, J. Lüning, J. Stöhr, C.T. Rettner, O. Hellwig, E.E. Fullerton, and G Denbeaux. Polarization effects in coherent scattering from magnetic specimen: Implications for x-ray holography, lensless imaging, and correlation spectroscopy. *Physical Review B*, 68(10):104419, 2003.

[26] S. Eisebitt, J. Lüning, W.F. Schlotter, M. Lörgen, O. Hellwig, W. Eberhardt, and J. Stöhr. Lensless imaging of magnetic nanostructures by x-ray spectroholography. *Nature*, 432(7019):885–888, 2004.

[27] E.E. Fenimore. Coded aperture imaging: predicted performance of uniformly redundant arrays. *Applied Optics*, 17(22):3562–3570, 1978.

[28] E.E. Fenimore. Coded aperture imaging: the modulation transfer function for uniformly redundant arrays. *Applied Optics*, 19(14):2465–2471, 1980.

[29] E.E. Fenimore. Time-resolved and energy-resolved coded aperture images with ura tagging. *Applied Optics*, 26(14):2760–2769, 1987.

[30] E.E. Fenimore and T.M. Cannon. Coded aperture imaging with uniformly redundant arrays. *Applied Optics*, 17(3):337–347, 1978.

[31] E.E. Fenimore and T.M. Cannon. Uniformly redundant arrays: digital reconstruction methods. *Applied Optics*, 20(10):1858–1864, 1981.

[32] E.E. Fenimore, T.M. Cannon, D.B. Van-Hulsteyn, and P. Lee. Uniformly redundant array imaging of laser driven compressions: preliminary results. *Applied Optics*, 18(7):945–947, 1979.

[33] E.E. Fenimore and G.S. Weston. Fast delta hadamard transform. *Applied Optics*, 20(17):3058–3067, 1981.

[34] M.H. Finger and T.A. Prince. Hexagonal uniformly redundant arrays for coded-aperture imaging. *In NASA. Goddard Space Flight Center 19th Intern. Cosmic Ray Conf.*, 3:295–298, 1985.

[35] K.J. Gaffney and H.N. Chapman. Imaging atomic structure and dynamics with ultrafast x-ray scattering. *Science*, 316(5830):1444–1448, 2007.

[36] G.R. Gindi, R.G. Paxman, and H.H. Barrett. Reconstruction of an object from its coded image and object constraints. *Applied Optics*, 23(6):851–856, 1984.

[37] J.W. Goodman. *Introduction to Fourier Optics*. Roberts & Company Publishers, third edition edition, 2005.

[38] S.R. Gottesman and E.E. Fenimore. New family of binary arrays for coded aperture imaging. *Applied Optics*, 28(20):4344–4352, 1989.

[39] E. Gührs, C.M. Günther, R. Könnecke, B. Pfau, and S. Eisebitt. Holographic soft x-ray omni-microscopy of biological specimens. *Optics Express*, 17(8):6710, 2009.

[40] M. Guizar-Sicairos and J.R. Fienup. Holography with extended reference by autocorrelation linear differential operation. *Optics Express*, 15(26):17592–17612, 2007.

[41] M. Guizar-Sicairos and J.R. Fienup. Direct image reconstruction from a fourier intensity pattern using heraldo. *Optics Letters*, 33(22):2668–2670, 2008.

[42] C.M. Günther. Switching behavior of magnetic nanostructures investigated by x-ray spectro-holography. *Diplomarbeit*, 2006.

[43] W.S. Haddad, I. McNulty, J.E. Trebes, E.H. Anderson, R.A. Levesque, and L. Yang. Ultrahigh-resolution x-ray tomography. *Science*, 266(5188):1213–1215, 1994.

[44] E. Hecht. *Optics*. Pearson Education, international edition edition, 2002.

[45] O. Hellwig, S. Eisebitt, W. Eberhardt, W.F. Schlotter, J. Lüning, and J. Stöhr. Magnetic imaging with soft x-ray spectroholography. *J. Appl. Phys.*, 99(8):08H307, 2006.

[46] H.He, U. Weierstall, J.C.H. Spence, M. Howells, H.A. Padmore, S. Marchesini, and H.N. Chapman. Use of extended and prepared reference objects in experimental fourier transform x-ray holography. *Applied Physics Letters*, 85(13):2454–2456, 2004.

[47] G. Indebetouw and W. Shing. Scanning optical reconstruction of coded aperture images. *Applied Physics B: Lasers and Optics*, 27:69–76, 1982.

[48] J. Jimenez, P. Olmos, J.L. de Pablos, and J.M. Perez. Gamma ray imaging using coded aperture masks: a computer simulation approach. *Applied Optics*, 30(5):549–560, 1991.

[49] T. Kato and R. Hatakeyama. Formation of freestanding single-walled carbon nanotubes by plasma-enhanced cvd. *Chem. Vap. Deposition*, 12:345–352, 2006.

[50] T. Kato, G. Jeong, T. Hirata, and R. Hatakeyama. Structure control of carbon nanotubes using radio-frequency plasma enhanced chemical chemical vapor deposition. *Thin Solid Films*, 457:2–6, 2004.

[51] P. Kim, S. Baik, and K.Y. Suh. Capillarity-driven fluidic alignment of single-walled carbon nanotubes in reversibly bonded nanochannels. *Small*, 4(1):92–95, 2008.

[52] W.K. Klemperer. Very large array configurations for the observation of rapidly varying sources. *Astronomy and Astrophysics Supplement*, 15:449–451, 1974.

[53] C. Kocabas, S. Hur, A. Gaur, M. Meitl, M. Shim, and J.A. Rogers. Guided growth of large-scale, horizontally aligned arrays of single-walled carbon nanotubes and their use in thin-film transistors. *Small*, 1(11):1110–1116, 2005.

[54] H. Lang, L. Liu, and Q. Yang. Design of nras having higher aperture opening ratio and autocorrelation compression ratio by means of a global optimization method. *Optik - International Journal for Light and Electron Optics*, 118(10):491–494, 2007.

[55] H. Lang, L. Liu, and Q. Yang. Design of uras by direct global optimization algorithm. *Optik-International Journal for Light and Electron Optics*, 120:370–373, 2007.

[56] H. Lang, L. Liu, and Q. Yang. A novel method to design flexible uras. *J. Opt. A: Pure Appl. Opt.*, 9:502–505, 2007.

[57] H. Lang, L. Liu, and Q. Yang. A novel three-dimensional imaging method by means of coded cameras array recording and computational reconstruction. *Optik - International Journal for Light and Electron Optics*, 118(4):168–174, 2007.

[58] K. Liu, Y. Sun, L. Chen, C. Feng, X. Feng, K. Jiang, Y. Zhao, and S. Fan. Controlled growth of super-aligned carbon nanotube arrays for spinning continuous unidirectional sheets with tunable physical properties. *Nano Letters*, 8(2):700–705, 2008.

[59] H.D. Lueke. Binary odd-periodic complementary sequences. *Ieee Transactions On Information Theory*, 43(1):365–367, 1997.

[60] H.D. Lueke and A. Busboom. Binary arrays with perfect odd-periodic autocorrelation. *Applied Optics*, 36(26):6612–6619, 1997.

[61] H.D. Luke and A. Busboom. Mismatched filtering of periodic and odd-periodic binary arrays. *Applied Optics*, 37(5):856–864, 1998.

[62] S. Marchesini, S. Boutet, A.E. Sakdinawat, M.J. Bogan, S. Bajt, A. Barty, H.N. Chapman, M. Frank, S.P. Hau-Riege, A. Szoeke, C. Cui, D.A. Shapiro, M.R. Howells, J.C.H. Spence, J.W. Shaevitz, J.Y. Lee, J. Hajdu, and M.M. Seibert. Massively parallel x-ray holography. *Nature Photonics*, 2(9):560–563, 2008.

[63] I. McNulty, J. Kirz, C. Jacobsen, E.H. Anderson, M.R. Howells, and D.P. Kern. High-resolution imaging by fourier transform x-ray holography. *Science*, 256(5059):1009–1012, 1992.

[64] I. McNulty, J. Trebes, J. Brase, T. Yorkey, R. Levesque, H. Szoke, E.H. Anderson, C. Jacobsen, and D. Kern. Experimental demonstration of high resolution three-dimensional x-ray holography. *Proceedings of SPIE*, 1741:78–84, 1992.

[65] L. Mertz and N.O. Young. Fresnel transformations of images. *SPIE milestone series ms*, pages 305–310, 1961.

[66] D.M. Paganin. *Coherent X-Ray Optics*. Oxford University Press, 2006.

[67] R.G. Paxman, W.E. Smith, and H.H. Barrett. Two algorithms for use with an orthogonal-view coded-aperture system. *J Nuci Med*, 25:700–705, 1984.

[68] S.G. Podorov, K.M. Pavlov, and D.M. Paganin. A non-iterative reconstruction method for direct and unambiguous coherent diffractive imaging. *Optics Express*, 15(16):9954–9962, 2007.

[69] J. Saez-Landete, J. Alonso, and E. Bernabeu. Design of two-dimensional zero reference codes by means of a global optimization method. *Optics Express*, 13(11):4230–4236, 2005.

[70] A. Schawlow. Laser light(laser light effects, applications and differentiation from incoherent light). *Scientific American*, 219(3):120–124, 1968.

[71] W.F. Schlotter. Lensless fourier transform holography with soft x-rays. *Dissertation*, 2007.

[72] W.F. Schlotter, J. Lüning, R. Rick, K. Chen, A. Scherz, S. Eisebitt, C.M. Günther, W. Eberhardt, O. Hellwig, and J. Stöhr. Extended field of view soft x-ray fourier transform holography: toward imaging ultrafast evolution in a single shot. *Optics Letters*, 32(21):3110–3112, 2007.

[73] W.F. Schlotter, R. Rick, K. Chen, A. Scherz, J. Stöhr, J. Lüning, S. Eisebitt, Ch. Günther, W. Eberhardt, O. Hellwig, and I. McNulty. Multiple reference fourier transform holography with soft x rays. *Applied Physics Letters*, 89(16):163112, 2006.

[74] G.W. Stroke. Lensless fourier-transform method for optical holography. *Applied Physics Letters*, 6(10):201–203, 1965.

[75] G.W. Stroke and D.G. Falconer. Attainment of high resolutions in wavefront-reconstruction imaging. *Physics Letters*, 13(4):306–309, 1964.

[76] K.B.K. Teo, M. Chhowalla, G.A.J. Amaratunga, W.I. Milne, D.G. Hasko, G. Pirio, P. Legagneux, F. Wyczisk, and D. Pribat. Uniform patterned growth of carbon nanotubes without surface carbon. *Applied Physics Letters*, 79(10):1534–1536, 2001.

[77] R. Accorsi und R.C. Lanza. Near-field artifact reduction in planar coded aperture imaging. *Applied Optics*, 40(26):4697–4705, 2001.

[78] D.T. Wilson, G.D. DeMeester, H.H. Barrett, and E. Barsack. A new configuration for coded aperture imaging. *Optics Communications*, 8(4):384–386, 1973.

[79] J.T. Winthrop and C.R. Worthington. X-ray microscopy by successive fourier transformation. *Physics Letters*, 15(2):124, 1965.

[80] J.W. Woods, M.P. Ekstrom, T.M. Palmieri, and R.E. Twogood. Best linear decoding of random mask images. *Ieee Transactions On Nuclear Science*, 22(1):379–383, 1975.

[81] C. Zhang, S. Pisana, C.T. Wirth, A. Parvez, C. Ducati, S. Hofmann, and J. Robertson. Growth of aligned millimeter-long carbon nanotube by chemical vapor deposition. *Diamond & Related Materials*, 17:1447–1451, 2008.

[82] http://www.andor.com/learning/digital_cameras/?docid=319.

[83] http://www.bessy.de/bit/bit_show_object.html.php?i_bit_id_object=34.

[84] http://www.bessy.de/bit/bit_show_object.html.php?i_bit_id_object=28.

[85] http://henke.lbl.gov/optical_constants/filter2.html.

[86] http://www.microscopyu.com/articles/optics/mtfintro.html.

[87] http://cvpr.uni-muenster.de/teaching/ws07/bildverarbeitungws07/script/bv07-2.pdf.

[88] Private communication with B. Pfau.

[89] Private communication with S. Boutet.

Appendix A

Acknowledgement

I would like to express my gratitude to all those who gave me support for completing my doctor thesis.

At first I want to thank my supervisor Stefan Eisebitt for giving me the chance to write my doctor thesis in his group. During my research time he gave me diverse opportunities to bring in my knowledge in different projects. I benefited a lot from the variety of experiments. Through Stefan Eisebitts engagement I experienced new possibilities of measurements at BESSY as well as at the Free Electron Laser FLASH. I especially want to thank Stefan Eisebitt for his patience, care and support in the final stage of my work.

In the first year of my stay at BESSY I had the pleasure to work together with Jan-Erik Rubensson. He gave me a lot of good advices and theoretical explanations with such a patience that I very enjoyed to talk to him. These many fruitful discussions helped me tremendously for my further research activities. I wished Jan-Erik Rubensson would have been stayed longer at BESSY. I really thank him for all of it.

A pleasure for me was also the team work in our group. Any questions were tried to be answered at any time. Special thanks to Bastian, Christian and Erik for their helpful contributions in many discussions. It was hard work but also just as much fun during plenty of beamtimes.

I would like to thank Ulrike Bloeck. During my time at the Focused Ion Beam

(FIB) she gave me much support in order to get familiar with the use of the FIB. Special thanks also to Nelia Wanderka who gave me the opportunity to work with the FIB.

In particular I want to thank Oliver Wilhelmi for providing me a number of samples that I could use for the measurements at BESSY. In several discussions he also helped me with sample preparations, even if they were not directly connected with my doctor thesis.

A special thank you I want to give to Emad Flear Aziz Bekhit for his encouraging and very motivating way with regard to the completion of my thesis.

Finally, I would like to say thank you to my family. Without their support I would not have finished my doctor thesis. Especially my girlfriend Nicole I want to give a very lovely thank. She encouraged me to go ahead with my work and supported me in every way she could. Special thanks also to my parents for their strong support and for being there for me. I appreciate very much the way they are standing behind me in the things I do.

Appendix B

Deutsche Zusammenfassung

Mannigfaltige und ausgedehnte Referenzen in der Fourier Transformations Holographie

Die Fourier Transformations Holographie (FTH) im Bereich der weichen Röntgenstrahlung hat sich vor allem durch die Einführung Freier Elektronenlaser (FEL) zu einem schnell wachsenden Forschungsgebiet entwickelt. In der klassischen FTH mit einem einzelnen Punktloch als Referenz sind Untersuchungen von Objekten auf kurzen Zeitskalen typischerweise mit einer schwachen Signalausbeute verbunden. Die hohe transversale Kohärenz der FELs eröffnet die Möglichkeit, Referenzstrukturen in der FTH zu erweitern, um eine höhere Signalausbeute bei gleicher Belichtungszeit zu erhalten.

Im Bereich der erweiterten Referenzen werden in dieser Arbeit zwei Strukturen vorgestellt, das mannigfaltige und das ausgedehnte Referenzmuster. Ersteres besteht ausschließlich aus Punktlöchern, letzteres hingegen kann jegliche Gestalt mit mindestens einer Ecke annehmen. Als Vertreter der mannigfaltigen Referenzmuster wird die URA und als Vertreter der ausgedehnten Referenzmuster wird das HERALDO-Muster diskutiert.

Die URA besteht aus vielen eng beieinander liegenden Punktlöchern, die zusammen eine kompakte Referenzstruktur bilden. Die Anordnung der Punktlöcher ist so gewählt, dass jeder Abstand zwischen ihnen gleich häufig vorkommt. Diese spezielle Anordnung führt dazu, dass das Objekt, welches bereits durch die FTH

mit der Referenz-URA gefaltet ist, durch eine zweite Faltung rekonstruiert werden kann. Diese Vorgehensweise wird als Faltungsmethode bezeichnet. Die für die zweite Faltung verwendete URA, die Rekonstruktions-URA, enthält als Grundlage die gleiche Basis-URA wie die Referenz-URA.
Der RSH-Wert, das Verhältnis zwischen Lochabstand und Lochgröße, ist der wichtigste Parameter zur Rekonstruktion des Objektes ohne Einsatz eines mathematischen iterativen Algorithmus. Ein bedeutendes Ergebnis dieser Arbeit ist, dass der RSH-Wert in der Rekonstruktions-URA unabhängig vom RSH-Wert in der Referenz-URA ist und als Voraussetzung für eine optimale Rekonstruktion des Objektes stets Null sein muss.
Unter Verwendung des FIBs vom Helmholtz-Zentrum Berlin wurde eine Probe mit einer selbsttragenden Referenz-URA hergestellt und gemessen. Ohne Zuhilfenahme eines mathematischen iterativen Algorithmus konnte das Objekt erfolgreich rekonstruiert werden. Mit Hilfe eines zusätzlichen Punktloches konnte die Auflösung in der Faltungsmethode mit den jeweiligen Auflösungen in der klassischen FTH und der Entfaltungsmethode verglichen werden. Die Messungen ergaben, dass die Faltungsmethode weder an die Auflösung der klassischen FTH noch an die Auflösung der Entfaltungsmethode heranreichte. Die Rekonstruktion nach der klassischen FTH erzielte die weitaus beste Auflösung von 130 nm.

Das in dieser Arbeit betrachtete HERALDO-Muster besteht aus einer einzelnen Linie als Referenz. Die Referenzpunkte werden mathematisch in Form einer Ableitung entlang dieser Linie erzeugt, nachdem das Hologram detektiert wurde. Die Auflösung bestimmt sich durch den Übergang zwischen höchster Transmission und höchster Absorption. Die Auflösung ist umso höher, je kürzer dieser Übergang ist. Darüber hinaus hängt der Kontrast von der Unterschiedshöhe in der Transmission zwischen höchster Transmission und höchster Absorption ab. Je größer der Unterschied, desto stärker ist der Kontrast.
Das HERALDO-Konzept wurde erstmalig im Bereich der weichen Röntgenstrahlen umgesetzt. In den Messungen konnte eine Auflösung von 48 nm erreicht werden. Mittels Drehung der Probe konnte sogar eine Verbesserung der Auflösung auf 28 nm erzielt werden. Die Möglichkeit der Drehung der Probe stellt eine Besonderheit des HERALDO-Musters dar. Hierdurch lässt sich eine 3D-Darstellung der räumlichen Absorption erzeugen.

Beide Referenzmuster besitzen ihre eigenen Vor- und Nachteile. Trotz vorhandener Nachteile sind beide Referenzmuster sehr interessant für zukünftige Experimente in der FTH im Bereich der weichen Röntgenstrahlung. Beide Referenzmuster erhöhen die Signalintensität bei konstanter Belichtungszeit. Insbesondere bei FEL-Experimenten mit einer Belichtungszeit von nur wenigen Femtosekunden erfreuen sich derartige Referenzmuster zunehmender Beliebtheit.